Miniaturized generator – collector electrochemical sensors

Zafarani, Hamid

DOI
10.4233/uuid:f56a09c9-e381-49c8-8313-14c347f33ce7

Publication date
2018

Document Version
Final published version

Citation (APA)
Zafarani, H. (2018). *Miniaturized generator – collector electrochemical sensors*. [Dissertation (TU Delft), Delft University of Technology]. https://doi.org/10.4233/uuid:f56a09c9-e381-49c8-8313-14c347f33ce7

MINIATURIZED GENERATOR - COLLECTOR ELECTROCHEMICAL SENSORS

MINIATURIZED GENERATOR - COLLECTOR ELECTROCHEMICAL SENSORS

Proefschrift

ter verkrijging van de graad van doctor
aan de Technische Universiteit Delft,
op gezag van de Rector Magnificus prof. dr. ir. T.H.J.J. van der Hagen,
voorzitter van het College voor Promoties,
in het openbaar te verdedigen op
woensdag 26 september 2018 om 12:30 uur

door

Hamid Reza ZAFARANI

Master of Science in Materials Science and Engineering,
Shiraz University, Iran,
geboren te Shiraz, Iran.

This dissertation has been approved by the

promotor: Prof. dr. E.J.R. Sudhölter

Composition of the doctoral committee:

Rector Magnificus,	Chairman
Prof. dr. E.J.R. Sudhölter	Delft University of Technology, promotor
Prof. dr. S.G. Lemay	University of Twente
Independent members:	
Prof. dr. ir. M.T. Kreutzer	Delft University of Technology
Prof. dr. A. Schmidt-Ott	Delft University of Technology
Dr. ir. M.A. van der Veen	Delft University of Technology
Prof. dr. J.G.E. Gardeniers	University of Twente

The work described in this thesis was carried out in the Organic Materials and Interfaces (OMI) section, Department of Chemical Engineering, Faculty of Applied Science, Delft University of Technology.
Dr. Liza Rassaei, as supervisor, has contributed significantly to the preparation of this dissertation.

Printed by: ....

ISBN 000-00-0000-000-0

An electronic version of this dissertation is available at
http://repository.tudelft.nl/.

To my parents,
Thanks for a lifetime love, loyalty and support,
You always have your own ways to make me feel great.

CONTENTS

1

INTRODUCTION

1

1.1. ELECTROCHEMICAL SENSORS

ELECTROCHEMICAL sensing is one of the most attractive detection techniques in different areas such as industrial [1, 2], clinical [3–6], environmental [7, 8] analyses; mainly owing to its fast response time, high selectively and sensitivity and ease of miniaturization for analytical systems [9–11]. These sensors work according to electrochemical measuring techniques, *e.g.*, cyclic voltammetry and amperometry [12]. These techniques are powerful measurement methods in redox-active species studies. In the cyclic voltammetry (CV) technique, the potential of the working electrode is continuously sweeping - respect to the solution's potential - with a defined scan rate according to a triangular wave, while the electrode current is recorded. The voltammogram depends on the electrode size as will be discussed more in the following sections. In the amperometry technique, the working electrode is biased to a constant potential and the resulting current is measured in time [13–15]. In these approaches the measuring faradaic currents are then proportional to the flux of molecules that react per unit time at the working electrode and accordingly to the analyte concentration [16, 17]. Hence, the mass transfer rate of the analytes toward the electrode surface limits the measured current and consequently the detection limit of the electrochemical sensor [17].

1.2. MASS TRANSFER

Mass transfer, *i.e.* the ion movements from one location to the other in a solution, can be caused by three individual modes or processes: diffusion, migration and convection. Diffusion is the ion movements as a result of the chemical potential gradient (*i.e.*, the concentration gradient) in a solution; charged ion movements as a result of the applied electric field is migration and convection is the ion movements as a result of the solution moving such as stirring or forced laminar/turbulent flow of the solution. The Nernst-Planck equation represents these three modes and is given in equation 1.1 for the one-dimensional mass transfer studies:

$$J_i(x) = \underbrace{-D_i \frac{\partial C_i(x)}{\partial x}}_{Diffusion} \underbrace{- \frac{z_i F}{RT} D_i C_i \frac{\partial \phi(x)}{\partial x}}_{Migration} + \underbrace{C_i v(x)}_{Convection} \tag{1.1}$$

Where $J_i(x)$ is the flux of species i (mol $s^{-1}cm^{-2}$) at distance x from the electrode surface, D_i is the diffusion coefficient (cm^2s^{-1}), $\frac{\partial C_i(x)}{\partial x}$ is the concentration gradient at distance x, $\frac{\partial \phi(x)}{\partial x}$ is the potential gradient, z_i and C_i are the charge (dimensionless) and concentration (mol cm^{-3}) of species i, respectively, and $v(x)$ is the velocity (cm s^{-1}) with which a volume element in solution moves along the axis (perpendicular to the electrode surface).

Throughout this thesis, the migrational and convectional components of the mass transfer are neglected (unless otherwise stated); by the addition of an inert electrolyte (supporting electrolyte) and conducting the measurements under stagnant condition. Hence, diffusion is considered as the only mass transport mode.

Applying Fast Scan Cyclic Voltammetry (FSCV) method - where as in the CV method the potential of the working electrode is linearly scanned, but now with much higher scan rates (in the kHz or even MHz range) [18, 19] - can overcome the mass transport

rate limitation as pointed above. In this method, as long as the sweep rate frequency of the electrode dominates the diffusion, the sensitivity (measured current) is not limited by the mass transfer rate toward the electrode surface. However, a large capacitive background current and electrode fouling (caused by irreversible adsorption of impurities or oxidation by products) are the two major drawbacks of FSCV method [20, 21]. Employing the microelectrodes is another approach to address the mass transport limitation in electrochemical measurement techniques, which will be described in the following section.

1.3. DIFFUSION MODES: FROM MACRO TO MICRO ELECTRODES

Depending on the size of the electrode, mainly two diffusion regimes exist: planar (macroelectrode) and radial (microelectrode). Bard [14] defined a microelectrode as an electrode having at least one dimension smaller than 25 μm. There is also a more general definition for a microelectrode; an electrode with the size smaller than the scale of the diffusion layer developed in the experiments (δ >r; δ is diffusion layer thickness and r is the radius of the electrode). Considering a spherical diffusion field rather than a planar, Fick's second law becomes [14],

$$\frac{\partial C_O(r,t)}{\partial t} = D_O \left\{ \frac{\partial^2 C_O(r,t)}{\partial r^2} + \frac{2}{r} \frac{\partial C_O(r,t)}{\partial r} \right\} \tag{1.2}$$

Where C_O and D_O are the surface concentration and diffusion coefficient of species O, respectively and r is the radial distance from the electrode center. The boundary conditions are then,

$$C_O(r,0) = C_O^* \qquad (r > r_0) \tag{1.3}$$

$$\lim_{r\to\infty} C_O(r,t) = C_O^* \tag{1.4}$$

$$C_O(r_0,t) = 0 \qquad (t > 0) \tag{1.5}$$

where r_0 is the radius of the electrode and C_O^* is the bulk concentration. Solving the equation to obtain the diffusion current, yields to,

$$i_d(t) = nFAD_O C_O^* \left[\frac{1}{(\pi D_O t)^{1/2}} + \frac{1}{r_0} \right] \tag{1.6}$$

Which can be rewritten as,

$$i_d(spherical) = i_d(linear) + \frac{nFAD_O C_O^*}{r_0} \tag{1.7}$$

It is seen in equation 1.7 that for the microelectrodes, the second term adds to the current which is expected for macroelectrodes. At a macroelectrode, diffusion to or from the electrode surface happens in a planar mode (figure 1.1A and C). In this case the diffusion at the edges of the macroelectrode - which is actively to the point and makes large mass transport rate at the edges - is negligible compare to the planar diffusion contribution over the entire electrode area. However, by reducing the size of the electrode to micro or even smaller the edge effect makes an impact on the diffusion mode - changes

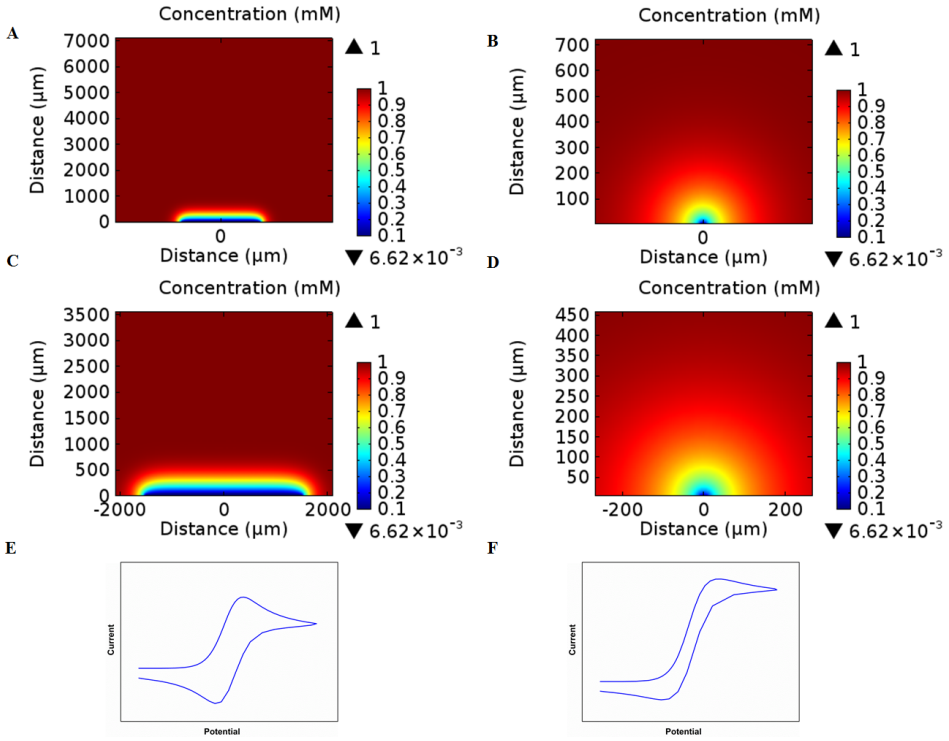

Figure 1.1: Planar (A, C and E) and spherical (B, D and F) diffusion modes in a macroelectrode and microelectrode and related CVs. (A) and (C) showing a planar diffusion mode with the concentration profile near a macroelectrode surface (3 mm in diameter) in a 1 mM reduced form solution of an assumed redox active system. (B) and (D) showing a radial (spherical) diffusion mode with the concentration profile near a microelectrode surface (10 μm in diameter) in a 1 mM reduced form solution of an assumed redox active system. (E) and (F) representing the CVs for a macroelectrode (3 mm in diameter) and a microelectrode (10 μm in diameter) respectively.

from planar mode to radial (spherical) - which consequently affects the mass transport (figure 1.1B and D). Hence the current density is higher in microelectrods compare to macroelectrodes. Other advantages of using microelectrodes are a lower background current (due to the smaller electrode area), fast response time and the ability to be applicable in small sample volumes [22]. Changing the electrode size to micro, and accordingly changing the diffusion mode, can also influences the shape of the voltammogram [23]. As shown in figure 1.1, the peak shape behavior voltammogram for macroelectrode (1.1E) is changed to a sigmoidal behavior for the microeletrode (1.1F).

Placing two microelectrodes (or an array of microelectrodes) close to each other in a way that their diffusion fields overlap, introduces new powerful analytical devices known as dual-electrode sensors [24]. These kind of sensors will be discussed in more detail in the following sections.

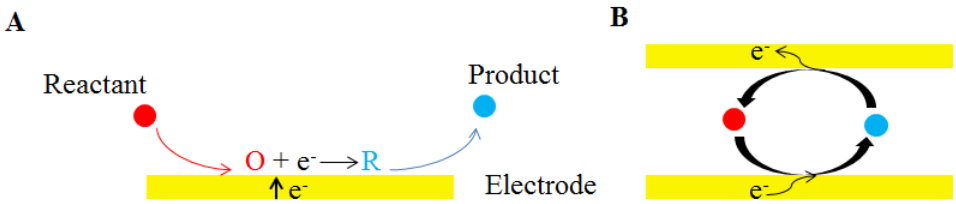

Figure 1.2: (A) Illustration of a redox reaction on an electrode surface and (B) the redox cycling mechanism between two closely spaced electrodes.

1.4. DUAL- ELECTRODE SENSORS AND REDOX CYCLING

A conventional electrochemical measurement setup consists of a working electrode, a reference electrode and a counter electrode. By biasing the working electrode into an appropriate potential versus the reference electrode the redox active species available in the electrochemical cell will be reduced/oxidized at the working electrode surface. In this setup each species contributes only once in the redox reaction and gain/lose one or a couple of electrons on the electrode surface (depends on the species valency) and there is a need for diffusion of the new redox active species from the bulk to the electrode surface (figure 1.2A); Hence the current is limited by the mass transport rate toward the working electrode surface as discussed above. Also the electrical detection limit of the instruments (*i.e.* considering diluted solution of the redox active species) confines the sensitivity of this setup [25, 26]. The current can be greatly enhanced by placing a second electrode (dual-electrode sensor) in a close proximity to the first [27], in a way that their diffusion fields overlap. Hence the events at each electrode can be affected by the other one; The oxidized/reduced species from an electrode reach to the adjacent electrode where the species can reduced/oxidized back to the initial state. The repeated, successive oxidation and reduction of analyte molecules at these two electrodes provide the required charge amplification (figure 1.2B). This process is called redox cycling which allows each redox active species to oxidize and reduce several times and so enhances the detection sensitivity [26].

For the first time Reilly and coworkers [28, 29] introduced the redox cycling approach and Fan and Bard extended this toward single molecules detection [30]. Reilly used a cylindrical section of the solution bounded by two parallel plane electrode faces. A precision micrometer controlled the distance between the electrodes [29, 31]. A Teflon collar, was pressed onto the micrometer spindle hold the sample solution between the electrodes and the Teflon collar (figure 1.3). Fan and Bard [30] created a nanogap by approaching a Pt-Ir tip to a conductive substrate within nanometer scale using a scanning electrochemical microscope (SECM). Small tip electrode of nanometer dimension surrounded by insulating sheath, provides confinement of the molecules between the tip and the conductive surface, as illustrated in figure 1.4.

In recent years, by improving the nanofabrication techniques, there is considerable interest in developing robust dual-electrode sensors with a nanometer scale gap between the electrodes. The nanogap devices provide the selective and sensitive detec-

1

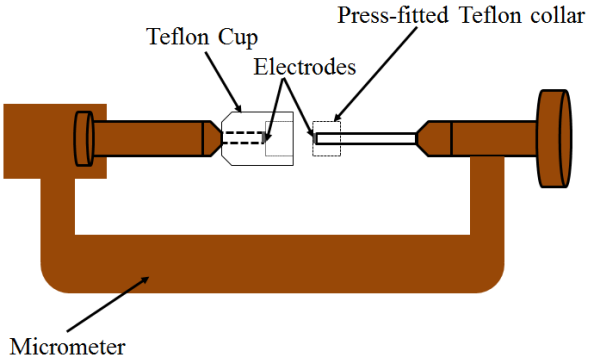

Figure 1.3: Schematic illustration of two parallel plane electrodes at close distance controlled by a precise micrometer as proposed by Reilly [29, 31].

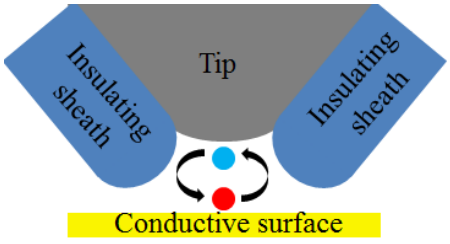

Figure 1.4: Schematic illustration of a scanning electrochemical microscope working in redox cycling mode as proposed by Fan and Bard [30].

tion tools for analytical and bioanalytical applications [32, 33]. These devices lead to fundamental studies and experiments such as investigations on Brownian motion at the nanoscale and single molecule detection [34–36].

1.5. PRINCIPLE OF REDOX CYCLING

Dual-electrode systems provide powerful tools in electroanalytical studies [24, 37]. A generator-collector electrode system consists of two independent working electrodes; In these systems usually one electrode is sweeping in a defined potential range to oxidize/reduce the desired species and the other one is kept at a fixed potential to reduce/oxidize the produced species to another species (usually to the initial one) [24], thus the redox active species sequentially shuttle multiple times between the two electrodes [27] and hence the obtained current is amplified. The potential or the current at each electrode is controlled separately and the resulting steady-state flux of electroactive species is inversely proportional to the distance separating the two electrodes [30]. Previously Anderson and Reilley presented an equation for estimating the limiting current for two planar electrodes separated by a thin layer of fluid [28],

$$I = \frac{nFADC}{z} \tag{1.8}$$

where I is the limiting Faradaic current for two planar electrodes in close distance of z, n is the number of transferred electrons per redox active species, A is the overlapping area of the two electrodes, D the diffusing constant and C is the bulk concentration of species.

By applying appropriate potentials on the generator and the collector electrodes, only one redox couple can selectively be cycled between the electrodes, which gives an opportunity to selectively detect it in a mixture with other redox active species. This aspect make these devices as a useful tool for selective detection for target analyte based on difference in redox reversibility [38–41]. Redox cycling can provide a strong tool in the biosensing area, where there is a need for a fast, sensitive, selective analytical method [42–44]; Such as contamination sensing [45]; determining physical molecular properties such as diffusion coefficient [33, 46] and single molecule detection [47, 48].

There are different approaches and methods toward the fabrication of redox cycling devices [24, 39, 49–51]. Interdigitated electrodes (IDE) are one class of redox cycling electrodes [52, 53]. IDEs consist of two sets of comb-shaped electrodes where the teeth of each set are aligned between the teeth of the another (figure 1.5) [24].

Recessed ring-disk electrode arrays, where each pore contains a disk electrode at the bottom and a ring electrode on the top which are separated by an insulation layer, forms another type of redox cycling devices. Here the top electrode faces the electrolyte directly and the bottom electrode is achievable via the pore opening in the top electrode and the insulating layer [39, 54].

Another type of redox cycling devices are thin layer cells which consist of two planar electrodes separated by a thin layer of liquid [32]. In recent years Marken *et al.* described a simple method for fabrication of dual-plate systems assembled by placing a thin epoxy layer between two electrodes (figure 1.6) [55]. Within this simple and low cost fabrication method they performed many fundamental studies, such as nitrite detection [9], ion transfer at liquid-liquid interfaces [56]. As equation 1.8 indicates, reducing the gap

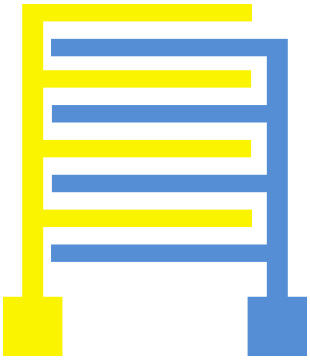

Figure 1.5: Schematic illustration of Interdigitated electrodes (IDE).

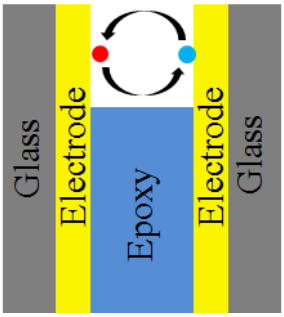

Figure 1.6: Schematic illustration of dual-electrode junction assembly proposed by Marken *et al.* [55].

between the electrodes enhances the efficiency of these devices. Owing to the advances in nanofabrication techniques, reducing the electrodes gap to the nanometer scale is achievable. Pioneering work on nanogap electrodes produced via lithography has been reported by Lemay and coworkers [57]. In nanogap electrochemistry experiments the volume of liquid between the two electrodes plays the role of a small volume, which can go down to femtoliters of the desired species [44], depends on the gap geometry. Most of developed designs for nanogap redox cycling devices are based on several steps of successive photo/e-beam lithography and evaporation and sputtering different metal/oxide layers [32, 42, 58].

The proposed nanogap device by Lemay (1.7) consists of a sandwich structure of three evaporated metal layers; a bottom electrode, a sacrificial chromium layer and finally the top electrode. For each layer separate patterning procedure is needed which is done by photo or e-beam lithography. Next the whole structure is covered by an insulation layer (such as SiO_2) and followed by the dry etching process. The access holes are created through the insulation layer to the chromium layer. Finally, by etching away the chromium layer the nanogap is created. Hence, the thickness of the chromium layer defines the electrodes gap. A detailed fabrication method is presented by Zevenbergen *et al.* [58]. This geometry with some modifications has been used by many researchers for

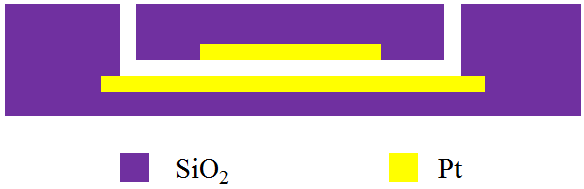

Figure 1.7: Schematic illustration of nanogap device assembly proposed by Lemay *et al.* [58].

different purposes [44, 59, 60]. These kind of nanogap sensors considered as powerful analytical devices used for a variety of applications such as biosensing and contamination sensing [26, 44]

The advantages of the redox cycling devices are not only limited to an improvement of the sensor sensitivity by amplification of faradic currents, but also in the current study we use the nanogap sensors for new applications. We use the nanogap sensors for determination of molecular properties such as diffusion coefficient as a function of specific oxidation states of redox couples. Furthermore we show that these sensors are able to simultaneously detect several redox active species separately and overcome interference in electrochemical response. The method relies on modulating the potentials of both electrodes in a way that each species is separately detected.

The fabrication of the above mentioned nanogap devices requires several steps of consecutive e-beam or photolithography, depositions, and dry etching, making the overall process rather complex [61]. Hence, in the first place considering the need for more sensitive sensing devices, there is a demand for new nanogap sensors which are simpler to fabricate. Second, the sensitivity of any thin layer cell sensor is increased by reducing the gap size between the two electrodes. However, considering the technical fabrication limitations making the nanogap smaller than couple of tenth nm is challenging in the above mentioned nanogap devices. Finally making the nanogap device with the other electrode materials beyond platinum or gold is not achievable. In this thesis we aim to develop more straightforward method with less complicated fabrication procedures, possible variation of electrode materials, further reduction of the inter-electrode distance, increasing its sensitivity and reducing the active volume in nanogap sensors. Moreover, the new proposed nanogap geometry in this thesis allows direct access of optical detection methods either from the top or through a transparent substrate using an inverted microscope, thus enabling direct observation of combined optical-electrochemical molecular properties. Improving the sensor response time is another achievement of the new introduced sensor here compared to the previous sensors.

1.6. THESIS OUTLINE

The objective of this thesis is to investigate the unique advantages of applying dual-electrode (nanogap) sensors and also study and introduce new designs and fabrication procedures of such a systems for analytical applications. The upcoming chapters of the thesis are arranged as follows:

Chapter 2: Interference or crosstalk of coexisting redox species, *i.e.* other species

than the desired one can participate in the redox reactions and reduces the selectivity of the detection technique. We have addressed this limitation by using nanogap devices. New strategies for selective sensing of three different redox species in a nanogap sensor are reported. The approach relies on the modulation of the electrode potentials to define a specific potential windows between the two working electrodes. Consequently, specific detection of each redox species is achieved.

Chapter 3: In this chapter a nanogap sensor is employed to investigate the physical properties of multi ferrocenylic compounds, 2,3,4- triferrocenylthiophene and 2,5-diferrocenylthiophene, such as diffusion coefficient as a function of the oxidation states of a specific redox couple as well as the faradaic current generated per molecule in an nonpolar media. The Stochastic Amperometry method was employed in these studies.

Chapter 4: Numerical simulation are applied to design and optimize the geometry of new electrochemical sensors before following the sophisticated, expensive fabrication procedures (trial and error). Simulating the applied conditions (such as applied potential) in a desired sensor can also reveal more insight into the underlying physical phenomena (such as diffusion and concentration profile around the electrodes and through the nanochannel as a function of potential *etc.*). In this chapter a new design for nanogap sensors working based on the redox cycling is introduced. The proposed device consists of two closely spaced side-by-side electrodes which work under redox cycling conditions. By using finite element simulations, the effects of different geometric parameters on the redox cycling signal amplification are investigated. Results allows optimizing the sensor performance of the devices for fabrication.

Chapter 5: In this chapter the proposed new nanogap sensor (chapter 4) is fabricated. The new nanogap sensor consists of two side-by-side gold electrodes placed at a 70 nm distance and encompassing a 20 attoliter nanogap volume. Experimental voltammetry results are compared to the simulated results from finite element analysis.

Chapter 6: In this chapter a novel, simple and low cost method for the fabrication of microjunction electrodes is presented. The device consists of platinum leaves, with micron-sized pores, separated by a porous track etch membrane spacer. It is shown that the device can be employed in generator-collector mode.

REFERENCES

[1] M. Badea, A. Amine, G. Palleschi, D. Moscone, G. Volpe, and A. Curulli, *New electrochemical sensors for detection of nitrites and nitrates,* Journal of Electroanalytical Chemistry **509**, 66 (2001).

[2] J. Bunney, S. Williamson, D. Atkin, M. Jeanneret, D. Cozzolino, and J. Chapman, *The use of electrochemical biosensors in food analysis,* Current Research in Nutrition and Food Science Journal **5**, 183 (2017).

[3] A. Vasudev, A. Kaushik, Y. Tomizawa, N. Norena, and S. Bhansali, *An ltcc-based microfluidic system for label-free, electrochemical detection of cortisol,* Sensors and Actuators B: Chemical **182**, 139 (2013).

[4] Q. Yan, B. Peng, G. Su, B. E. Cohan, T. C. Major, and M. E. Meyerhoff, *Measurement of tear glucose levels with amperometric glucose biosensor/capillary tube configuration,* Analytical chemistry **83**, 8341 (2011).

[5] M. Gamella, S. Campuzano, J. Manso, G. G. De Rivera, F. López-Colino, A. Reviejo, and J. Pingarrón, *A novel non-invasive electrochemical biosensing device for in situ determination of the alcohol content in blood by monitoring ethanol in sweat,* Analytica chimica acta **806**, 1 (2014).

[6] A. J. Bandodkar and J. Wang, *Non-invasive wearable electrochemical sensors: a review,* Trends in biotechnology **32**, 363 (2014).

[7] K. A. Howell, E. P. Achterberg, C. B. Braungardt, A. D. Tappin, D. R. Turner, and P. J. Worsfold, *The determination of trace metals in estuarine and coastal waters using a voltammetric in situ profiling system,* Analyst **128**, 734 (2003).

[8] M.-L. Tercier and J. Buffle, *In situ voltammetric measurements in natural waters: future prospects and challenges,* Electroanalysis **5**, 187 (1993).

[9] A. J. Gross, S. Holmes, S. E. Dale, M. J. Smallwood, S. J. Green, C. P. Winlove, N. Benjamin, P. G. Winyard, and F. Marken, *Nitrite/nitrate detection in serum based on dual-plate generator–collector currents in a microtrench,* Talanta **131**, 228 (2015).

[10] M. A. Hasnat, A. J. Gross, S. E. Dale, E. O. Barnes, R. G. Compton, and F. Marken, *A dual-plate ito–ito generator–collector microtrench sensor: surface activation, spatial separation and suppression of irreversible oxygen and ascorbate interference,* Analyst **139**, 569 (2014).

[11] J. Wang, *Electrochemical detection for microscale analytical systems: a review,* Talanta **56**, 223 (2002).

[12] U. Guth, W. Vonau, and J. Zosel, *Recent developments in electrochemical sensor application and technology—a review,* Measurement Science and Technology **20**, 042002 (2009).

[13] R. S. Nicholson and I. Shain, *Theory of stationary electrode polarography. single scan and cyclic methods applied to reversible, irreversible, and kinetic systems.* Analytical Chemistry **36**, 706 (1964).

[14] A. J. Bard, L. R. Faulkner, *et al.*, *Fundamentals and applications,* Electrochemical Methods **2** (2001).

[15] R. G. Compton and C. E. Banks, *Understanding voltammetry* (World Scientific, 2011).

[16] M. A. Zevenbergen, P. S. Singh, E. D. Goluch, B. L. Wolfrum, and S. G. Lemay, *Electrochemical correlation spectroscopy in nanofluidic cavities,* Analytical chemistry **81**, 8203 (2009).

[17] E. Kätelhön and B. Wolfrum, *On-chip redox cycling techniques for electrochemical detection,* Reviews in Analytical Chemistry **31**, 7 (2012).

[18] J. O. Howell and R. M. Wightman, *Ultrafast voltammetry and voltammetry in highly resistive solutions with microvoltammetric electrodes,* Analytical Chemistry **56**, 524 (1984).

[19] C. Amatore, E. Maisonhaute, and G. Simonneau, *Ultrafast cyclic voltammetry: performing in the few megavolts per second range without ohmic drop,* Electrochemistry communications **2**, 81 (2000).

[20] D. L. Robinson, B. J. Venton, M. L. Heien, and R. M. Wightman, *Detecting subsecond dopamine release with fast-scan cyclic voltammetry in vivo,* Clinical chemistry **49**, 1763 (2003).

[21] R. B. Keithley, P. Takmakov, E. S. Bucher, A. M. Belle, C. A. Owesson-White, J. Park, and R. M. Wightman, *Higher sensitivity dopamine measurements with faster-scan cyclic voltammetry,* Analytical chemistry **83**, 3563 (2011).

[22] Q. Wu, C.-C. Liu, *et al.*, *Development of chemical sensors using microfabrication and micromachining techniques,* Sensors and Actuators B: Chemical **13**, 1 (1993).

[23] D. A. Brownson, C. E. Banks, *et al.*, *The handbook of graphene electrochemistry* (Springer, 2014).

[24] E. O. Barnes, G. E. Lewis, S. E. Dale, F. Marken, and R. G. Compton, *Generator-collector double electrode systems: A review,* Analyst **137**, 1068 (2012).

[25] S. G. Lemay, S. Kang, K. Mathwig, and P. S. Singh, *Single-molecule electrochemistry: present status and outlook,* Accounts of chemical research **46**, 369 (2012).

[26] E. D. Goluch, B. Wolfrum, P. S. Singh, M. A. Zevenbergen, and S. G. Lemay, *Redox cycling in nanofluidic channels using interdigitated electrodes,* Analytical and bioanalytical chemistry **394**, 447 (2009).

[27] M. A. Zevenbergen, D. Krapf, M. R. Zuiddam, and S. G. Lemay, *Mesoscopic concentration fluctuations in a fluidic nanocavity detected by redox cycling,* Nano letters **7**, 384 (2007).

[28] L. B. Anderson and C. N. Reilley, *Thin-layer electrochemistry: steady-state methods of studying rate processes,* Journal of Electroanalytical Chemistry (1959) **10**, 295 (1965).

[29] L. B. Anderson and C. N. Reilley, *Thin-layer electrochemistry: use of twin working electrodes for the study of chemical kinetics,* Journal of Electroanalytical Chemistry (1959) **10**, 538 (1965).

[30] F.-R. F. Fan and A. J. Bard, *Electrochemical detection of single molecules,* Science **267**, 871 (1995).

[31] D. M. Oglesby, S. H. Omang, and C. N. Reilley, *Thin layer electrochemical studies using controlled potential or controlled current.* Analytical Chemistry **37**, 1312 (1965).

[32] L. Rassaei, P. S. Singh, and S. G. Lemay, *Lithography-based nanoelectrochemistry,* (2011).

[33] P. S. Singh, H.-S. M. Chan, S. Kang, and S. G. Lemay, *Stochastic amperometric fluctuations as a probe for dynamic adsorption in nanofluidic electrochemical systems,* Journal of the American Chemical Society **133**, 18289 (2011).

[34] K. Krause, K. Mathwig, B. Wolfrum, and S. Lemay, *Brownian motion in electrochemical nanodevices,* The European Physical Journal Special Topics **223**, 3165 (2014).

[35] S. Kang, A. F. Nieuwenhuis, K. Mathwig, D. Mampallil, and S. G. Lemay, *Electrochemical single-molecule detection in aqueous solution using self-aligned nanogap transducers,* ACS nano **7**, 10931 (2013).

[36] S. Kang, K. Mathwig, and S. G. Lemay, *Response time of nanofluidic electrochemical sensors,* Lab on a Chip **12**, 1262 (2012).

[37] S. E. Dale, C. E. Hotchen, and F. Marken, *Generator–collector electroanalysis at tin-doped indium oxide–epoxy–tin-doped indium oxide junction electrodes,* Electrochimica Acta **101**, 196 (2013).

[38] V. Dam, W. Olthuis, and A. Van den Berg, *Redox cycling with facing interdigitated array electrodes as a method for selective detection of redox species,* Analyst **132**, 365 (2007).

[39] C. Ma, N. M. Contento, L. R. Gibson, and P. W. Bohn, *Redox cycling in nanoscale-recessed ring-disk electrode arrays for enhanced electrochemical sensitivity,* Acs Nano **7**, 5483 (2013).

[40] O. Niwa, M. Morita, and H. Tabei, *Highly sensitive and selective voltammetric detection of dopamine with vertically separated interdigitated array electrodes,* Electroanalysis **3**, 163 (1991).

[41] W. R. Vandaveer, D. J. Woodward, and I. Fritsch, *Redox cycling measurements of a model compound and dopamine in ultrasmall volumes with a self-contained microcavity device,* Electrochimica acta **48**, 3341 (2003).

[42] B. Wolfrum, M. Zevenbergen, and S. Lemay, *Nanofluidic redox cycling amplification for the selective detection of catechol,* Analytical chemistry **80**, 972 (2008).

[43] F. Zhu, J. Yan, M. Lu, Y. Zhou, Y. Yang, and B. Mao, *A strategy for selective detection based on interferent depleting and redox cycling using the plane-recessed microdisk array electrodes,* Electrochimica Acta **56**, 8101 (2011).

[44] L. Rassaei, K. Mathwig, S. Kang, H. A. Heering, and S. G. Lemay, *Integrated biodetection in a nanofluidic device,* ACS nano **8**, 8278 (2014).

[45] M. Li, G. E. Lewis, T. D. James, Y.-T. Long, B. Kasprzyk-Hordern, J. M. Mitchels, and F. Marken, *Oil| water interfacial phosphate transfer facilitated by boronic acid: Observation of unusually fast oil| water lateral charge transport,* ChemElectroChem **1**, 1640 (2014).

[46] K. Mathwig, H. R. Zafarani, J. M. Speck, S. Sarkar, H. Lang, S. G. Lemay, L. Rassaei, and O. G. Schmidt, *Potential-dependent stochastic amperometry of multiferrocenylthiophenes in an electrochemical nanogap transducer,* The Journal of Physical Chemistry C **120**, 23262 (2016).

[47] S. Kang, A. F. Nieuwenhuis, K. Mathwig, D. Mampallil, Z. A. Kostiuchenko, and S. G. Lemay, *Single-molecule electrochemistry in nanochannels: probing the time of first passage,* Faraday discussions **193**, 41 (2016).

[48] K. Mathwig, T. J. Aartsma, G. W. Canters, and S. G. Lemay, *Nanoscale methods for single-molecule electrochemistry,* Annual Review of Analytical Chemistry **7**, 383 (2014).

[49] M. Odijk, W. Olthuis, V. e. e. Dam, and A. van den Berg, *Simulation of redox-cycling phenomena at interdigitated array (ida) electrodes: Amplification and selectivity,* Electroanalysis **20**, 463 (2008).

[50] O. Niwa, M. Morita, and H. Tabei, *Electrochemical behavior of reversible redox species at interdigitated array electrodes with different geometries: consideration of redox cycling and collection efficiency,* Analytical Chemistry **62**, 447 (1990).

[51] M. Straver, M. Odijk, W. Olthuis, and A. van den Berg, *A simple method to fabricate electrochemical sensor systems with predictable high-redox cycling amplification,* Lab on a Chip **12**, 1548 (2012).

[52] P. Van Gerwen, W. Laureyn, W. Laureys, G. Huyberechts, M. O. De Beeck, K. Baert, J. Suls, W. Sansen, P. Jacobs, L. Hermans, *et al.*, *Nanoscaled interdigitated electrode arrays for biochemical sensors,* Sensors and Actuators B: Chemical **49**, 73 (1998).

[53] D. G. Sanderson and L. B. Anderson, *Filar electrodes: steady-state currents and spectroelectrochemistry at twin interdigitated electrodes,* Analytical chemistry **57**, 2388 (1985).

[54] M. Hüske, R. Stockmann, A. Offenhäusser, and B. Wolfrum, *Redox cycling in nanoporous electrochemical devices,* Nanoscale **6**, 589 (2014).

[55] S. E. Dale and F. Marken, *Pulse electroanalysis at gold–gold micro-trench electrodes: Chemical signal filtering,* Faraday discussions **164**, 349 (2013).

[56] S. E. Dale, Y. Chan, P. C. Bulman Page, E. O. Barnes, R. G. Compton, and F. Marken, *A gold–gold oil microtrench electrode for liquid–liquid anion transfer voltammetry,* Electrophoresis **34**, 1979 (2013).

[57] E. Kätelhön, B. Hofmann, S. G. Lemay, M. A. Zevenbergen, A. Offenhäusser, and B. Wolfrum, *Nanocavity redox cycling sensors for the detection of dopamine fluctuations in microfluidic gradients,* Analytical chemistry **82**, 8502 (2010).

[58] M. A. Zevenbergen, B. L. Wolfrum, E. D. Goluch, P. S. Singh, and S. G. Lemay, *Fast electron-transfer kinetics probed in nanofluidic channels,* Journal of the American Chemical Society **131**, 11471 (2009).

[59] L. Rassaei, K. Mathwig, E. D. Goluch, and S. G. Lemay, *Hydrodynamic voltammetry with nanogap electrodes,* The Journal of Physical Chemistry C **116**, 10913 (2012).

[60] S. Sarkar, K. Mathwig, S. Kang, A. F. Nieuwenhuis, and S. G. Lemay, *Redox cycling without reference electrodes,* Analyst **139**, 6052 (2014).

[61] H. R. Zafarani, K. Mathwig, E. J. Sudholter, and L. Rassaei, *Electrochemical amplification in side-by-side attoliter nanogap transducers,* ACS Sensors **2**, 724 (2017).

2

MODULATING SELECTIVITY IN NANOGAP SENSORS

Interference or crosstalk of coexisting redox species results in overlapping of electrochemical signals, and it is a major hurdle in sensor development. In nanogap sensors, redox cycling between two independently biased working electrodes results in an amplified electrochemical signal and an enhanced sensitivity. Here, we report new strategies for selective sensing of three different redox species in a nanogap sensor of a 2 fL volume. Our approach relies on modulating the electrode potentials to define specific potential windows between the two working electrodes; consequently, specific detection of each redox species is achieved. Finite element modeling is employed to simulate the electrochemical processes in the nanogap sensor, and the results are in good agreement with those of experiments.

This chapter is based on the following publication:

H.R. Zafarani, K. Mathwig, S.G. Lemay, E.J.R. Sudhölter and L. Rassaei, ACS SENSORS **2016**, *1*,1439-1444 [1].

2.1. INTRODUCTION

SELECTIVE detection of redox species is important in various fields such as pharmacy [2–4], pathology [5, 6], health [7–9] and environmental monitoring [10, 11]. Interference or crosstalk of coexisting compounds leads to the overlap of electrochemical responses and is one major drawback of these techniques; frequently encountered, it impedes simultaneous detection of species and limits the selectivity of electrochemical sensors [12, 13]. Thus, many research efforts have been devoted to overcome this hurdle, for example, by electrochemically pretreating of electrodes [14]; using different electrode materials [15]; modifying electrodes with organic compounds [16, 17], polymers [18, 19], or nanoparticles [11, 20, 21]; adding complexing agents to the solution [22]; or by using a combination of these methods [23, 24].

Sensing redox species using dual electrodes benefits from amplified electrochemical signals and enhanced sensitivity while the contribution from the background current is minimized [25, 26]. In such systems, one electrode is biased at the reduction potential and the other at the oxidation potential. Here, the redox-active species undergo successive oxidation and reduction reactions as they travel by diffusion between these closely spaced electrodes. Hence, the Faradaic current is amplified and the sensitivity is enhanced. Interdigitated electrodes (IDE) – as one of the well-known classes of dual electrode systems – have been widely used in different studies [27–29]. IDEs consist of a pair of comb-shaped opposing electrodes with interlocking teeth in which each set of electrodes can be independently biased.

A newer type of dual electrode systems is the electrochemical nanofluidic devices which consist of two planar parallel electrodes closely spaced (<100 nm) from each other in a nanofluidic channel [30–32]. The interferences in these nanogap devices [30, 33, 34] have mainly been eliminated by biasing one electrode at the potential that consumes the interference while the other electrode is swept to quantify the target analyte [35, 36]. The nanogap is depleted from interfering irreversible redox species and the signal for the analyte is insensitive to the interfering species. However, this method only eliminates the response from interfering irreversible redox species. Therefore, a more versatile technique is required to overcome the interferences from reversible redox species in these nanogap sensors.

In the present chapter, we introduce a new method to selectively detect three reversible redox species in the nanogap sensors. The method relies on modulating the potentials of both electrodes in a way that each species is separately detected. We implement this method for the simultaneous detection of these three species in three different ways unique to dualelectrode sensors: (a) by cyclic voltammetry and varying the fixed potential of the second working electrode; (b) by differential cyclic voltammetry (DCV) [37, 38]; and (c) by potential step chronoamperometry. Finite element analysis (COMSOL Multiphysics) is employed to model the electrochemical processes in the nanogap sensor and compare with those of experiments.

2.2. EXPERIMENTAL SECTION

Chemicals: 1,1'-ferrocene dimethanol, $Fc(MeOH)_2$, hexaammineruthenium(III) chloride, $Ru(NH_3)_6Cl_3$, and potassium iodide, KI, as electroactive model compounds; potas-

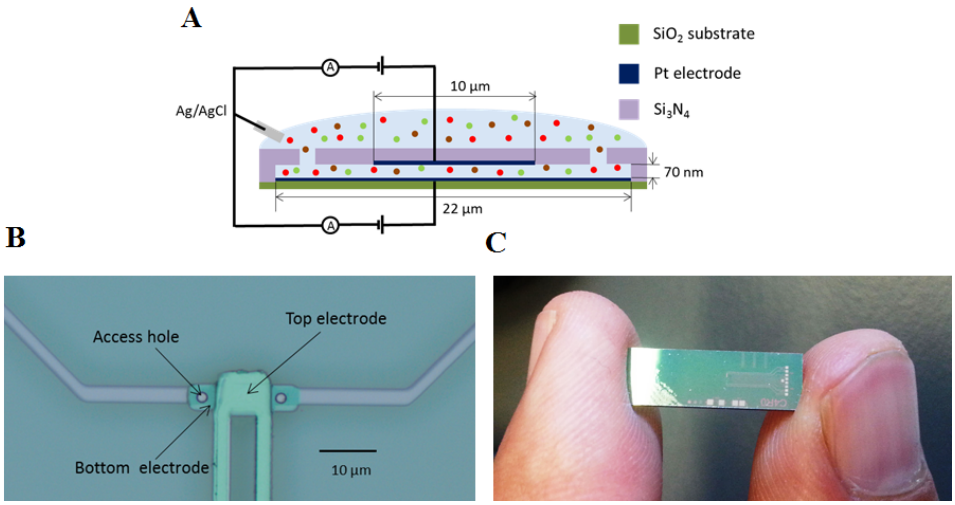

Figure 2.1: (A) Schematic view of the nanogap device. (B) Optical micrograph of a nanogap sensor (top view). (C) Image of nanogap sensor.

sium chloride, KCl, and standard chromium etchant were purchased from Sigma- Aldrich. All solutions were freshly prepared in Milli-Q water with 1 M KCl as supporting electrolyte and the experiments were carried out at room temperature.

Nanogap Device Fabrication: Nanogap devices were fabricated on a silicon wafer covered with 500 nm thermally grown SiO_2, employing several lithography steps and evaporation as previously reported [31]. In brief, a nanogap device consisted of a platinum bottom electrode of a 22 μm by 3 μm surface area and a top electrode of 10 μm by 9 μm. A 70-nm-thick sacrificial chromium layer between these two electrodes defined the volume of the nanochannel. The whole device was covered in a 500 nm silicon oxide/silicon nitride passivation layer in which access holes to the chromium layer were dry etched. Before measurements, the chromium layer was etched away using chromium etchant leaving behind a nanogap sensor. A schematic and optical micrograph of a nanogap device are presented in figure 2.1.

Electrochemical Measurements: Electrochemical experiments were carried out using a Keithley 4200 parameter analyzer with two source measurement units (SMUs). The SMUs were used as voltage source and current detection elements to separately bias both electrodes and measure faradic currents. A commercial Ag/AgCl electrode (BASi Inc.) was used as a reference, positioned in a reservoir on top of the nanogap device (Figure 2.2).

Numerical Methods: Two-dimensional finite element analysis was carried out using COMSOL Multiphysics to simulate the electrochemical processes in the nanochannel with conditions similar to those for the experimental measurements [39]. Assuming a highly concentrated supporting electrolyte and an unstirred solution, diffusion was considered as the only mass transport mechanism in the nanogap sensor as described by Fick's second law:

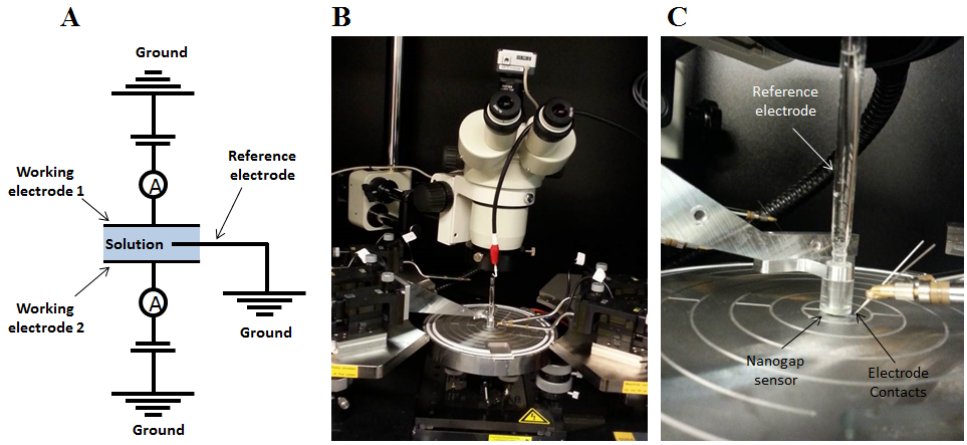

Figure 2.2: (A) Schematic view of the electrochemical measurements setup. (B) and (C) Image of electrochemical measurements setup.

$$\frac{\partial C_j}{\partial t} = D_j \nabla^2 C_j \tag{2.1}$$

Here, C_j and D_j are the concentration and diffusion coefficient of a redox species j, respectively. The currents are defined based on Butler-Volmer kinetics [40]:

$$i = F[c_O k_f - c_R k_b] \tag{2.2}$$

$$k_f = k_0 e^{[\frac{-\alpha F(E-E_h)}{RT}]} \tag{2.3}$$

$$k_b = k_0 e^{[\frac{(1-\alpha)F(E-E_h)}{RT}]} \tag{2.4}$$

Here, i is the current, k_0 is the mass transfer coefficient, α the charge transfer coefficient, F the Faraday constant, E the electrode potential, E_h the redox potential of the redox couple, k_f and k_b are the forward (reduction) and backward (oxidation) rate constants of a redox reaction, R is the gas constant, T the temperature, c_O and c_R are the concentration of oxidized and reduced species, respectively.

Table 2.1 lists constants used in the simulations, including diffusion coefficients D and redox potentials (*vs.* Ag/AgCl), E_h, for the $Fc(MeOH)_2$, KI and $Ru(NH_3)_6Cl_3$ redox couples. An identical rate constant k_o and transfer coefficients α were assumed for all species.

2.3. RESULTS AND DISCUSSION

Amplification Factor: Figure 2.3 shows the cyclic voltammograms obtained from the redox cycling of 0.33 mM 1,1'-ferrocene dimethanol in 1 M potassium chloride in the nanogap sensor. The inset in this figure presents the cyclic voltammogram obtained in

Table 2.1: Parameters used in the simulation processes [31, 38, 41–43]

$D_{Fc(MeOH)_2}$	$6.7 \times 10^{-10} m^2/s$	α	0.49
D_{I^-}	$2.05 \times 10^{-9} m^2/s$	F	96485.34 C/mol
$D_{Ru(NH_3)_6{}^{3+}}$	$7.5 \times 10^{-10} m^2/s$	R	8.31 J/K
$E_{h,Fc(MeOH)_2}$	0.26 V *vs.* Ag/AgCl	T	298 K
E_{h,I^-}	0.54 V *vs.* Ag/AgCl	k_o	0.06 m/s
$E_{h,Ru(NH_3)_6{}^{3+}}$	-0.16 V *vs.* Ag/AgCl		

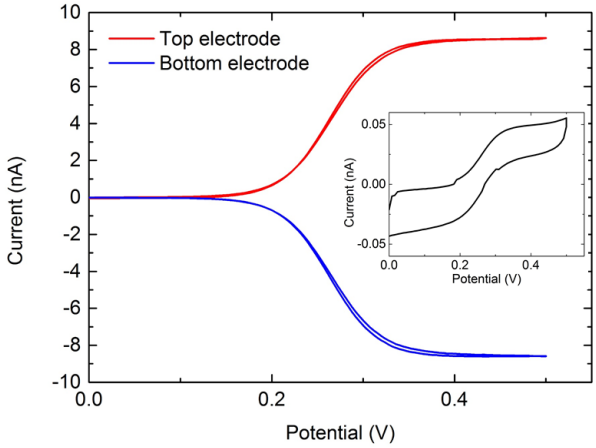

Figure 2.3: Cyclic voltammogram of 0.33 mM $Fc(MeOH)_2$ in 1 M KCl solution. The top electrode was swept between 0 and 0.5 V (*vs.* Ag/AgCl) at a 10 mVs^{-1} scan rate while the bottom electrode was kept at 0 V. The inset figure shows a cyclic voltammogram in single mode; the top electrode was swept *vs.* Ag/AgCl while the bottom electrode was kept floating.

single mode: only the top electrode was swept and the bottom electrode was left floating. Identical measurements were carried out for $Ru(NH_3)_6Cl_3$ and KI (see figure S1 in the Supporting Information). Comparing the limiting currents in these two modes, I_{dual}/I_{single}, leads to an amplification factor of 170 corresponding to a gap height of 74 nm according to equation 2.5 [34]:

$$I = \frac{nFADC}{z} \tag{2.5}$$

where I is limiting Faradaic current for two planar electrodes in close distance, n is the number of electrons transferred in the redox reaction, A is the overlapping area between the two electrodes, and z is the distance between the electrodes, i.e., the nanochannel height.

Tuning Electrodes' Potentials for Separate Detection of Each Species: Conventional electrochemical measurements suffer from poor selectivity, because, in a mixture of var-

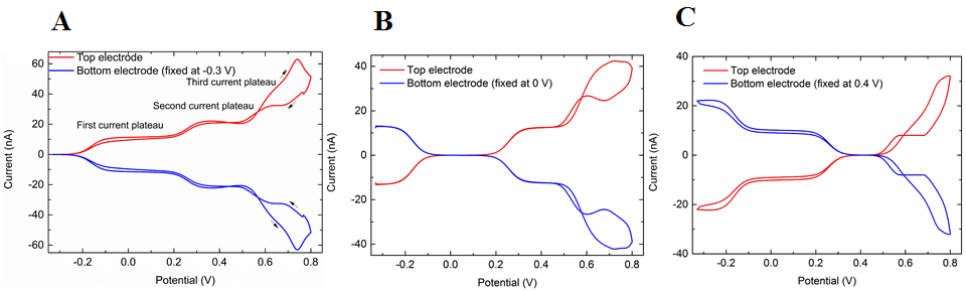

Figure 2.4: Cyclic voltammetry of a mixture of 0.33 mM $Ru(NH_3)_6^{3+}$, 0.33 mM $Fc(MeOH)_2$ and 0.33 mM I^- in a 1 M KCl solution. The top electrode is swept between -0.33 and 0.8 V at a scan rate of 10 mVs^{-1} and the bottom electrode potential is fixed at (A) -0.3 V, (B) 0 V, and (C) 0.4 V. Arrows (A) indicate the scan direction.

ious reduced (or oxidized) electroactive species having different standard redox potentials, all species are simultaneously oxidized (or reduced) when a high (or low) enough electrode potential is applied. The interferences caused this way complicate the interpretation of the results as the electrooxidation (or electro-reduction) current for the redox species with the highest oxidation (or lowest reduction) potential is superimposed by the signals from the other redox species.

Nanogap sensors not only allow amplifying the electrochemical signals of redox species, but also open up the possibility to prevent such interferences. The two working electrodes in the nanogap sensor are independently biased and, thus, they enable selective electrochemical reactions of specific redox couples. Selective detection is achieved by defining the potentials of the two electrodes in a way in which only the target species undergoes redox cycling. Simultaneously, interfering species are also reduced or oxidized but they do not undergo redox cycling, and therefore, the signal of these species is not amplified.

Figure 2.4 shows cyclic voltammograms for a mixture of 0.33 mM $Ru(NH_3)_6^{3+}$, 0.33 mM $Fc(MeOH)_2$ and 0.33 mM I^- in a 1 M KCl solution. Varying the bottom electrode potential to certain fixed potentials leads to a separate detection of these species in specific potential ranges. Here, the top electrode is swept between -0.33 and 0.8 V (*vs.* Ag/AgCl) while the potential of the bottom electrode is kept at -0.3, 0, and 0.4 V, respectively.

In figure 2.4A, the potential of the bottom electrode is set at -0.3 V. As presented, the potential of the top electrode is scanned from -0.3 V, and the first current plateau corresponds to redox cycling of $Ru(NH_3)_6^{3+/2+}$ ions (E_h = -0.16 V) without any interference from the other two species; the second current plateau relates to the combined redox cycling of $Fc(MeOH)_2^{0/+1}$ (E_h = 0.26 V) and $Ru(NH_3)_6^{3+/2+}$ ions. The third current plateau associates with the redox cycling of I^- (E_h = 0.54 V) and the previous two species. The redox reactions of the species are as follows:

$$Fc(MeOH)_2 \rightleftarrows Fc(MeOH)_2^+ + e^- \tag{2.6}$$

$$Ru(NH_3)_6^{3+} + e^- \rightleftarrows Ru(NH_3)_6^{2+} \tag{2.7}$$

$$I^- \rightleftarrows 1/2 I_2 + e^- \tag{2.8}$$

Once the potential of the bottom electrode is changed to 0 V (see figure 2.4 B), the interference and the contribution of $Ru(NH_3)_6^{3+/2+}$ ions on redox cycling of $Fc(MeOH)_2^{0/+1}$ and I^- disappears. As presented in this figure, here, redox cycling of $Ru(NH_3)_6^{3+/2+}$ occurs in the potential window of -0.3 to -0.16 V. For potentials above -0.16 V, $Ru(NH_3)_6^{3+/2+}$ ions exist in the oxidized form and cannot undergo redox cycling anymore. Hence, their contribution to the redox cycling currents of $Fc(MeOH)_2^{0/+1}$ and I^- is eliminated. This allows detection of the signal of $Fc(MeOH)_2^{0/+1}$ (second current plateau) without any $Ru(NH_3)_6^{3+/2+}$ interference in this potential range. Notwithstanding, the third current plateau still suffers from the interference of $Fc(MeOH)_2^{0/+1}$, and the redox cycling current of I^- is superimposed by $Fc(MeOH)_2^{0/+1}$. In order to resolve this issue, the potential of the bottom electrode is next set at 0.4 V (Figure 2.4C). Here, for potentials above 0.26 V, only I^- can undergo redox cycling (third current plateau) and the signal is free from any interferences of both $Fc(MeOH)_2^{0/+1}$ and $Ru(NH_3)_6^{3+/2+}$. Note that at potentials above 0.26 V in figure 2.4C, $Fc(MeOH)_2^{0/+1}$ is constantly oxidized at both electrodes, but it does not undergo redox cycling; this leads to a negligible current contribution (resulting to a deviation of 0.16%) compared to the amplified redox cycling current.

Using equation 2.5 and the constants in Table 2.1, the expected limiting currents are estimated to be 11 nA, 9 nA, and 30 nA for $Ru(NH_3)_6^{3+/2+}$, $Fc(MeOH)_2^{0/+1}$ and I^-, respectively, in good agreement with those obtained from experimental measurements (see figure 2.4). The 30 nA oxidation current obtained for I^- (also presented in figure 2.4C) indicates that this process is overall a one-electron transfer reaction in agreement with previous reports [44–46]. The hysteresis observed during the oxidation of iodide is caused by a pronounced desorption of iodide ions from the electrode surface during the forward scan and subsequent adsorption after the potential reversal [47].

Differential Cyclic Voltammetry of Redox Species in the Nanogap Sensor: We employ the method of differential cyclic voltammetry [38] to directly visualize the separate sensing of all species in a single potential sweep. Here, the potentials of both electrodes are simultaneously swept with a constant offset. We define various potential windows of 10 mV, 25 mV, 50 mV, and 100 mV between the two working electrodes in the same mixture solution of 0.33 mM $Fc(MeOH)_2$, 0.33 mM $Ru(NH_3)_6$ and 0.33 mM I^- in 1 M aqueous KCl. Once these potential windows are defined, a clear peak current is obtained for each redox species. The peak potential for each species corresponds to its redox potential.

Figure 2.5 shows the redox cycling currents obtained as a function of the mean potential between the top and bottom electrodes and a clear separation of all species. Due to the simultaneous sweep of both electrodes, the resulting currents have a differential nature. The peak currents at the half-wave potential of each species correspond to $\Delta I/\Delta E$ as well as to the species' concentration. As shown in figure 2.5, a narrower potential window leads to a lower current but a better separation of species. For example, for a potential window of 10 mV, a peak current of 1.12 nA is obtained for $Fc(MeOH)_2^{0/+1}$ species, while for a 100 mV potential window, the current peaks at 7.8 nA. However, the full width at half-maximum (fwhm) increases from 92 mV for a 10 mV potential window to 125 mV for a 100 mV potential window. Therefore, a wider potential window limits how well the redox species are separated; the baseline distance between $Fc(MeOH)_2^{0/+1}$ peak and adjacent peaks is decreased by applying a wider potential window. The widest potential window that can be applied depends on the difference in the redox potentials of species.

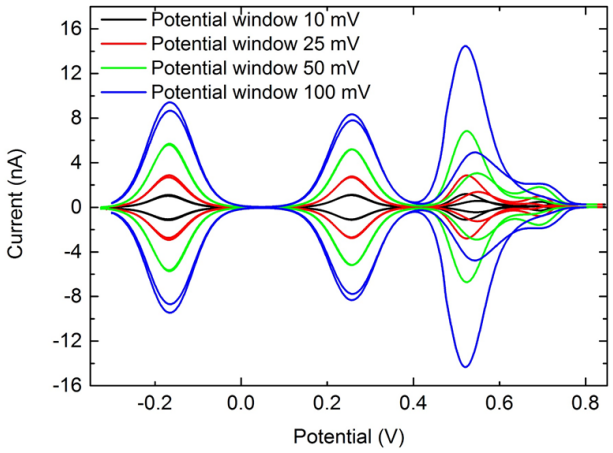

Figure 2.5: Differential cycling voltammetry in the nanogap sensor. The top and bottom electrodes are swept (*vs.* Ag/AgCl) at a scan rate of 10 mVs^{-1} with a constant potential difference ranging from 10 mV to 100 mV. The limiting currents are shown as a function of mean potential between the two electrodes.

For example, the largest potential window for separate detection of $Fc(MeOH)_2^{0/+1}$ and I^- is 280 mV corresponding to $E_{h,I^-} - E_{h,Fc(MeOH)_2} = 280$ mV (more details are presented in figure S2 in the Supporting Information).

Chronoamperometric Detection of Redox Species in the Nanogap Sensor: In the voltammetry schemes described above, the discriminatory power of specific electrode biases for both electrodes is shown in a direct way. However, the separate detection of analytes plays out its full advantage in chronoamperometric sensing with fixed potentials, in which redox waves of potential interfering species are not visible. We employed chronoamperometry in the nanogap sensor. Here, the device is filled with a mixture of 0.4 mM KI and 0.6 mM $Fc(MeOH)_2$ in 1 M KCl solution. A constant potential of 0.4 V *vs.* Ag/AgCl is applied to the top electrode while the potential of the bottom electrode is stepped between 0.1 and 0.4 V and then between 0.4 and 0.7 V (see figure 2.6).

Once the potential of the bottom electrode is stepped to 0.1 V, $Fc(MeOH)_2$ undergoes redox cycling (first two steps) without any interference from I^-. Here, $Fc(MeOH)_2$ is constantly oxidized at the top electrode and reduced at the bottom electrode. Similarly, when the bottom electrode potential is stepped to 0.7 V, I^- ions undergo redox cycling without any interference from $Fc(MeOH)_2^{0/+1}$. I^- is constantly oxidized at the bottom electrode and reduced at the top electrode. At the same time, $Fc(MeOH)_2^{0/+1}$ is constantly oxidized at both top and bottom electrodes, but since they cannot undergo redox cycling, their contribution to the current for I^- is negligible (resulting in a deviation of 0.3%). These results are in good agreement with those obtained from cyclic voltammetry. The long transient time for I^- is due to the dynamic adsorption at the Pt electrode surfaces [47–49].

Numerical Analysis: Figure 2.7 shows the comparison of cyclic voltammetry as well as differential cyclic voltammetry of 0.33 mM $Ru(NH_3)_6^{3+}$, 0.33 mM $Fc(MeOH)_2$ and 0.33 mM I^- in 1 M KCl for experimental measurements and finite element simulation results.

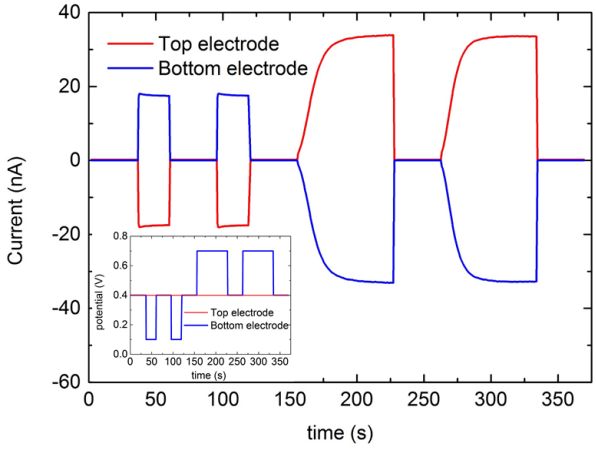

Figure 2.6: Chronoamperometry results obtained for a mixture of 0.6 mM $Fc(MeOH)_2$ and 0.4 mM KI in 1 M KCl solution. The inset shows the applied potentials as a function of time. The top electrode is kept at constant potential of 0.4 V and the bottom electrode is stepped to 0.1, 0.4, or 0.7 V.

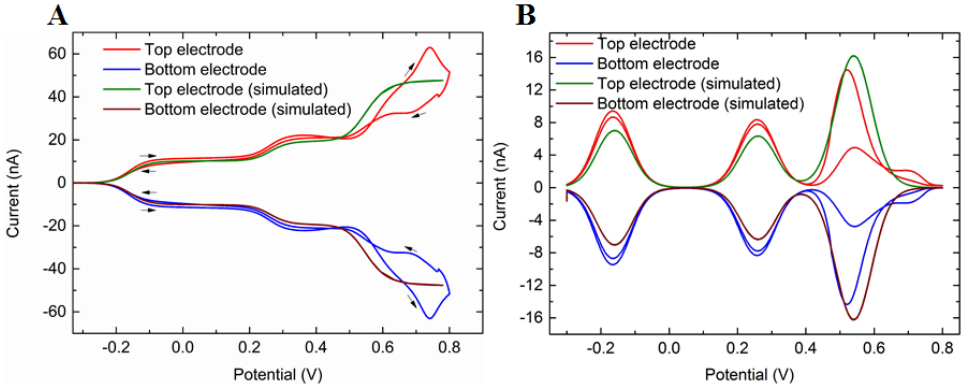

Figure 2.7: (A) Comparison of cyclic voltammograms (at a scan rate of 10 mVs^{-1}) of a mixture of 0.33 mM $Ru(NH_3)_6^{3+}$, 0.33 mM $Fc(MeOH)_2$ and 0.33 mM I^- in 1 M KCl (see also figure 2.4A) with those numerical results. Arrows indicate the scan direction. (B) Comparison of experimental and simulated differential cyclic voltammetry (at a scan rate of 10 mVs^{-1}) of a potential window of 100 mV (see also figure 2.5).

Figure 2.7A presents the simulated data and its comparison with experimental cyclic voltammograms; here, the top electrode potential is swept between -0.33 and 0.8 V (*vs.* Ag/AgCl) and the bottom electrode potential is kept at -0.3 V. Figure 2.7B presents differential cyclic voltammograms for the potential window of 100 mV for both experimental and modeled results. As depicted, simulated data match well with experimental data. However, a hysteresis is observed experimentally for the oxidation and reduction of I^- due to pronounced adsorption of I^- [47], which has not been considered in the simulations.

2.4. CONCLUSION

We proposed a novel strategy for the separate detection of redox active species in nanogap sensors and implemented it in three ways: first, by tuning the electrode potentials only desired species undergo redox cycling; hence, the obtained current is free of any interferences (shown for both cyclic voltammetry and chronoamperometric measurements). Second, by defining a potential window between the two electrodes and simultaneously sweeping them, each species can individually undergo redox cycling. Third, by chronoamperometry specific concentrations can be monitored without interference by using a matching potential window. A good agreement was obtained between the experimental and simulation results. The techniques introduced in this study may lead to new ways for the selective detection of redox species in nanogap devices.

REFERENCES

[1] H. R. Zafarani, K. Mathwig, S. G. Lemay, E. J. Sudholter, and L. Rassaei, *Modulating selectivity in nanogap sensors,* ACS Sensors **1**, 1439 (2016).

[2] S. Akbar, A. Anwar, and Q. Kanwal, *Electrochemical determination of folic acid: A short review,* Analytical biochemistry **510**, 98 (2016).

[3] A. Rahi, K. Karimian, and H. Heli, *Nanostructured materials in electroanalysis of pharmaceuticals,* Analytical biochemistry **497**, 39 (2016).

[4] E. Er, H. Çelikkan, and N. Erk, *Highly sensitive and selective electrochemical sensor based on high-quality graphene/nafion nanocomposite for voltammetric determination of nebivolol,* Sensors and Actuators B: Chemical **224**, 170 (2016).

[5] B. V. Chikkaveeraiah, A. A. Bhirde, N. Y. Morgan, H. S. Eden, and X. Chen, *Electrochemical immunosensors for detection of cancer protein biomarkers,* ACS nano **6**, 6546 (2012).

[6] H. Li, J. He, S. Li, and A. P. Turner, *Electrochemical immunosensor with n-doped graphene-modified electrode for label-free detection of the breast cancer biomarker ca 15-3,* Biosensors and Bioelectronics **43**, 25 (2013).

[7] L. Rassaei, W. Olthuis, S. Tsujimura, E. J. Sudhölter, and A. van den Berg, *Lactate biosensors: current status and outlook,* Analytical and bioanalytical chemistry **406**, 123 (2014).

[8] M. Fojta, A. Daňhel, L. Havran, and V. Vyskočil, *Recent progress in electrochemical sensors and assays for dna damage and repair,* TrAC Trends in Analytical Chemistry **79**, 160 (2016).

[9] E. Paleček, J. Tkáč, M. Bartošík, T. Bertók, V. Ostatná, and J. Paleček, *Electrochemistry of nonconjugated proteins and glycoproteins. toward sensors for biomedicine and glycomics,* Chemical reviews **115**, 2045 (2015).

[10] B. Kumar Jena and C. Retna Raj, *Gold nanoelectrode ensembles for the simultaneous electrochemical detection of ultratrace arsenic, mercury, and copper,* Analytical chemistry **80**, 4836 (2008).

[11] L. Rassaei, F. Marken, M. Sillanpää, M. Amiri, C. M. Cirtiu, and M. Sillanpää, *Nanoparticles in electrochemical sensors for environmental monitoring,* TrAC Trends in Analytical Chemistry **30**, 1704 (2011).

[12] G. Dutta, S. Park, A. Singh, J. Seo, S. Kim, and H. Yang, *Low-interference washing-free electrochemical immunosensor using glycerol-3-phosphate dehydrogenase as an enzyme label,* Analytical chemistry **87**, 3574 (2015).

[13] X. Liu, M. Zhang, T. Xiao, J. Hao, R. Li, and L. Mao, *Protein pretreatment of microelectrodes enables in vivo electrochemical measurements with easy precalibration and interference-free from proteins,* Analytical chemistry **88**, 7238 (2016).

[14] S. Alwarappan, G. Liu, and C.-Z. Li, *Simultaneous detection of dopamine, ascorbic acid, and uric acid at electrochemically pretreated carbon nanotube biosensors,* Nanomedicine: Nanotechnology, Biology and Medicine **6**, 52 (2010).

[15] J. Wu, J. Suls, and W. Sansen, *Amperometric determination of ascorbic acid on screen-printing ruthenium dioxide electrode,* Electrochemistry communications **2**, 90 (2000).

[16] M. D. Raicopol, C. Andronescu, R. Atasiei, A. Hanganu, E. Vasile, A. M. Brezoiu, and L. Pilan, *Organic layers via aryl diazonium electrochemistry: towards modifying platinum electrodes for interference free glucose biosensors,* Electrochimica Acta **206**, 226 (2016).

[17] C. R. Raj and T. Ohsaka, *Voltammetric detection of uric acid in the presence of ascorbic acid at a gold electrode modified with a self-assembled monolayer of heteroaromatic thiol,* Journal of Electroanalytical Chemistry **540**, 69 (2003).

[18] Y. Li, L. Zhang, J. Liu, S.-F. Zhou, K. A. Al-Ghanim, S. Mahboob, B.-C. Ye, and X. Zhang, *A novel sensitive and selective electrochemical sensor based on molecularly imprinted polymer on a nanoporous gold leaf modified electrode for warfarin sodium determination,* RSC Advances **6**, 43724 (2016).

[19] Y. Li, H. Song, L. Zhang, P. Zuo, B.-c. Ye, J. Yao, and W. Chen, *Supportless electrochemical sensor based on molecularly imprinted polymer modified nanoporous microrod for determination of dopamine at trace level,* Biosensors and Bioelectronics **78**, 308 (2016).

[20] C.-L. Sun, H.-H. Lee, J.-M. Yang, and C.-C. Wu, *The simultaneous electrochemical detection of ascorbic acid, dopamine, and uric acid using graphene/size-selected pt nanocomposites,* Biosensors and Bioelectronics **26**, 3450 (2011).

[21] S. Thiagarajan and S.-M. Chen, *Preparation and characterization of ptau hybrid film modified electrodes and their use in simultaneous determination of dopamine, ascorbic acid and uric acid,* Talanta **74**, 212 (2007).

[22] A. Idris, J. Mafa, N. Mabuba, and O. Arotiba, *Dealing with interference challenge in the electrochemical detection of as (iii)—a complexometric masking approach,* Electrochemistry Communications **64**, 18 (2016).

[23] T. Yin, W. Wei, and J. Zeng, *Selective detection of dopamine in the presence of ascorbic acid by use of glassy-carbon electrodes modified with both polyaniline film and multi-walled carbon nanotubes with incorporated β-cyclodextrin,* Analytical and bioanalytical chemistry **386**, 2087 (2006).

[24] O. Sadak, A. K. Sundramoorthy, and S. Gunasekaran, *Highly selective colorimetric and electrochemical sensing of iron (iii) using nile red functionalized graphene film,* Biosensors and Bioelectronics **89**, 430 (2017).

[25] Y. Kanno, K. Ino, H. Shiku, and T. Matsue, *A local redox cycling-based electrochemical chip device with nanocavities for multi-electrochemical evaluation of embryoid bodies,* Lab on a Chip **15**, 4404 (2015).

[26] E. O. Barnes, G. E. Lewis, S. E. Dale, F. Marken, and R. G. Compton, *Generator-collector double electrode systems: A review,* Analyst **137**, 1068 (2012).

[27] O. Niwa, M. Morita, and H. Tabei, *Electrochemical behavior of reversible redox species at interdigitated array electrodes with different geometries: consideration of redox cycling and collection efficiency,* Analytical Chemistry **62**, 447 (1990).

[28] K. Hayashi, J.-i. Takahashi, T. Horiuchi, Y. Iwasaki, and T. Haga, *Development of nanoscale interdigitated array electrode as electrochemical sensor platform for highly sensitive detection of biomolecules,* Journal of The Electrochemical Society **155**, J240 (2008).

[29] A. K. Samarao, M. J. Rust, and C. H. Ahn, *Rapid fabrication of a nano interdigitated array electrode and its amperometric characterization as an electrochemical sensor,* in *Sensors, 2007 IEEE* (IEEE, 2007) pp. 644–647.

[30] B. Wolfrum, M. Zevenbergen, and S. Lemay, *Nanofluidic redox cycling amplification for the selective detection of catechol,* Analytical chemistry **80**, 972 (2008).

[31] M. A. Zevenbergen, B. L. Wolfrum, E. D. Goluch, P. S. Singh, and S. G. Lemay, *Fast electron-transfer kinetics probed in nanofluidic channels,* Journal of the American Chemical Society **131**, 11471 (2009).

[32] L. Rassaei, K. Mathwig, S. Kang, H. A. Heering, and S. G. Lemay, *Integrated biodetection in a nanofluidic device,* ACS nano **8**, 8278 (2014).

[33] M. A. Hasnat, A. J. Gross, S. E. Dale, E. O. Barnes, R. G. Compton, and F. Marken, *A dual-plate ito–ito generator–collector microtrench sensor: surface activation, spatial separation and suppression of irreversible oxygen and ascorbate interference,* Analyst **139**, 569 (2014).

[34] E. D. Goluch, B. Wolfrum, P. S. Singh, M. A. Zevenbergen, and S. G. Lemay, *Redox cycling in nanofluidic channels using interdigitated electrodes,* Analytical and bioanalytical chemistry **394**, 447 (2009).

[35] R. S. Martin, A. J. Gawron, S. M. Lunte, and C. S. Henry, *Dual-electrode electrochemical detection for poly (dimethylsiloxane)-fabricated capillary electrophoresis microchips,* Analytical chemistry **72**, 3196 (2000).

[36] E. Kätelhön, B. Hofmann, S. G. Lemay, M. A. Zevenbergen, A. Offenhäusser, and B. Wolfrum, *Nanocavity redox cycling sensors for the detection of dopamine fluctuations in microfluidic gradients,* Analytical chemistry **82**, 8502 (2010).

[37] M. Van Megen, M. Odijk, J. Wiedemair, W. Olthuis, and A. Van den Berg, *Differential cyclic voltammetry for selective and amplified detection,* Journal of Electroanalytical Chemistry **681**, 6 (2012).

[38] M. Odijk, J. Wiedemair, M. van Megen, W. Olthuis, and A. van den Berg, *Differential cyclic voltammetry-a novel technique for selective and simultaneous detection using redox cyling based sensors,* in *Sensors, 2010 IEEE* (IEEE, 2010) pp. 918–922.

[39] H. R. Zafarani, K. Mathwig, E. J. Sudhölter, and L. Rassaei, *Electrochemical redox cycling in a new nanogap sensor: Design and simulation,* Journal of Electroanalytical Chemistry **760**, 42 (2016).

[40] A. J. Bard, L. R. Faulkner, *et al.*, *Fundamentals and applications,* Electrochemical Methods **2** (2001).

[41] I. Kolthoff and J. Jordan, *Voltammetry of iodine and iodide at rotated platinum wire electrodes,* Journal of the American Chemical Society **75**, 1571 (1953).

[42] L. Rassaei, K. Mathwig, E. D. Goluch, and S. G. Lemay, *Hydrodynamic voltammetry with nanogap electrodes,* The Journal of Physical Chemistry C **116**, 10913 (2012).

[43] C. Ma, N. M. Contento, L. R. Gibson, and P. W. Bohn, *Redox cycling in nanoscale-recessed ring-disk electrode arrays for enhanced electrochemical sensitivity,* Acs Nano **7**, 5483 (2013).

[44] R. W. French and F. Marken, *Growth and characterisation of diffusion junctions between paired gold electrodes: diffusion effects in generator–collector mode,* Journal of Solid State Electrochemistry **13**, 609 (2009).

[45] F. Marken, R. P. Akkermans, and R. G. Compton, *Voltammetry in the presence of ultrasound: the limit of acoustic streaming induced diffusion layer thinning and the effect of solvent viscosity,* Journal of Electroanalytical Chemistry **415**, 55 (1996).

[46] P. Tomčík and D. Bustin, *Voltammetric determination of iodide by use of an interdigitated microelectrode array,* Fresenius' journal of analytical chemistry **371**, 562 (2001).

[47] D. Mampallil, K. Mathwig, S. Kang, and S. G. Lemay, *Reversible adsorption of outer-sphere redox molecules at pt electrodes,* The journal of physical chemistry letters **5**, 636 (2014).

[48] S. Kang, K. Mathwig, and S. G. Lemay, *Response time of nanofluidic electrochemical sensors,* Lab on a Chip **12**, 1262 (2012).

[49] K. Mathwig and S. G. Lemay, *Mass transport in electrochemical nanogap sensors,* Electrochimica Acta **112**, 943 (2013).

2.5. SUPPORTING INFORMATION

Herein, we present individual cyclic voltammograms of selected electroactive model compounds (I^- and and $Ru(NH_3)_6^{3+}$) in the nanogap sensor (Figure S1). Figure S2 shows the simulated differential cyclic voltammograms in the nanogap with different potential windows. Here, we investigated the effect of the potential window on peak separation of redox species in differential cyclic voltammetry.

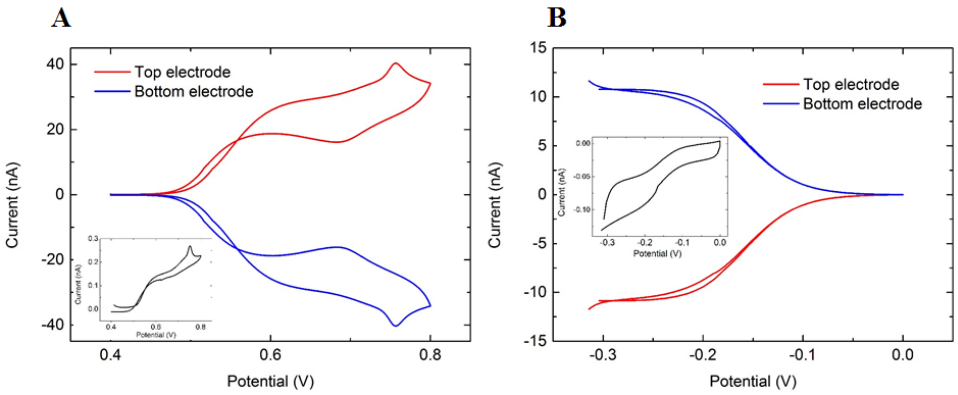

Figure S1: Cyclic voltammetry of individual species. (A) CV of 0.33 mM I^- in 1 M KCl solution. The top electrode was swept from 0.4 to 0.8 V (*vs.* Ag/AgCl) at a 10 mVs^{-1} scan rate while the bottom electrode was fixed at 0 V, (B) CV of 0.33 mM $Ru(NH_3)_6^{3+}$ in 1 M KCl solution. Top electrode was swept from -0.33 to 0 V at a 10 mVs^{-1} scan rate while the bottom electrode was fixed at 0 V. The insets shows CVs in single mode. Here, only the top electrode was swept and the bottom electrode was kept floating.

As shown in figure S1A, the characteristic peak current signal of I^- is presented in both cyclic voltammograms recorded in dual mode and in single mode.

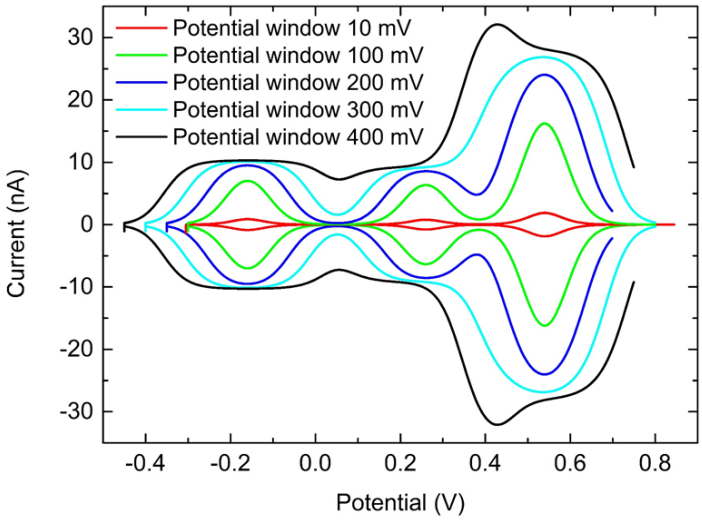

Figure S2. Modelled differential cycling voltammetry in the nanogap sensor. The top and bottom electrodes are swept with a constant potential difference ranging from 10 mV to 400 mV. The limiting currents are shown as a function of the mean potential between the two electrodes.

Figure S2 presents the simulated differential cyclic voltammograms in the nanogap sensor with different potential windows. Increasing the potential window between the two electrodes from 200 mV to 300 mV leads to the overlapping of the peak currents for $Fc(MeOH)_2$ and I^-; hence, selectivity is lost.

3

POTENTIAL-DEPENDENT STOCHASTIC AMPEROMETRY OF MULTI FERROCENYL THIOPHENES IN AN ELECTROCHEMICAL NANOGAP TRANSDUCER

In nanofluidic electrochemical sensors based on redox cycling, zeptomole (10^{-21}) quantities of analyte molecules can be detected as redox-active molecules travel diffusively between two electrodes separated by a nanoscale gap. These sensors are employed to study the properties of multi ferrocenylic compounds in nonpolar media, 2,3,4- triferrocenyl thiophene and 2,5-diferrocenyl thiophene, which display well-resolved electrochemically reversible one-electron transfer processes. Using stochastic analysis, we are able to determine, as a function of the oxidation states of a specific redox couple, the effective diffusion coefficient as well as the Faradaic current generated per molecule, all in a straightforward experiment requiring only a mesoscopic amount of molecules in a femtoliter compartment. It was found that diffusive transport is reduced for higher oxidation states and that analytes yield very high currents per molecule of 15 fA.

This chapter is based on the following publication:

K. Mathwig, H.R. Zafarani, J.M. Speck, S. Sarkar, H. Lang, S.G. Lemay,L. Rassaei and O.G. Schmidt, The Journal of Physical Chemistry C, **2016**, *120*, 23262-23267 [1].

3.1. INTRODUCTION

THERE is great interest in miniaturized electrochemical sensors for their ease of integration in lab-chip applications, highly sensitive detection, the requirement of only the smallest sample volumes, direct electrical signal transduction, and cost effectiveness when standard microfabrication is employed [2–9]. We previously reported on electrochemical nanogap sensors which allow sensitive analysis in femtoliter detection volumes [10]. In these systems, electrochemically active analyte molecules shuttle by diffusion between two electrodes embedded in the roof and ceiling of a nanochannel (figure 3.1). Thereby, the molecules undergo redox cycling, *i.e.*, they are repeatedly oxidized and reduced at the opposing electrodes at kilohertz frequencies. In this way, each analyte contributes a current of several thousand electrons per second, resulting in a high intrinsic signal amplification (as compared to a single-electrode configuration in which a molecule reacts only once).

Nanogap sensors are currently rare in their ability to perform stochastic amperometric sensing [11]. Only a small number of molecules are present in a very limited detection volume, even at high analyte concentrations. Therefore, the system can be described as a mesoscopic regime instead of a continuum: All molecules undergo a random Brownian walk and diffuse in and out of the nanofluidic channel and a coupled reservoir. This results in pronounced fluctuations of the molecular number density in the detection volume [12]. These fluctuations are reflected in the recorded electrical current; they can directly be probed amperometrically. Molecular-level information is then collected from fluctuations in current-time traces. In particular, diffusion coefficients as well as specific dynamic adsorptivities were determined by analysis of the amplitude [13] and frequency spectrum [14, 15] of current fluctuations.

To date, nanogap sensors have exclusively been employed for the detection of archetypical organometallic or metal-organic compounds such as ferrocenes [16, 17] or catechol derivatives [8, 18, 19]; experiments were limited to conditions of a polar solvent (water or acetonitrile), a high concentration of fully dissociated background electrolyte, and analytes with typically only one possible electron-transfer process.

In the present chapter, we extend the application of nanogap sensors and stochastic amperometry to more complex analytes under less polar conditions. Within this context, ferrocenyl substituted thiophenes represent suitable molecules for such investigations, because the thiophene building block allows an easy functionalization with redox-active transition-metal-containing entities, and the resulting compounds are able to show several well-resolved one-electron transfer processes [20–25]. Furthermore, these heterocyclic systems are of interest regarding their potential application in molecular electronics or thiophene-based intrinsic conducting polymers (ICP) [25–36].

The nanogap geometry enables the determination of diffusion coefficients of these compounds as a function of specific oxidation states of redox couples. We were able to identify a trend of decreased diffusive transport for higher oxidations states. Moreover, we found that the analytes yield the highest currents per molecule for a three-electron transfer process.

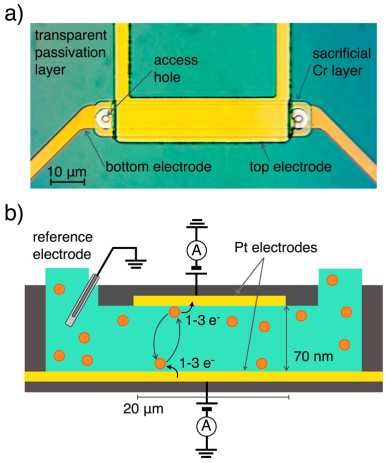

Figure 3.1: (a) Top-view optical micrograph of a nanofluidic electrochemical sensor. (b) Schematic cross section of the device and principle of operation of a nanogap sensor. Analyte molecules undergo redox cycling between the two electrodes. For different electrode potentials, redox cycling occurs between different oxidation states, and different numbers of electrons (1-3) are exchanged at each transfer process.

3.2. EXPERIMENTAL SECTION

Chemical Reagents and Nanofluidic Device Fabrication: 2,5-diferrocenyl thiophene (2,5-Fc_2-$^cC_4H_2S$) and 2,3,4-triferrocenyl thiophene (2,3,4-Fc_3-^cC_4HS) were synthesized in a Pd-promoted Negishi C,C cross-coupling reaction of 2,5-dibromothiophene or 2,3,4-tribromo-thiophene with ferrocenyl zinc chloride, as reported previously [22, 37–39]. As electrolyte, an 0.1 M solution of tetrabutylammonium tetrakis- (pentafluorophenyl)borate was used, whereby $[N^nBu_4][B\text{-}(C_6F_5)_4]$ was prepared by metathesis of lithium tetrakis (pentafluorophenyl) borate etherate (Boulder Scientific) with tetrabutylammonium bromide according to a published procedure and enhanced by a filtration step of the crude product through a pad of silica using dichloromethane as solvent [40].

Electrochemical nanogap devices were fabricated by cleanroom microfabrication on an oxidized silicon wafer substrate as described previously [41]. They consist of a 5 μm wide, 10-20 μm long, and 70 nm high nanochannel in silicon oxide/silicon nitride; the roof and ceiling of the channel are Pt electrodes. The length and width of the nanochannel are defined by photolithography; the nanoscale height is defined by evaporation of a sacrificial Cr layer sandwiched between two Pt layers, which were also defined and fabricated by photolithography and electron-beam deposition, respectively. After these three metal deposition steps, the structure was buried in a Si_3N_4/SiO_2 passivation layer by plasma-enhanced chemical vapor deposition. Access holes were subsequently plasma-etched into this layer to connect the nanodevice to a fluidic reservoir. Just before an experiment, the nanochannel was released by a selective wet-chemical etch of the sacrificial Cr layer (Cr etchant Selectipur, BASF). A micrograph and schematic view of a nanofluidic electrochemical device are shown in figure 3.1.

Electrochemical Instrumentation and Experimentation: Using a home-built potentiostat setup, two sensitive operational amplifiers (Femto DDCPA-300) were sepa-

rately connected to the top and bottom electrodes of a nanofluidic device. The amplifiers were LabView-controlled and used as current meters and voltage sources (figure 3.1B). A micromanipulator was used to position a reservoir in polydimethylsiloxane (PDMS) on top of the access holes. After the wet-etch of the chromium layer, the etchant was replaced by sulfuric acid (Sigma-Aldrich), prepared as a 0.5 M solution in Milli-Q water, and both Pt electrode surfaces were cleaned by repeatedly sweeping their potential between -0.15 and 1.2 V versus a Ag/AgCl reference electrode (BASi inc.) placed in the reservoir.

The PDMS reservoir was then replaced by a reservoir machined in polytetrafluoroethylene and connected to the nanochannel via an O-ring (fluorinated propylene monomer, 0.5 mm inner diameter). The reservoir and nanochannel were filled with the analyte-containing dichloromethane solution, and a double-junction Ag/Ag^+ reference electrode (BASi inc.) was immersed into the reservoir. This reference electrode was constructed from a silver wire inserted into a Luggin capillary with a Vycor tip containing a solution of 0.01 M [$AgNO_3$] and 0.1 M of the supporting electrolyte in acetonitrile. This Luggin capillary was inserted into a second Luggin capillary with Vycor tip filled with a 0.1 M supporting electrolyte solution in dichloromethane. The whole setup was shielded from interference in a Faraday cage.

3.3. RESULTS AND DISCUSSION

Cyclic Voltammetry: Cyclic voltammograms (CVs) of 2,5-diferrocenyl thiophene and 2,3,4 -triferrocenyl thiophene (1 mM in 0.1 M $[N^nBu_4][B(C_6F_5)_4]$ in dichloromethane) recorded at a Pt ultramicrodisk electrode (UME; BASi inc.) with a diameter of 10 μm are shown in figure 3.2. In a stepwise oxidation, the analytes exhibit two (or three, respectively) well-resolved electrochemically reversible one-electron transfer processes with equal heights of the current steps. This is in good agreement with previous results [37].

By determining the magnitude of the steady-state currents, we estimate the diffusion coefficients, D, of the fully reduced species to be $1.08 \times 10^{-9}\ m^2/s$ for 2,5-Fc_2-$^cC_4H_2S$ and $0.96 \times 10^{-9}\ m^2/s$ for 2,3,4-Fc_3-^cC_4HS. [Diffusion coefficients (D) were estimated by $i = 4nFcDr$, where i is the height of a current step, n the number of exchanged electrons, F Faraday constant, c the analyte concentration, and r the electrode radius [42]].

Cyclic Voltammetry in a Nanogap Device: Figure 3.3 shows voltammograms of both thiophene compounds recorded in a nanochannel device. The steps are not entirely as pronounced as for the measurements using the UME, which is most likely caused by the finite rate for heterogeneous electron transfer, as has been reported earlier for other redox couples [43]. Nonetheless, all electron-transfer processes are clearly resolved. In these measurements, one electrode was kept constant at 0 V, while the other electrode was swept with respect to the reference electrode. The curves depict the oxidation current at one electrode and the reduction current at the other working electrode. This means that the molecules undergo redox cycling with one, two, or three electrons per molecule being exchanged during each process. While in the device, each analyte molecule undergoes about 60 000 transfer processes per second. This leads to a considerable amplification of the current detected per molecule.

A difference in the measurements compared to the cyclic voltammetry at the UME is that the height of the current steps is reduced for an increasing magnitude of applied

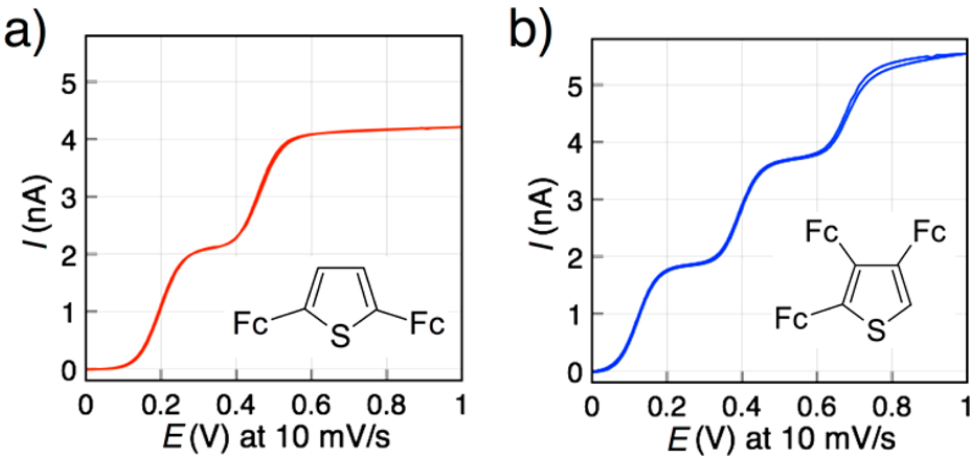

Figure 3.2: Cyclic voltammograms of 2,5-diferrocenylthiophene (left) and 2,3,4-triferrocenylthiophene (right) detected in dichloromethane solutions (1 mM) at a Pt ultramicroelectrode with a diameter of 10 μm (supporting electrolyte 0.1 M $[N^nBu_4][B(C_6F_5)_4]$).

potentials or oxidation states, respectively, as indicated by the gray bars in figure 3.3. This effect cannot be explained by a reduced diffusion coefficient of oxidized molecules or an effectively reduced diffusion due to dynamic adsorption; as such, a reduction is equilibrated by exchange (increase) in local concentration with the bulk reservoir [44].

We believe that the shape of the cyclic voltammograms recorded in the nanochannel is dictated by the finite rate for heterogeneous electron transfer, as has been reported earlier for other couples [43]. We estimated the electrochemical rate constants k_0. As shown in the dashed lines in figure 3.3, the forward sweeps of the CVs were fitted to the Butler-Volmer expression for thin layer cells [43], using a superposition of j one electron reactions:

$$i(E) = \sum_{j=1}^{2or3} \frac{i_{\mathrm{lim,j}}}{1 + exp[-f(E - E_{\mathrm{j}}^{0'})] + \frac{D_{\mathrm{eff}}}{z k_{\mathrm{j}}^{0}} exp[-(1-\alpha) f(E - E_{\mathrm{j}}^{0'})]} \tag{3.1}$$

Here $i_{lim,j}$ are limiting currents for the individual waves, $E_j^{0'}$ formal potentials, α the transfer coefficient, z = 70 nm the nanochannel height, and $f = F/RT$ (F, Faraday constant; R, gas constant; T, temperature). D_{eff} is the effective diffusion coefficient; diffusion is effectively slowed by dynamic analyte adsorption due to the high surface-to-volume ratio in the nanochannel of $3 \times 10^7\ m^{-1}$, typically to D_{eff} = 0.2-0.5D in previous experiments [11, 16]. The fitting parameters were i_{lim} and the dimensionless rate constant D_{eff}/zk^0. The transfer coefficient was approximated by α = 0.5 [43]. Formal potentials $E_{\mathrm{j}}^{0'}$ were determined as the inflection points of the CVs. Using the effective diffusion coefficients determined as shown below (see figure 3.4), rate constants were extracted. They decrease considerably with a higher electron number from 1.4 to 0.50 cm/s for 2,5-Fc_2-$^cC_4H_2S$ and from 0.40 to 0.18 to 0.07 cm/s for the 2,3,4-Fc_3-^cC_4HS compound for the first and second (and third) wave, respectively.

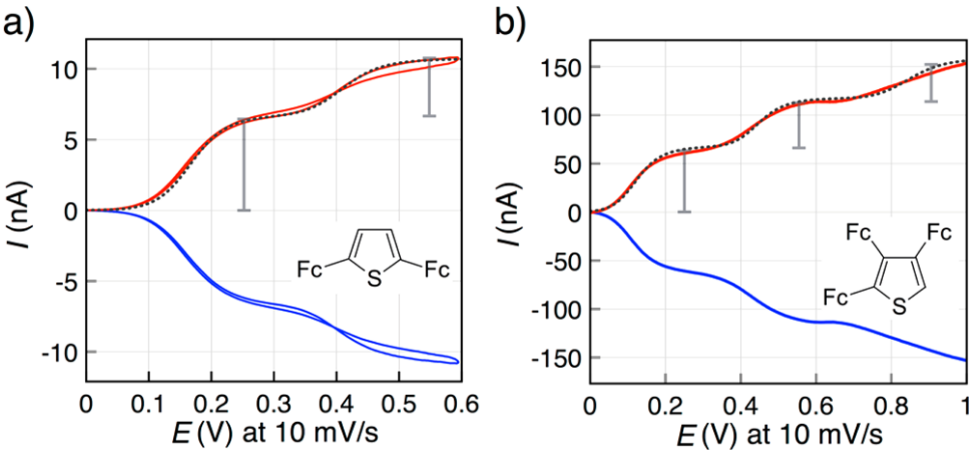

Figure 3.3: Cyclic voltammetry in the nanofluidic device. (a) 50 μM 2,5-Fc_2-$^cC_4H_2S$ in a 20 μm long device. The top electrode is swept (red), while the bottom electrode is kept at 0 V (blue). The dashed line is a fit to the Butler-Volmer formalism, equation 3.1. Gray bars indicate limiting currents determined by the same fit. (b) 1 mM 2,3,4-Fc_3-^cC_4HS in a 10 μm long device. Here the bottom electrode is swept (red), while the top electrode is kept constant at 0 V (blue).

Moreover, electrical migration might have an adverse effect on transfer kinetics and analyte transport perpendicular to the electrodes; this effect was previously studied in nanogap geometries [45–47]. $[N^nBu_4][B(C_6F_5)_4]$ has a large ionic dissociation constant $K_D > 1000$ [48]. Therefore, a thick electrical double layer of $\lambda_D > 10$ nm (at actual electrolyte ion concentrations < 0.1 mM) could lead to repulsion of charged analytes from charge electrodes and thereby to reduced limiting currents for higher oxidation states.

Stochastic Amperometry: We biased the electrodes a specific fixed potential, recorded current-time traces for both electrodes, and analyzed the mesoscopic number density fluctuations mirrored in the current fluctuations. In this detection scheme, the nanogap geometry offers the unique advantage that an arbitrary couple of oxidation states can be chosen for redox cycling between the two working electrodes. This means that also cycling between two positive oxidation states is possible, independent of the fully reduced bulk state.

Properties were analyzed by determining the magnitude of the fluctuations [13], *i.e.*, the standard deviation i_{std} and comparing it to the magnitude of the Faradaic limiting current $\langle i_{lim} \rangle$ for specific combination of electrode potentials. Here, i_{std} depends only on the current generated per molecule, i_p, and the mean number of analyte molecules $\langle N \rangle$ present in the detection volume:

$$i_{\mathrm{std}} = i_{\mathrm{p}} \langle N \rangle^{1/2} \tag{3.2}$$

The current per molecule, i_p, depends only on the nanochannel height, z; the number of electrons transferred, n; and the diffusivity, D_{eff} (and on the elementary charge, e):

$$i_{\mathrm{p}} = \frac{neD_{\mathrm{eff}}}{z^2} \qquad (n = 1,2,3) \tag{3.3}$$

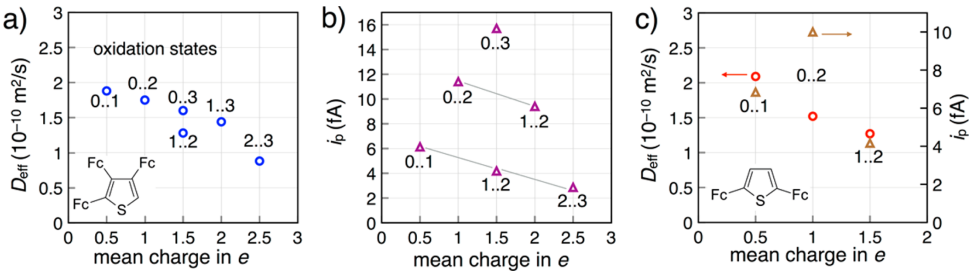

Figure 3.4: (a) Effective diffusion coefficient of 2,3,4-Fc_3-^cC_4HS determined by the magnitude of fluctuations i_{std} in current-time traces. The "mean charge in e" corresponds to the applied potentials $0.5e \widehat{=}$ 0-0.25 V; $1e \widehat{=}$ 0-0.5 V; $1.5e$ ("0..3") $\widehat{=}$ 0-0.9 V; $1.5e$ ("1..2") $\widehat{=}$ 0.25-0.5 V; $2e \widehat{=}$ 0.25-0.9 V; $2.5e \widehat{=}$ 0.5-0.9 V. (b) Corresponding currents per molecule for 2,3,4-Fc_3-^cC_4HS. The gray lines indicate one-electron (lower line) and two electron (upper line) transfer processes. (c) Effective diffusivities and currents per molecule for 2,5-Fc_2-$^cC_4H_2S$. Here the mean charge in e corresponds to the potentials $0.5e \widehat{=}$ 0-0.25 V; $1e \widehat{=}$ 0-0.55 V; $1.5e \widehat{=}$ 0.25-0.55 V.

By using equations 3.2 and 3.3 as well as the limiting current $\langle i_{lim} \rangle = i_p \langle N \rangle$, D_{eff} and i_p can directly be determined, *i.e.*, $i_p = i^2_{std} / \langle i_{lim} \rangle$. The results of this fluctuation analysis are shown in figure 3.4a. Here, the effective diffusion coefficient, D_{eff}, is plotted as a function of applied potential represented by the nominal "mean charge in e". This means that for a value of 0.5, the analyte 2,3,4-Fc_3-^cC_4HS cycles between the fully reduced state and a state with only one oxidized ferrocenyl group, potentials of 0 V and 250 mV are applied, and the molecules in the device have an average charge of about $0.5e$. Our measurements show unequivocally that the effective diffusivity decreases with increasing mean charge or with the mean of the potential applied at the top and bottom electrodes. Figure 3.4b shows the current per molecule, i_p, as determined by equation 3.3. This current increases with the number of electrons exchanged but decreases for higher oxidation numbers. In figure 3.4c, the same trends of smaller currents and diffusion coefficients for an increased mean charge are depicted for the 2,5-Fc_2-$^cC_4H_2S$ analyte.

D_{eff} can also be extracted from a current-time trace by determining its power spectral density and determining the characteristic crossover frequency, f_0 [14]. Both methods are compared in the Supporting Information, showing higher diffusivities for the latter methods but the same trend of reduced D_{eff} for higher potentials and charges.

The slightly faster diffusion of 2,5-Fc_2-$^cC_4H_2S$ compared to 2,3,4-Fc_3-^cC_4HS is expected because of its smaller size. The observed reduced diffusivities at higher oxidation states are also not unexpected. For example, the diffusion coefficient of ferrocenedimethanol in aqueous solution is reduced by 20% in its oxidized state [44] because of a changed solvation shell. In the case of the ferrocenylthiophenes, a similarly strong effect is not expected because of the very large size of the electrolyte ions in a nonpolar solvent. Several origins or a combination of effects can lead to the observed change in D_{eff}, namely, a change in bulk diffusivity, a change in dynamic adsorptivity, a slightly reduced limiting current due to slow kinetics, as well as a contribution by electrical migration. The increased D_{eff} for the spectroscopic determination compared to the current magnitude analysis (figure S2 in the Supporting Information) hints at an anisotropic contribution by migration which is captured in i_{std} but not in f_0 because only longitudinal diffusion contributes to the crossover frequency (shuttling in and out of the

nanochannel), while fluctuations on all time scales (including diffusion across the channel) are captured in i_{std}.

A change in electrostatic adsorption can be ruled out as a cause for the decreased effective diffusivity because more positively charged analytes would be repelled from more positively charged electrode surfaces, but a decrease in D_{eff} is observed for these conditions.

Ultimately, while clear trends are observed for D_{eff} and i_p, so far it is not possible to distinguish the contribution of adsorption and changed diffusivities to these observations. While transport is hindered in the nanochannel, very large currents per molecule of up to 15 fA at room temperature were measured for high overpotentials (figure 3.4b). This shows that compounds exhibiting multielectron transfer processes can have a potential application in single-molecule electrochemistry.

3.4. CONCLUSION

We introduced a new electrochemical method to determine the diffusive properties as a function of the oxidation state of complex electrochemically active molecules in a stochastic amperometric measurement. The experiments show that electrochemical nanogap sensors are suitable to work under conditions of a very volatile solvent, enabling a more complex analysis of novel compounds. For the investigated oligoferrocenyl thiophenes, our measurements show a decrease in effective diffusivity for an increase in applied potentials and oxidation state of the compounds. Moreover, highest currents per molecule of 15 fA per molecule were determined, which compares well to previous single-molecule experiments [17]. For future experiments, we plan to investigate the origins of changes in effective diffusivity by determining the influence of electrical migration as well as to extend the method from identifying the properties of a redox couple to determining the diffusion of a specific oxidation state.

REFERENCES

[1] K. Mathwig, H. R. Zafarani, J. M. Speck, S. Sarkar, H. Lang, S. G. Lemay, L. Rassaei, and O. G. Schmidt, *Potential-dependent stochastic amperometry of multiferrocenylthiophenes in an electrochemical nanogap transducer,* The Journal of Physical Chemistry C **120**, 23262 (2016).

[2] J. M. Rothberg, W. Hinz, T. M. Rearick, J. Schultz, W. Mileski, M. Davey, J. H. Leamon, K. Johnson, M. J. Milgrew, M. Edwards, *et al., An integrated semiconductor device enabling non-optical genome sequencing,* Nature **475**, 348 (2011).

[3] A. T. Sage, J. D. Besant, B. Lam, E. H. Sargent, and S. O. Kelley, *Ultrasensitive electrochemical biomolecular detection using nanostructured microelectrodes,* Accounts of chemical research **47**, 2417 (2014).

[4] C. Laborde, F. Pittino, H. Verhoeven, S. Lemay, L. Selmi, M. Jongsma, and F. Widdershoven, *Real-time imaging of microparticles and living cells with cmos nanocapacitor arrays,* Nature nanotechnology **10**, 791 (2015).

[5] L. Rassaei, P. S. Singh, and S. G. Lemay, *Lithography-based nanoelectrochemistry,* (2011).

[6] P. S. Singh, *From sensors to systems: Cmos-integrated electrochemical biosensors,* IEEE Access **3**, 249 (2015).

[7] K. Mathwig, T. Albrecht, E. D. Goluch, and L. Rassaei, *Challenges of biomolecular detection at the nanoscale: nanopores and microelectrodes,* Analytical chemistry **87**, 5470 (2015).

[8] L. Rassaei, K. Mathwig, S. Kang, H. A. Heering, and S. G. Lemay, *Integrated biodetection in a nanofluidic device,* ACS nano **8**, 8278 (2014).

[9] K. Dawson and A. O'Riordan, *Electroanalysis at the nanoscale,* Annual Review of Analytical Chemistry **7**, 163 (2014).

[10] M. A. Zevenbergen, D. Krapf, M. R. Zuiddam, and S. G. Lemay, *Mesoscopic concentration fluctuations in a fluidic nanocavity detected by redox cycling,* Nano letters **7**, 384 (2007).

[11] E. Kätelhön, B. Hofmann, S. G. Lemay, M. A. Zevenbergen, A. Offenhäusser, and B. Wolfrum, *Nanocavity redox cycling sensors for the detection of dopamine fluctuations in microfluidic gradients,* Analytical chemistry **82**, 8502 (2010).

[12] K. Krause, K. Mathwig, B. Wolfrum, and S. Lemay, *Brownian motion in electrochemical nanodevices,* The European Physical Journal Special Topics **223**, 3165 (2014).

[13] P. S. Singh, H.-S. M. Chan, S. Kang, and S. G. Lemay, *Stochastic amperometric fluctuations as a probe for dynamic adsorption in nanofluidic electrochemical systems,* Journal of the American Chemical Society **133**, 18289 (2011).

[14] M. A. Zevenbergen, P. S. Singh, E. D. Goluch, B. L. Wolfrum, and S. G. Lemay, *Electrochemical correlation spectroscopy in nanofluidic cavities,* Analytical chemistry **81**, 8203 (2009).

[15] K. Mathwig, D. Mampallil, S. Kang, and S. G. Lemay, *Electrical cross-correlation spectroscopy: Measuring picoliter-per-minute flows in nanochannels,* Physical review letters **109**, 118302 (2012).

[16] D. Mampallil, K. Mathwig, S. Kang, and S. G. Lemay, *Reversible adsorption of outer-sphere redox molecules at pt electrodes,* The journal of physical chemistry letters **5**, 636 (2014).

[17] S. Kang, A. F. Nieuwenhuis, K. Mathwig, D. Mampallil, and S. G. Lemay, *Electrochemical single-molecule detection in aqueous solution using self-aligned nanogap transducers,* ACS nano **7**, 10931 (2013).

[18] B. Wolfrum, M. Zevenbergen, and S. Lemay, *Nanofluidic redox cycling amplification for the selective detection of catechol,* Analytical chemistry **80**, 972 (2008).

[19] Y. Kanno, K. Ino, H. Shiku, and T. Matsue, *A local redox cycling-based electrochemical chip device with nanocavities for multi-electrochemical evaluation of embryoid bodies,* Lab on a Chip **15**, 4404 (2015).

[20] M. Iyoda, T. Kondo, T. Okabe, H. Matsuyama, S. Sasaki, and Y. Kuwatani, *A simple and efficient synthesis of di-, tri-, and tetraferrocenylarenes,* Chemistry letters **26**, 35 (1997).

[21] B. Jin, F. Tao, and P. Liu, *Rapid-scan time-resolved ft-ir spectroelectrochemistry–study on the electron transfer of ferrocene-substituted thiophenes,* Journal of Electroanalytical Chemistry **624**, 179 (2008).

[22] A. Hildebrandt, D. Schaarschmidt, R. Claus, and H. Lang, *Influence of electron delocalization in heterocyclic core systems on the electrochemical communication in 2, 5-di-and 2, 3, 4, 5-tetraferrocenyl thiophenes, furans, and pyrroles,* Inorganic chemistry **50**, 10623 (2011).

[23] J. M. Speck, D. Schaarschmidt, and H. Lang, *Atropisomeric 3, 3, 4, 4, 5, 5-hexaferrocenyl-2, 2-bithiophene: Synthesis, solid-state structure, and electrochemistry,* Organometallics **31**, 1975 (2012).

[24] A. Hildebrandt, T. Ruffer, E. Erasmus, J. C. Swarts, and H. Lang, *A star-shaped supercrowded 2, 3, 4, 5-tetraferrocenylthiophene: Synthesis, solid-state structure, and electrochemistry,* Organometallics **29**, 4900 (2010).

[25] A. Hildebrandt and H. Lang, *(multi) ferrocenyl five-membered heterocycles: excellent connecting units for electron transfer studies,* Organometallics **32**, 5640 (2013).

[26] A. J. Heeger, *Semiconducting and metallic polymers: the fourth generation of polymeric materials (nobel lecture),* Angewandte Chemie International Edition **40**, 2591 (2001).

[27] A. G. MacDiarmid, *"synthetic metals": A novel role for organic polymers (nobel lecture),* Angewandte Chemie International Edition **40**, 2581 (2001).

[28] D. Zhang, K. Ryu, X. Liu, E. Polikarpov, J. Ly, M. E. Tompson, and C. Zhou, *Transparent, conductive, and flexible carbon nanotube films and their application in organic light-emitting diodes,* Nano letters **6**, 1880 (2006).

[29] Y. H. Kim, J. Lee, S. Hofmann, M. C. Gather, L. Müller-Meskamp, and K. Leo, *Achieving high efficiency and improved stability in ito-free transparent organic light-emitting diodes with conductive polymer electrodes,* Advanced Functional Materials **23**, 3763 (2013).

[30] J. Roncali, P. Blanchard, and P. Frère, *3, 4-ethylenedioxythiophene (edot) as a versatile building block for advanced functional π-conjugated systems,* Journal of Materials Chemistry **15**, 1589 (2005).

[31] F. Paul and C. Lapinte, *Organometallic molecular wires and other nanoscale-sized devices: an approach using the organoiron (dppe) cp* fe building block,* Coordination chemistry reviews **178**, 431 (1998).

[32] M. D. Ward, *Metal-metal interactions in binuclear complexes exhibiting mixed valency; molecular wires and switches,* Chemical Society Reviews **24**, 121 (1995).

[33] M. Akita and T. Koike, *Chemistry of polycarbon species: from clusters to molecular devices,* Dalton Transactions , 3523 (2008).

[34] A. Ceccon, S. Santi, L. Orian, and A. Bisello, *Electronic communication in heterobinuclear organometallic complexes through unsaturated hydrocarbon bridges,* Coordination chemistry reviews **248**, 683 (2004).

[35] F. Barigelletti and L. Flamigni, *Photoactive molecular wires based on metal complexes,* Chemical Society Reviews **29**, 1 (2000).

[36] S. Barlow and D. O'Hare, *Metal- metal interactions in linked metallocenes,* Chemical reviews **97**, 637 (1997).

[37] J. M. Speck, R. Claus, A. Hildebrandt, T. Ruffer, E. Erasmus, L. van As, J. C. Swarts, and H. Lang, *Electron transfer studies on ferrocenylthiophenes: Synthesis, properties, and electrochemistry,* Organometallics **31**, 6373 (2012).

[38] J. M. Speck, M. Korb, T. Ruffer, A. Hildebrandt, and H. Lang, *Substituent influence on charge transfer interactions in α, α-diferrocenylthiophenes,* Organometallics **33**, 4813 (2014).

[39] E. A. Poppitz, A. Hildebrandt, M. Korb, D. Schaarschmidt, and H. Lang, *Synthesis, properties, and electron transfer studies of ferrocenyl thiophenes,* Zeitschrift für anorganische und allgemeine Chemie **640**, 2809 (2014).

[40] J. M. Speck, M. Korb, A. Schade, S. Spange, and H. Lang, *Ferrocenes bridged by ethylenediamino thiophene: Varying charge transfer properties in a series of 3, 4-di-n-substituted 2, 5-diferrocenyl thiophenes,* Organometallics **34**, 3788 (2015).

[41] K. Mathwig and S. G. Lemay, *Pushing the limits of electrical detection of ultralow flows in nanofluidic channels,* Micromachines **4**, 138 (2013).

[42] K. Aoki, *Theory of ultramicroelectrodes,* Electroanalysis **5**, 627 (1993).

[43] M. A. Zevenbergen, B. L. Wolfrum, E. D. Goluch, P. S. Singh, and S. G. Lemay, *Fast electron-transfer kinetics probed in nanofluidic channels,* Journal of the American Chemical Society **131**, 11471 (2009).

[44] D. Mampallil, K. Mathwig, S. Kang, and S. G. Lemay, *Redox couples with unequal diffusion coefficients: effect on redox cycling,* Analytical chemistry **85**, 6053 (2013).

[45] W. Hyk and Z. Stojek, *Thin and ultra-thin layer dual electrode electrochemistry: theory of steady-state voltammetry without supporting electrolyte,* Electrochemistry Communications **34**, 192 (2013).

[46] J. Xiong, Q. Chen, M. A. Edwards, and H. S. White, *Ion transport within high electric fields in nanogap electrochemical cells,* (2015).

[47] Q. Chen, K. McKelvey, M. A. Edwards, and H. S. White, *Redox cycling in nanogap electrochemical cells. the role of electrostatics in determining the cell response,* The Journal of Physical Chemistry C **120**, 17251 (2016).

[48] R. J. LeSuer, C. Buttolph, and W. E. Geiger, *Comparison of the conductivity properties of the tetrabutylammonium salt of tetrakis (pentafluorophenyl) borate anion with those of traditional supporting electrolyte anions in nonaqueous solvents,* Analytical chemistry **76**, 6395 (2004).

3.5. SUPPORTING INFORMATION

Electrochemical correlation spectroscopy:

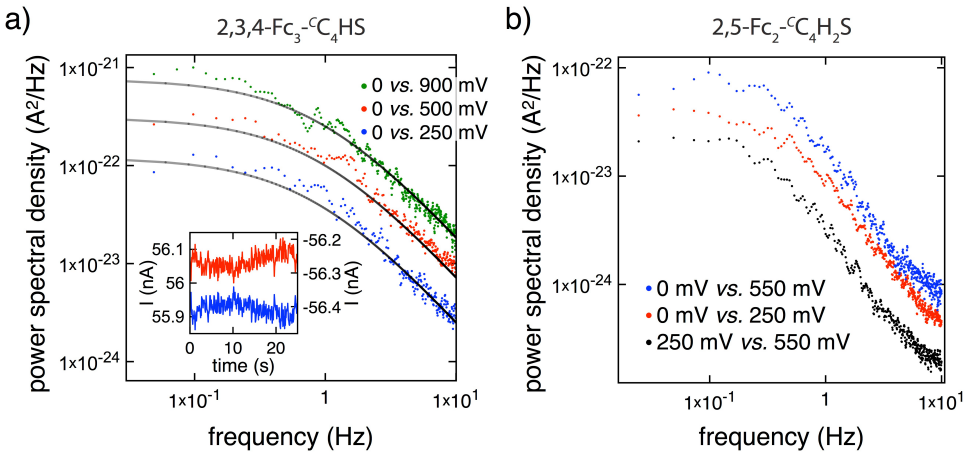

Figure S1. Power spectral densities (PSDs). a) PSDs for oxidation potentials of 0.9 V, 0.5 V and 0.25 V for 0.5 mM 2,3,4-Fc_3-^cC_4HS undergoing redox cycling in a 10 μm long device (the reduction potential is kept at 0 V). Gray lines are a fit to the theoretical model. Inset: raw current-time traces for potentials of 0.25 V and 0.9 V and the top and bottom electrode, respectively. b) Power spectra for 10 mM 2,5-Fc_2-$^cC_4H_2S$ in a 20 μmm long device.

Exemplary power spectra extracted from current-time traces measured in a nanofluidic device are shown in figure S1. Traces were recorded for a length of 60 s (100 s for 2,5-Fc_2-$^cC_4H_2S$ at a bandwidth of 150 Hz. Low-frequency drift was filtered, and spectra of three current-time traces were averaged for each depicted power spectrum. The PSDs *S(f)* can be characterized by two characteristic properties: the magnitude of the plateau at lower frequencies, which for a given geometry and diffusion coefficient depends only on the analyte concentration, and the crossover frequency f_0, which indicates the transition from the plateau at lower frequencies to a $f^-3/2$ decay at high frequencies [14]. The value of f_0 was extracted by a fit to $S(f) = S_0/(1+(f/f_0)^{3/2})$ and D_{eff} evaluated using $f_0 = (D_{eff}/\pi)(3/L^2{}_a(L_a+6L_e)))^{2/3}$. Here L_a is the top electrode length and $L_e = 2$ μm is the distance between the access holes and the top electrode). Figure S2 shows corresponding diffusivities for 2,5-Fc_2-$^cC_4H_2S$ in comparison to D_{eff} determined by evaluating the current fluctuation magnitude (as shown also in figure 3.4c).

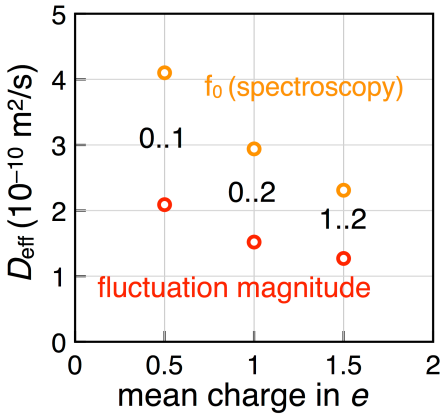

Figure S2. Comparison of D_{eff} of 2,5-Fc_2-$^{c}C_4H_2S$ calculated by determining i_{std} and the crossover frequency f_0 of the power spectral density of a current-time trace.

4

ELECTROCHEMICAL REDOX CYCLING IN A NEW NANOGAP SENSOR: DESIGN AND SIMULATION

We propose a new geometry for nanogap electrochemical sensing devices. These devices consist of two closely spaced side-by-side electrodes which work under redox cycling conditions. Using finite element simulations, we investigate the effects of different geometric parameters on the redox cycling signal amplification to gain insight into the electrochemical sensing performance of the device design. This will allow optimizing the sensor performance of devices to be fabricated in the future.

This chapter is based on the following publication:

H.R. Zafarani, K. Mathwig, E.J.R. Sudhölter and L. Rassaei, Journal of Electroanalytical Chemistry **2016**, *760* , 42–47 [1].

4.1. INTRODUCTION

MICRO/NANOELECTRODE systems have been extensively studied for electrochemical (bio)sensing applications due to their fast response time, small capacitive currents and steady-state voltammetric response, which compare favorably to macroelectrode systems [2]. However, the small surface area of these electrodes limits their sensitivity, in particular at low analyte concentrations, due to the limited sensitivity of electronic instrumentation [3]. One way to circumvent these limitations is to configure the electrodes in a dual mode, thereby taking advantage of redox cycling between them. In this way, the concentration profiles of both species overlap, allowing the species generated at one electrode to be efficiently collected at the other electrode. Such successive oxidation and reduction of analyte molecules as a result of the inter-diffusion between two closely spaced electrodes lead to current amplification and, thus, the detection limit of electrochemical sensors is lowered [4–6]. These systems are a modified version of rotating ring disc electrodes operating in generator–collector mode which were in particular developed by Albery and Hitchman [7, 8] followed by the development of numerous electrode geometries and techniques such as double-band channel electrodes [9], micro-ring-disc electrodes [10], micro-electrode arrays [11], interdigitated electrodes [12], dual microdisc electrodes [13], and junction electrodes [14]. A summary of the variety of geometries and applications can be found in reference [15].

The advantages of the redox cycling devices are not only limited to an improvement of the sensor sensitivity by amplification of faradic currents [12, 16]; they are also powerful tools for determining diffusion coefficients of redox species [9, 17] and monitoring the lifetime of electrogenerated intermediates [18, 19]. One widely used type of redox cycling devices is thin layer cells which consist of two planar electrodes separated by a thin layer of liquid [20]. Recently, Marken *et al.* developed a simple method for the preparation of dual-plate electrode systems with a micrometer gap via etching a thin epoxy layer between the two electrodes [21–23]. Despite the advantage of a simple and innovative fabrication methodology, the gap size is limited to the micrometer length scale, and the method is not compatible mass fabrication needed for many practical applications. The sensitivity of any thin layer cell sensor is increased by reducing the gap size between the two electrodes [22]. However, reducing the gap size to the nanometer range requires cleanroom facilities and multi-step photo or e-beam lithography techniques [20] as demonstrated in pioneering works by Lemay *et al.* [24, 25]. In this approach, nanogap devices are fabricated layer-by-layer. Subsequent to the microfabriation, a sacrificial chromium layer separating to metal electrodes is wet-etched, creating a nanochannel and completing the formation of the nanogap sensor. The sensitivity of these nanogap devices allows even single-molecule detection [26, 27], and they have been used for a variety of applications [25, 28, 29]. Considering the need for more sensitive sensing devices, there exists a demand for new nanogap sensors which are simpler to fabricate. Various geometries and fabrication method have been suggested in last few years [5, 30]. We currently aim at the fabrication of a new type of nanogap sensor consisting of two closely spaced side-by-side electrodes. Comparable redox-cycling sensors with side-by-side electrodes have been realized by a variety of fabrication methods using different electrode materials [31–33]. All of these sensors employ side-by-side electrodes in interdigitated geometries. However, they operate in a microscale regime with gap sizes

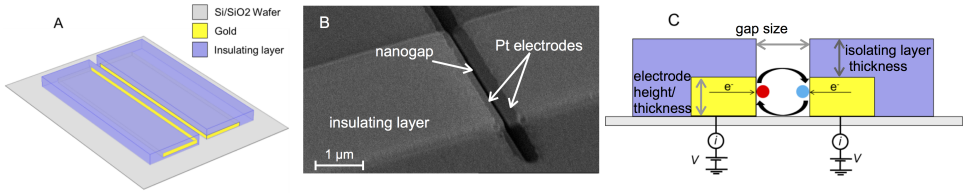

Figure 4.1: (A) Schematic of the proposed nanogap sensor, (B) scanning electron micrograph of a precursor of a device acquired at a 30° angle, and (C) schematic side view.

above 1 μm and, thus, do not benefit from the unique advantages of nanoscale sensors such as highest amplification factors. Side-by-side interdigitated electrodes with sub-micrometers distances have been fabricated, but only employed for impedance sensing [34].

In the present work, we employ numerical finite element simulations to study the electrochemical sensing behavior in a new nanogap design. By evaluating the influence of geometric parameters as well as electrode potentials on the sensor performance an understanding of design rules is gained for future device fabrication.

4.2. METHODS

Sensor geometry: The nanogap sensor consists of two closely spaced electrodes positioned next to each other (see figure 4.1). The top sides of both electrodes are passivated to avoid a contribution to the electrochemical signal.

COMSOL Multiphysics (version 4.4) was employed to simulate the electrochemical processes and mass transport of analytes in the nanogap sensor. We assume an unstirred solution (with the exception in the flow rate study section) and a high supporting electrolyte concentration. Therefore mass transport is diffusive, and convection and migration are not considered. The effects of various design parameters, namely the gap size, the thickness of the top isolating layer, the electrode thickness, the collector potential and the flow rate were studied, and their influence on the current signal and the signal amplification factor was determined.

The geometry of the device allows simplifying the simulation to a two–dimensional geometry. Fick's second law describes diffusion of species:

$$\frac{\partial C_j}{\partial t} = D_j \nabla^2 C_j \tag{4.1}$$

C_j and D_j are the concentration and diffusion coefficient of a redox species j. For simplicity, we consider equal diffusion coefficients for both oxidized and reduced species (see Table 4.1).

Electrochemical reactions: The archetypical redox reaction,

$$Fc(MeOH)_2{}^+ + e^- \rightleftarrows Fc(MeOH)_2 \tag{4.2}$$

was simulated at the electrode surfaces. The current was defined based on Butler–Volmer kinetics as [35]

$$i = F[c_O k_f - c_R k_b] \tag{4.3}$$

Table 4.1: Constants used in the current simulation processes [24, 30].

D_O	$6.7 \times 10^{-10} m^2/s$	α	0.49
D_R	$6.7 \times 10^{-10} m^2/s$	F	96485.34 C/mol
k_o	0.06 m/s	R	8.31 J/K
E_h	0.251 V *vs.* Ag/AgCl	T	298 K

$$k_f = k_0 e^{[\frac{-\alpha F(E-E_h)}{RT}]} \tag{4.4}$$

$$k_b = k_0 e^{[\frac{(1-\alpha)F(E-E_h)}{RT}]} \tag{4.5}$$

Here, k_f and k_b are the forward (reduction) and backward (oxidation) rate constants of a redox reaction, k_0 is the standard electrochemical rate constant, α: transfer coefficient, F: Faraday constant, E: electrode potential, E_h standard potential of the redox couple, c_O and c_R concentration of the oxidized and reduced species, respectively.

Model geometry: In our simulation, two electrodes are considered with variable thicknesses and a 3 μm width(*i.e.*, the length of the gap in the third dimension which is not simulated explicitly). The electrodes are located at close distance next to each other. An isolating layer is considered above each electrode with a defined thickness. Finally, a solution containing 1 mM $Fc(MeOH)_2$ infills the gap and a reservoir above the device. All potentials are defined versus a Ag/AgCl reference electrode.

Table 4.1 lists the value of the constants used in the simulation based on experimental values reported in the literatures [24, 30]. However, the choice of the electrolyte as well as the electrode material and electrode surface conditions can affect these constants [25, 36]. In all dual mode studies, the right electrode (generator) was swept in the potential range of 0–0.5 V *vs.* Ag/AgCl, while the left electrode (collector) was kept constant at a cathodic potential (0 V, except for studying the effect of varied collector potentials section). Under these conditions, the oxidized species are produced at the generator electrode, the majority of this species is reduced again at the collector electrode and then diffuses back to the generator electrode for re-oxidation.

4.3. RESULTS AND DISCUSSION

Study of the gap size: One important feature in the design of nanogap sensors is the distance between the two electrodes [29, 37]. Reducing the gap size enhances the current amplification due to a shorter diffusion time between the two electrodes [24, 38]. Thus, we studied this effect on the current amplification factor, which we defined as the ratio between the generator limiting current in dual mode to the current in single mode. (As shown in the cyclic voltammograms in figure 4.2 the single-mode currents exhibit a slight hysteresis due to slow diffusion into the nanogap. We approximated the limiting current by the current at a potential of 0.5 V.) We also studied the effect on the collection efficiency (defined as the current ratio of the collector electrode to the generator electrode in dual mode; collection efficiency = $I_{collector}/I_{generator}$. In these simulations, the

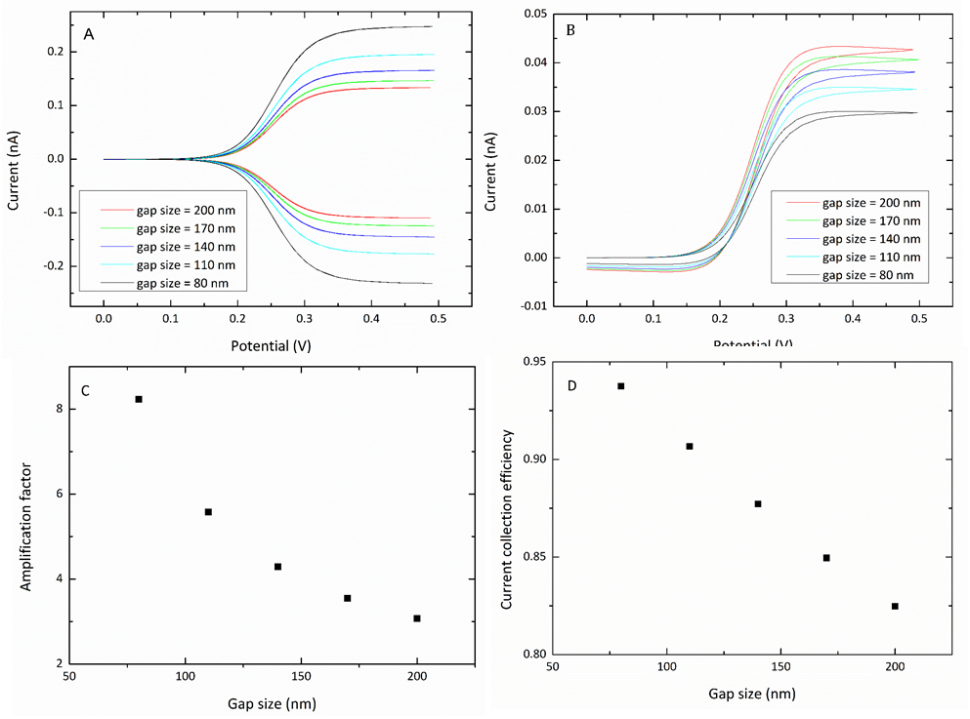

Figure 4.2: (A) Simulated cyclic voltammograms (scan rate = 10 mVs^{-1}) showing the effect of the distance between the two electrodes (gap size) in redox cyclic mode (the generator electrode was swept between 0 and 0.5 V while the collector potential was kept constant at 0 V). (B) Cyclic voltammograms (scan rate: 10 mVs^{-1}) showing the effect in single mode (one electrode was swept between 0 and 0.5 V while the other electrode was kept floating). (C) Plot showing the change in current amplification factor versus gap size in redox cyclic mode, and (D) plot showing the current collection efficiency versus the gap size in redox cyclic mode.

electrodes' thickness was chosen as 80 nm and the thickness of the top isolating layer was kept constant (250 nm). We simulated cyclic voltammograms of $Fc(MeOH)_2$ for different gap sizes (80 to 200 nm). As shown in Fiure 4.2A, decreasing the gap size results in an increase in both anodic and cathodic limiting current in agreement with reports in the literature. This increase is due to a reduced diffusion path between the two electrodes and, thus, more efficient redox cycling [29]. Figure 4.2B presents simulated cyclic voltammograms for varied gap sizes in single mode. Interestingly, in single mode a decrease in current is found with decreasing gap size; this is attributed to slower diffusive transport from the reservoir into the narrower nanochannel. As shown in figure 4.2C and D, decreasing the gap size results in both a higher amplification factor and a higher current collection efficiency in dual mode.

Study of the isolating layer thickness: The role of the top isolating layer thickness was studied by varying the thickness in the range of 100 nm to 300 nm for a 80 nm wide nanogap (electrode layer thickness = 80 nm). Here, again, the potential of one electrode was swept from 0 to 0.5 V (scan rate of 10 mVs^{-1}) while the potential of the other electrode

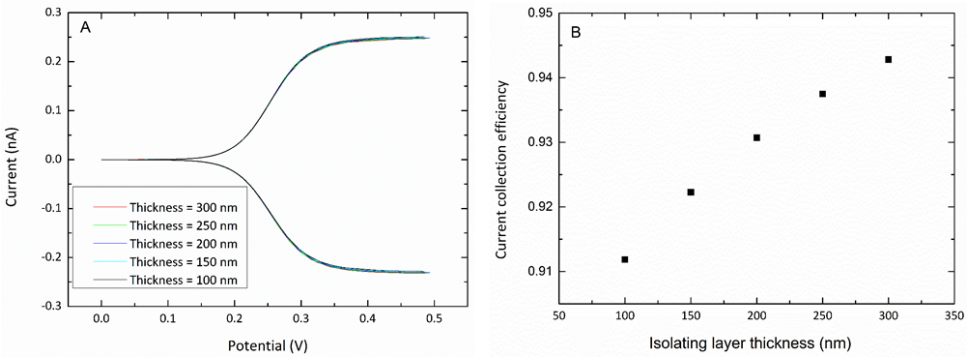

Figure 4.3: (A) Cyclic voltammograms (scan rate: 10 mVs^{-1}) showing the effect of the isolating layer thickness on the current obtained in the redox cyclingmode. (B) Current collection efficiency versus different isolating layer thicknesses in redox cyclic mode. (The generator electrode was swept between 0 and 0.5 V, and the collector potential was kept constant at 0 V).

was kept constant at 0 V for the oxidation and reduction of 1 mM $Fc(MeOH)_2$. As shown in figure 4.3A, a change in the thickness of the top isolating layer does not affect the magnitude of the limiting current in dual mode, whereas increasing the isolating layer thickness from 100 nm to 300 nm decreases the limiting current in single mode from 0.045 nA to 0.025 nA (data not shown). This demonstrates that the diffusive access to the electrodes is slowed down by a thick isolating layer; however, this has no influence on the redox cycling efficiency as species between the two electrodes undergo repeated electron transfer processes.

Figure 4.3B shows the trend of increasing current collection efficiency with increasing thickness of the top isolating layer due to the confinement of the redox species in the nanogap. Hence, the probability for diffusion of active species in the nanochannel back into the bulk reservoir decreases by increasing the thickness of the nanogap trench.

Study of the electrode thickness: Originally, Anderson and Reilley estimated the limiting current I for two planar electrodes separated by a thin layer of fluid by the equation [38]:

$$I = \frac{nFADC}{z} \tag{4.6}$$

Here A is the overlapping area between the two electrodes, and z is distance between the electrodes (gap size). Thus, by increasing the electrode surface areas the redox cycling current is increased. We studied the influence of the electrode surface areas in the our nanogap design by varying their height (layer thickness) in the range from 30 to 130 nm in a device with a 80 nm gap size and a 250 nm isolating layer on top (see figure 4.4).

Increasing the electrode thickness from 30 to 130 nm enhanced the limiting current from 0.1 to 0.38 nA linearly (in agreement with equation 4.6). As shown above in figure 4.3A, an enhanced species trapping due to the elevated electrodes does not improve the redox cycling current.

Study of the collector potential: In addition to the geometric parameters of the nanogap design we investigated the effect of the collector potential on the redox cycling current. We kept the collector electrode potential constant at values ranging from −0.5 to

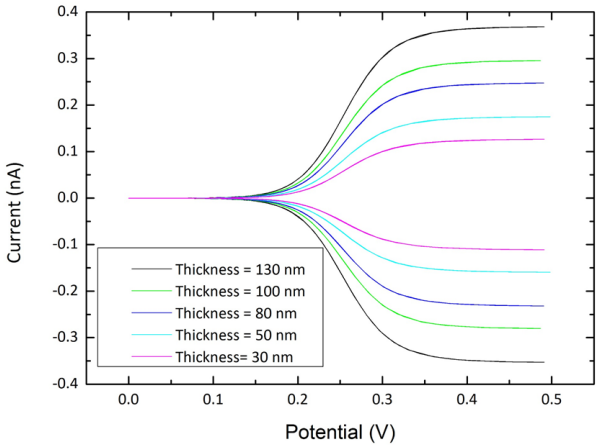

Figure 4.4: Cyclic voltammograms (scan rate: 10 mVs^{-1}) showing the effect of different electrode thicknesses on the redox cycling current (the collector electrode is kept constant potential of 0 V).

0.2 V while the generator electrode potential was swept between 0 and 0.5 V in a 80 nm nanogap device with a 250 nm isolating layer thickness and an 80 nm electrode thickness. The effect of these changes on the cyclic voltammograms is shown in figure 4.5.

The concentration profiles in the nanogap device are shown in figure 4.6 for two different collector potentials. When the collector potential is set at 0.2 V, close to the half-wave potential, a small amount of $Fc(MeOH)_2^+$ is reduced at the collector electrode which results in a decrease in redox cycling current. However, by shifting the potential of the collector electrode to a more cathodic potential, more $Fc(MeOH)_2^+$ ions are reduced at the electrode and diffuse to the generator electrode where they are re-oxidized resulting in an increase in the limiting current. Further decreasing the potential of the collector electrode from 0 to -0.5 V does not affect the redox cycling current (see figure 4.5). This indicates that a potential of 0 V suffices to reduce the species produced at generator electrode back to its initial state. Such high over potentials ensure that charge transfer does not limit the reaction rate [39].

Study of the flow rate: Contributions of both migration and convection to analyte mass transport were neglected in the simulations presented above. The proposed device can be implemented as a detection element in a microfluidic channel for improved sensitivity in microanalytical systems.

In microanalytical systems employing microelectrodes, the magnitude of the current typically depends on the solution flow rate, and the obtained signal has to be normalized to the hydrodynamic flow velocity. This is due to a strong dependence on mass transport to the electrode on the flow rate (and the channel cross section). Recently, we investigated the effect of the flow rate on the performance of a nanofluidic sensor located in a microchannel [40]. The investigated nanofluidic in that study, has a closed layer-by-layer structure [24, 25] where the solution introduced to the nanochannel- the gap between the top and the bottom electrode- via two small (2 μm by 2 μm) access holes. In this case changing the solution flow rate on the top of the nanofluidic had no influ-

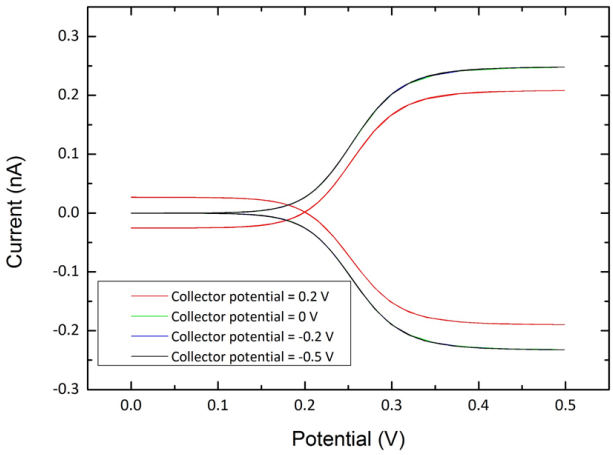

Figure 4.5: Cyclic voltammograms showing the effect of different collector potentials. The generator electrode is swept between 0 and 0.5 V (scan rate: 10 mVs^{-1}); the collector electrode is kept at different constant potentials.

ence on the sensor limiting current response. While in this study there is a nanochannel which is open on the top and the nanochannel is directly in contact with the above bulk solution. We want to study the effect of the flow rate on the performance of such an open nanofluidic sensor.

For this study, the nanogap sensor was located at the bottom of a microchannel (3 mm length, 200 μm height and 300 μm in width), a laminar flow was introduced perpendicular to the nanogap (*i.e.*, from left to right for the representation in figure 4.6). We evaluated the flow profile by using the Stokes equations for an incompressible fluid.

$$\vec{\nabla} p = \eta \nabla^2 \vec{u}, \quad \vec{\nabla}.\vec{u} = 0 \tag{4.7}$$

Here $\vec{u}$ is the flow velocity, p is the hydrostatic pressure, and η is the dynamic viscosity (0.001 Pa.s for water). We chose the boundary conditions of a constant laminar inflow rate at the microchannel inlet, $p = 0$ Pa at the outlet, and no-slip conditions for all other boundaries. The redox cycling current was determined as a function of flow ranging from rates of 0 to 600 μls^{-1} for the flow profile in the microchannel for a 80 nm nanogap (with a 250 nm isolating layer and 80 nm electrode thickness). Figure 4.7A presents cyclic voltammograms for various flow rates. At the center of the channel floor, these rates correspond to shear rates (flow velocity gradients ranging from 0 to 8600 s^{-1} as determined by $\frac{\partial v_x}{\partial z}(z=0) = \frac{6}{h^2 w - 0.63 h^3} Q$. (Here, $\frac{\partial v_x}{\partial z}$ is the shear rate [41], Q is the volume flow rate, h and w are the height and width of the microchannel, respectively.)

Previously, we showed that increasing the flow rate in a microchannel on top of a nanofluidic gap sensor does not affect the redox cycling signal [40, 42]. Since diffusion of species between the electrodes in the nanogap is fast in redox cycling, a variation of flow rate in micro-channel – considering also the large hydrodynamic resistance of the nanogap – does not alter the redox cycling current. Figure 4.7A reveals that, even with the open nanochannel geometry studied here, the electrochemical redox cycling

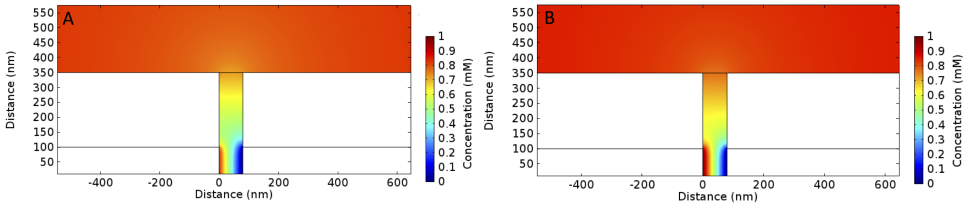

Figure 4.6: Concentration profile for the reduced species in a 80 nm nanogap devicewith a 250 nm isolating layer. The right electrode is set at 0.5 V, and the left electrode is set at (A) 0.2 V and (B) 0 V. The nanogap device connects to a reservoir on top with a bulk concentration of 1 mM $Fc(MeOH)_2$.

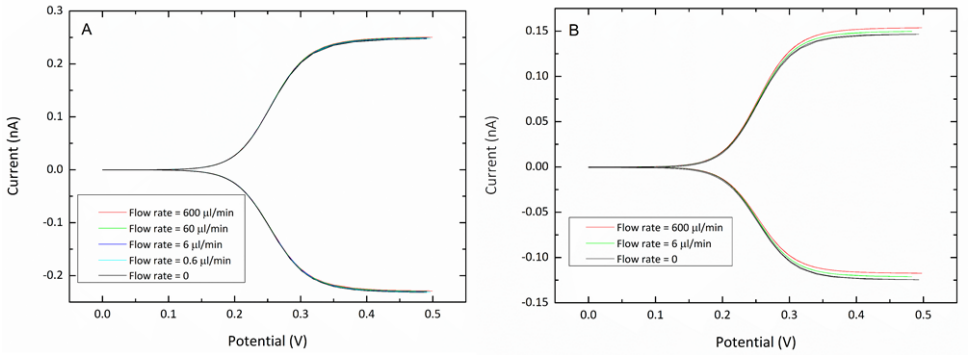

Figure 4.7: Cyclic voltammograms (scan rate: 10 mVs^{-1}) showing the effect of flow rate on the redox cycling current in the nanogap with (A) 80 nm gap size and (B) 170 nm gap size located in a microchannel. The potential of the generator electrode was swept between 0 and 0.5 V and the potential of collector electrode was kept constant at 0 V.

currents are unaffected by a change in flow rate in the microfluidic channel.

Finally, we studied the effect of flow rate combined with one of the most important parameter in geometric design: gap size. For this purpose, we defined a device with a wide gap of 170 nm (see figure 4.7B). The nanogap device clearly is sensitive to the variation of flow rate once the gap size is expanded to 170 nm. In this situation, the flow rate affects both the limiting current and the collection efficiency (the collection efficiency reduces from 0.85 to 0.76 by increasing the flow rate from 0 to 600 μls^{-1}). Here, the flow prevents inter-diffusion of species between the two electrodes.

4.4. CONCLUSION

We proposed a new design for generator-collector nanogap devices and performed finite element simulations to study electrochemical processes inside the sensor. We considered the effect of different geometric parameters as well as applied potentials for this design. Data revealed that decreasing the gap size and increasing the electrode thickness increase the amplification factor and collection efficiency of the device. However, varying the thickness of the top isolating layer results in insignificant changes in the device performance. We also showed that, once the nanogap is located in a microfluidic chan-

nel, for small gap sizes (<170 nm) a change in flow rate typical for microfluidic channels does not influence the electrochemical processes in the gap. This information can be utilized for the fabrication of these nanogap sensors and their use in electroanalytical applications.

These sensors will combine the advantages of ease of fabrication, intrinsic high signal amplification due to redox cycling and possible integration into lab-chip or point-of-care devices. The independence of flow rate enhances the reliability in such applications as a calibration method is not required. Moreover, the open design will allow the combination with different detection techniques such as optical microscopy.

The simulations and well-understood geometry will enable a straightforward detailed and quantitative assessment of future experimental data.

REFERENCES

[1] H. R. Zafarani, K. Mathwig, E. J. Sudhölter, and L. Rassaei, *Electrochemical redox cycling in a new nanogap sensor: Design and simulation,* Journal of Electroanalytical Chemistry **760**, 42 (2016).

[2] J. T. Cox and B. Zhang, *Nanoelectrodes: recent advances and new directions,* Annual review of analytical chemistry **5**, 253 (2012).

[3] K. Mathwig, T. Albrecht, E. D. Goluch, and L. Rassaei, *Challenges of biomolecular detection at the nanoscale: nanopores and microelectrodes,* Analytical chemistry **87**, 5470 (2015).

[4] H. Ben-Yoav, T. E. Winkler, E. Kim, S. E. Chocron, D. L. Kelly, G. F. Payne, and R. Ghodssi, *Redox cycling-based amplifying electrochemical sensor for in situ clozapine antipsychotic treatment monitoring,* Electrochimica Acta **130**, 497 (2014).

[5] K. Ino, Y. Kanno, T. Nishijo, H. Komaki, Y. Yamada, S. Yoshida, Y. Takahashi, H. Shiku, and T. Matsue, *Densified electrochemical sensors based on local redox cycling between vertically separated electrodes in substrate generation/chip collection and extended feedback modes,* Analytical chemistry **86**, 4016 (2014).

[6] A. Walter, J. Wu, G.-U. Flechsig, D. A. Haake, and J. Wang, *Redox cycling amplified electrochemical detection of dna hybridization: application to pathogen e. coli bacterial rna,* Analytica chimica acta **689**, 29 (2011).

[7] W. J. Albery and M. L. Hitchman, *Ring-disc electrodes* (Oxford University Press, 1971).

[8] W. Albery, M. Hitchman, and J. Ulstrup, *Ring-disc electrodes. part 9.—application to first-order kinetics,* Transactions of the Faraday Society **64**, 2831 (1968).

[9] C. Amatore, C. Sella, and L. Thouin, *Electrochemical time-of-flight responses at double-band generator-collector devices under pulsed conditions,* Journal of Electroanalytical Chemistry **593**, 194 (2006).

[10] P. Liljeroth, C. Johans, C. J. Slevin, B. M. Quinn, and K. Kontturi, *Micro ring–disk electrode probes for scanning electrochemical microscopy,* Electrochemistry communications **4**, 67 (2002).

[11] C. Thomas, P. Springer, G. Loeb, Y. Berwald-Netter, and L. Okun, *A miniature microelectrode array to monitor the bioelectric activity of cultured cells,* Experimental cell research **74**, 61 (1972).

[12] V. Dam, W. Olthuis, and A. Van den Berg, *Redox cycling with facing interdigitated array electrodes as a method for selective detection of redox species,* Analyst **132**, 365 (2007).

[13] I. J. Cutress, Y. Wang, J. G. Limon-Petersen, S. E. Dale, L. Rassaei, F. Marken, and R. G. Compton, *Dual-microdisk electrodes in transient generator–collector mode: Experiment and theory,* Journal of electroanalytical chemistry **655**, 147 (2011).

[14] L. Rassaei, R. W. French, R. G. Compton, and F. Marken, *Microwave-enhanced electroanalytical processes: generator–collector voltammetry at paired gold electrode junctions,* Analyst **134**, 887 (2009).

[15] E. O. Barnes, G. E. Lewis, S. E. Dale, F. Marken, and R. G. Compton, *Generator-collector double electrode systems: A review,* Analyst **137**, 1068 (2012).

[16] R. W. French, S. N. Gordeev, P. R. Raithby, and F. Marken, *Paired gold junction electrodes with submicrometer gap,* Journal of Electroanalytical Chemistry **632**, 206 (2009).

[17] D. Mampallil, K. Mathwig, S. Kang, and S. G. Lemay, *Redox couples with unequal diffusion coefficients: effect on redox cycling,* Analytical chemistry **85**, 6053 (2013).

[18] R. W. French, A. M. Collins, and F. Marken, *Growth and application of paired gold electrode junctions: evidence for nitrosonium phosphate during nitric oxide oxidation,* Electroanalysis **20**, 2403 (2008).

[19] D. Menshykau, M. Cortina-Puig, F. J. del Campo, F. X. Muñoz, and R. G. Compton, *Plane-recessed disk electrodes and their arrays in transient generator–collector mode: The measurement of the rate of the chemical reaction of electrochemically generated species,* Journal of Electroanalytical Chemistry **648**, 28 (2010).

[20] L. Rassaei, P. S. Singh, and S. G. Lemay, *Lithography-based nanoelectrochemistry,* (2011).

[21] S. E. Dale, A. Vuorema, M. Sillanpää, J. Weber, A. J. Wain, E. O. Barnes, R. G. Compton, and F. Marken, *Nano-litre proton/hydrogen titration in a dual-plate platinum-platinum generator-collector electrode micro-trench,* Electrochimica Acta **125**, 94 (2014).

[22] M. A. Hasnat, A. J. Gross, S. E. Dale, E. O. Barnes, R. G. Compton, and F. Marken, *A dual-plate ito–ito generator–collector microtrench sensor: surface activation, spatial separation and suppression of irreversible oxygen and ascorbate interference,* Analyst **139**, 569 (2014).

[23] A. J. Gross, S. Holmes, S. E. Dale, M. J. Smallwood, S. J. Green, C. P. Winlove, N. Benjamin, P. G. Winyard, and F. Marken, *Nitrite/nitrate detection in serum based on dual-plate generator–collector currents in a microtrench,* Talanta **131**, 228 (2015).

[24] M. A. Zevenbergen, B. L. Wolfrum, E. D. Goluch, P. S. Singh, and S. G. Lemay, *Fast electron-transfer kinetics probed in nanofluidic channels,* Journal of the American Chemical Society **131**, 11471 (2009).

[25] B. Wolfrum, M. Zevenbergen, and S. Lemay, *Nanofluidic redox cycling amplification for the selective detection of catechol,* Analytical chemistry **80**, 972 (2008).

[26] M. A. Zevenbergen, P. S. Singh, E. D. Goluch, B. L. Wolfrum, and S. G. Lemay, *Stochastic sensing of single molecules in a nanofluidic electrochemical device,* Nano letters **11**, 2881 (2011).

[27] K. Mathwig, T. J. Aartsma, G. W. Canters, and S. G. Lemay, *Nanoscale methods for single-molecule electrochemistry,* Annual Review of Analytical Chemistry **7**, 383 (2014).

[28] L. Rassaei, K. Mathwig, S. Kang, H. A. Heering, and S. G. Lemay, *Integrated biodetection in a nanofluidic device,* ACS nano **8**, 8278 (2014).

[29] E. D. Goluch, B. Wolfrum, P. S. Singh, M. A. Zevenbergen, and S. G. Lemay, *Redox cycling in nanofluidic channels using interdigitated electrodes,* Analytical and bioanalytical chemistry **394**, 447 (2009).

[30] C. Ma, N. M. Contento, L. R. Gibson, and P. W. Bohn, *Redox cycling in nanoscale-recessed ring-disk electrode arrays for enhanced electrochemical sensitivity,* Acs Nano **7**, 5483 (2013).

[31] S. K. Kim, P. J. Hesketh, C. Li, J. H. Thomas, H. B. Halsall, and W. R. Heineman, *Fabrication of comb interdigitated electrodes array (ida) for a microbead-based electrochemical assay system,* Biosensors and Bioelectronics **20**, 887 (2004).

[32] R. R. Kamath and M. J. Madou, *Three-dimensional carbon interdigitated electrode arrays for redox-amplification,* Analytical chemistry **86**, 2963 (2014).

[33] J. Heo, D. Shim, G. T. Teixidor, S. Oh, M. Madou, and H. Shin, *Carbon interdigitated array nanoelectrodes for electrochemical applications,* Journal of the Electrochemical Society **158**, J76 (2011).

[34] K. V. Singh, A. M. Whited, Y. Ragineni, T. W. Barrett, J. King, and R. Solanki, *3d nanogap interdigitated electrode array biosensors,* Analytical and bioanalytical chemistry **397**, 1493 (2010).

[35] A. J. Bard, L. R. Faulkner, *et al., Fundamentals and applications,* Electrochemical Methods **2** (2001).

[36] X. Yang and G. Zhang, *The voltammetric performance of interdigitated electrodes with different electron-transfer rate constants,* Sensors and Actuators B: Chemical **126**, 624 (2007).

[37] J. Min and A. J. Baeumner, *Characterization and optimization of interdigitated ultramicroelectrode arrays as electrochemical biosensor transducers,* Electroanalysis **16**, 724 (2004).

[38] L. B. Anderson and C. N. Reilley, *Thin-layer electrochemistry: steady-state methods of studying rate processes,* Journal of Electroanalytical Chemistry (1959) **10**, 295 (1965).

[39] M. Straver, M. Odijk, W. Olthuis, and A. van den Berg, *A simple method to fabricate electrochemical sensor systems with predictable high-redox cycling amplification,* Lab on a Chip **12**, 1548 (2012).

[40] L. Rassaei, K. Mathwig, E. D. Goluch, and S. G. Lemay, *Hydrodynamic voltammetry with nanogap electrodes,* The Journal of Physical Chemistry C **116**, 10913 (2012).

[41] H. Bruus, *Acoustofluidics 1: Governing equations in microfluidics,* Lab on a Chip **11**, 3742 (2011).

[42] K. Mathwig and S. G. Lemay, *Mass transport in electrochemical nanogap sensors,* Electrochimica Acta **112**, 943 (2013).

5

ELECTROCHEMICAL AMPLIFICATION IN SIDE-BY-SIDE ATTOLITER NANOGAP TRANSDUCERS

We report a strategy for the fabrication of a new type of electrochemical nanogap transducer. These nanogap devices are based on signal amplification by redox cycling. Using two steps of electron-beam lithography, vertical gold electrodes are fabricated side by side at a 70 nm distance encompassing a 20 attoliter open nanogap volume. We demonstrate a current amplification factor of 2.5 as well as the possibility to detect the signal of only 60 analyte molecules occupying the detection volume. Experimental voltammetry results are compared to calculations from finite element analysis.

This chapter is based on the following publication:

H.R. Zafarani, K. Mathwig, E.J.R. Sudhölter and L. Rassaei, ACS SENSORS **2017**, *2*, 724–728 [1].

5.1. INTRODUCTION

DEMANDS for robust analysis at the clinical point-of-care [2, 3] as well as for monitoring pollutants in the environment [4, 5] have led to diverse research directions toward the development and further size reduction of miniaturized analytical chemical sensors. Electrochemical detectors combine the advantages of being sensitive tools with a low cost, small sample volume, and fast response time [6–10]. Here, progress stems from the developments in microfabrication techniques and their application in analytical chemistry [11–15]. Microelectrodes in particular offer a superior performance [16–19] with enhanced mass transport to the electrode surface resulting in a fast response time and often low detection limits and high signal-to noise ratios.

The small surface areas of microelectrodes yield low currents, which are often difficult to detect with conventional electrochemical equipment [20, 21]. An effective way for signal amplification is redox cycling, *i.e.*, the successive oxidation and reduction of analyte molecules at two closely spaced electrodes. As analytes travel by diffusion between the electrodes, each molecule can shuttle up to thousands of times per second, leading to an intrinsic amplification of the current. In addition, in redox cycling only reversibly electrochemically active species yield an amplified signal and two separated working electrodes are employed, enabling biasing schemes for a highly selective sensing [22, 23], for example, by using interdigitated electrodes (IDEs) [17, 24, 25].

Microfabricated nanogap devices are a newer type of redox cycling devices which consist of two planar parallel electrodes closely spaced (≤100 nm) in a nanochannel, positioned as its bottom and ceiling in a thin-layer cell configuration [26]; or they can be realized as pore-based structures in which electrodes are stacked in vertical pores consisting of metal-insulator-metal layers [27, 28]. Due to this small distance these devices can be employed for a variety of sensing schemes such as mesoscopic stochastic sensing, advanced biodetection, and single-molecule electrochemistry [29–33]. The fabrication of these devices requires several steps of consecutive electron-beam or photolithography, depositions, and dry etching, making the overall process rather complex.

Here, we report a novel nanogap transducer which we had previously investigated by numerical methods [34]. The geometry consists of two electrodes positioned side by side at a 70 nm distance. The electrode pair is not covered to form a closed nanochannel, but the active detection volume is directed to a larger reservoir. The active volume is 20 attoliters, about 100 times less than previously reported for closed nanogap devices [29]. Our device resembles an interdigitated electrode array [17, 35, 36] with several unique properties: it only has two fingers; the nanoscale interelectrode distance is considerably smaller than in most IDEs [37–39]; the electrode surfaces are parallel [40] and are passivated on top. We characterized the device by cyclic voltammetry and step amperometry to determine the amplification factor, sensitivity, and time response, and compared the experimental performance by two-dimensional finite element analysis.

5.2. EXPERIMENTAL SECTION

Device Fabrication: Two steps of electron-beam lithography were employed to pattern devices on a silicon wafer substrate passivated by 300 nm thermally grown silicon oxide. Figure 5.1A shows the fabrication scheme. First, two layers of methyl methacrylate

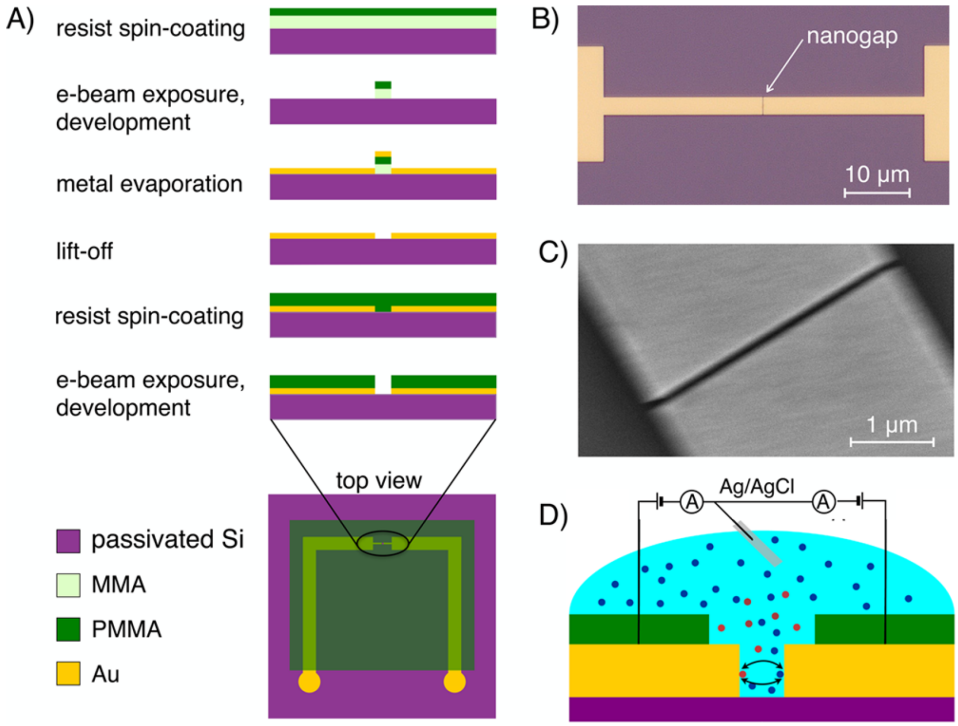

Figure 5.1: (A) Schematic of the nanogap fabrication process. (B) Microscopic top view image of a typical nanogap device. (C) Electron micrograph of the Au-PMMA nanogap. (D) Schematic principle of electrochemical measurements.

(MMA) and poly(methyl methacrylate) (PMMA) (thicknesses of 300 and 150 nm) were successively spin-coated on the substrate. Two 3-μm wide electrodes with a 70 nm gap in between were patterned by e-beam exposure. Next, a 10-nm-thick Ti adhesion layer and 80-nm thick Au were deposited by electron-beam evaporation, followed by a lift-off (hence, active volume = 3 μm × 70 nm × 80 nm ≃ 20 attoliters). Subsequently, a 500-nm-thick PMMA passivation layer was spin-coated. In a second e-beam exposure and development step, only the gap area and connection pads were exposed. Microscopic top-view images of a nanogap (Au and passivation layer) are shown in figure 5.1B and C.

Chemicals: 1,1'-Ferrocene dimethanol, $Fc(MeOH)_2$, and potassium chloride, KCl, were obtained from Sigma-Aldrich. All solutions were freshly prepared in Milli-Q water with 1 M KCl as supporting electrolyte. The experiments were carried out at room temperature.

Electrochemical Experiments: A Keithley 4200 parameter analyzer with two source measurement units was used to separately bias both electrodes as well as to measure Faradaic currents. A Ag/AgCl reference electrode (BASi Inc.) was positioned in a reservoir

on top of the nanogap device. Figure 5.1D shows the measurement setup.

5.3. RESULTS AND DISCUSSION

Fabrication of the Nanogap: Focused ion beam milling has been employed for the fabrication of the nanogaps for single molecule measurements in the field of molecular electronics [41–43], and it has the advantage of fabrication in a single milling step. However, we found that this technique is not optimally suited for our nanogaps: due to the Gaussian distribution of the ion beam, v-shaped nanogap structures were obtained instead of parallel straight walls [41, 44, 45]. Moreover, by employing ion beam milling, not only the metal but also the passivation layer around the gap are removed (with a Gaussian geometry); hence surrounding the gap a large area of the electrodes remains bare without any passivation on top.

Using e-beam lithography and lift-off, well-defined clean sidewalls of two closely spaced electrodes are more easily achievable. While we chose a gap width of 70 nm, also considerably shorter interelectrode distances are feasible (possibly at reduced metal thicknesses). Moreover, using this fabrication by deposition, lithography, and lift-off, electrodes can be fabrication in a large variety of materials. A second e-beam exposure defined the insulating layer; to avoid covering the nanogap with PMMA due to misalignment, a wider opening was chosen (50 nm tolerance). While this layer does not allow the use of organic solvent in electrochemical measurements, it can be replaced by inert materials such as silicon oxide.

Current Amplification: We compared the current of the nanogap transducers in single mode (*i.e.*, biasing only one electrode) and in redox cycling dual mode to determine the amplification factor. Figure 5.2 presents cyclic voltammograms for a device filled with 0.5 mM $Fc(MeOH)_2$ in a 1 M KCl aqueous solution. In single mode (see figure 5.2A,B), the potential of one electrode was swept while the other one was kept floating. In dual mode (see figure 5.2C), one electrode was swept (right generator electrode) from 0 to 0.5 V while the left collector electrode was kept at a constant reducing potential of 0 V vs Ag/AgCl. Comparing the limiting currents in single mode, I_{single}, and dual mode, I_{dual}, leads to an amplification factor of $I_{dual}/I_{single} = 2.5$. The difference between the limiting currents of the right and left electrodes (100 pA vs 75 pA at 0.5 V) in figure 5.2C stems from the open geometry of the nanogap; oxidized and reduced species produced at one electrode can diffuse back into the solution before reaching the next electrode. Thus, amplification factor and collection efficiency are reduced, and a collection efficiency of $I_{collector}/I_{generator} = 75\%$ was obtained.

The Faradaic limiting current for two planar opposing electrodes is determined as [23]

$$I = \frac{nFADC}{z} \tag{5.1}$$

where n is the number of exchanged electrons, F the Faraday constant, A the electrode surface area, D the diffusion coefficient, C the analyte concentration, and z the interelectrode distance. Using equation 5.1 yields a current of $I = 110$ pA in good agreement with the experimental value of 100 pA. The effective redox cycling volume in between the two electrodes amounts to 20 aL, which is about 100 times smaller than in smallest electrochemical nanochannel sensors [29, 46, 47].

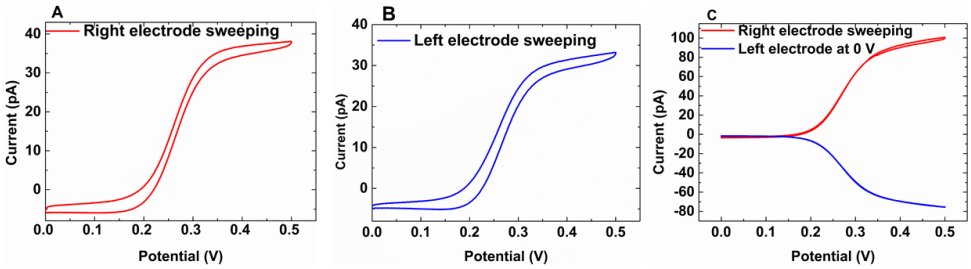

Figure 5.2: Cyclic voltammograms of 0.5 mM $Fc(MeOH)_2$ in 1 M KCl solution in the nanogap at a 5 mVs^{-1} scan rate. (A) The right electrode was swept between 0 to 0.5 V (*vs.* Ag/AgCl) while the left electrode was disconnected. (B) The left electrode was swept between 0 and 0.5 V while the right electrode was disconnected. (C) The right electrode was swept between 0 and 0.5 V while the left electrode was kept constant at 0 V.

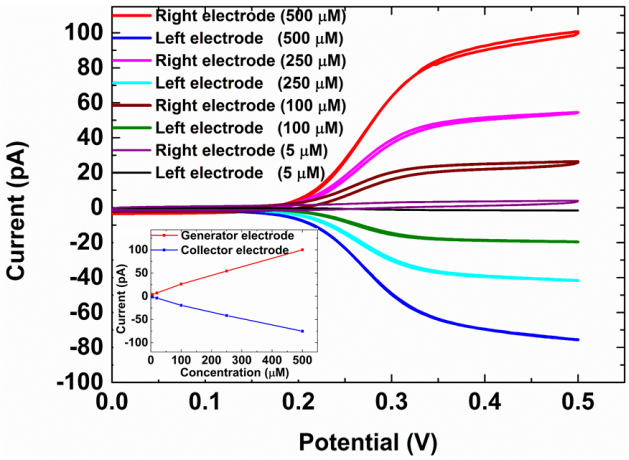

Figure 5.3: Cyclic voltammograms of different concentrations of $Fc(MeOH)_2$ in 1 M KCl solution at a 5 mVs^{-1} scan rate. Inset: Limiting current at 0.5 V as a function of concentration: 5, 10, 100, 250, and 500 μM (lines are guides for the eye).

Concentration Effect: Detection limit. In order to quantitatively investigate the detection limit of the nanogap transducers, we performed cyclic voltammetry for different concentrations of $Fc(MeOH)_2$ in 1 M KCl solution as presented in figure 5.3. The right electrode potential was swept between 0 and 0.5 V (at a 5 mVs^{-1} scan rate) while the left electrode was fixed at 0 V. Well-defined cyclic voltammograms were obtained for $Fc(MeOH)_2$ concentrations down to 5 μM, showing in linear response in the limiting current (see inset in figure 5.3). For the concentration of 5 μM, corresponding to an average number of 60 molecules in the active volume, a limiting current of 1.5 pA was measured at the collector electrode (Lower concentrations were inaccessible due to an instrumental limitation of 1 pA).

Response Time: The response time is an important characteristic of nanogap sensors [48]; it is the time to reach a steady-state current after a change in concentration (or a change in local concentration induced by stepping an electrode potential). In closed

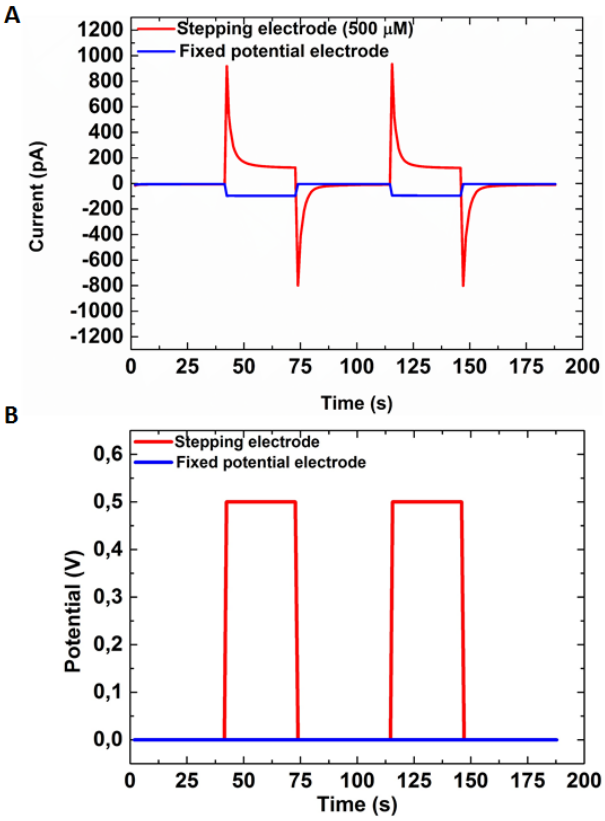

Figure 5.4: (A)Step chronoamperometry for 0.5 mM $Fc(MeOH)_2$ in 1 M KCl solution. The left electrode (blue) is kept at a constant potential of 0 V; the right electrode (red) is stepped to either 0 or 0.5 V. (B) Applied potentials as a function of time.

nanochannels, molecules have to diffuse from the bulk and through the access holes along the entire nanochannel (length L) to reach an equilibrium concentration. The response time $\tau \propto L^2/D$ is further slowed down by reversible potential-dependent adsorption of analytes and can amount to several tens of seconds [48, 49].

We investigated the response time of the side-by-side devices by stepping the potential of one of the electrodes between 0 and 0.5 V and observing the current response at the other electrode biased constantly at 0 V (see figure 5.4). While the stepping electrode exhibits considerable transient behavior due to parasitic RC charging [48], the collector electrode shows an instant response, limited by the instrumental time resolution of 0.2 s. We estimate that the actual response time of the device is much shorter, as it only takes $\propto (80\ nm)^2/D = 10\ \mu$s to diffuse into its active area. Also, moderately fast sweeping in cyclic voltammetry without hysteresis is facilitated due to this fast response (see Supporting Information for scan rates ranging from 1 to 40 mVs^{-1}).

Numerical Analysis: We employed two-dimensional finite element analysis (COM-

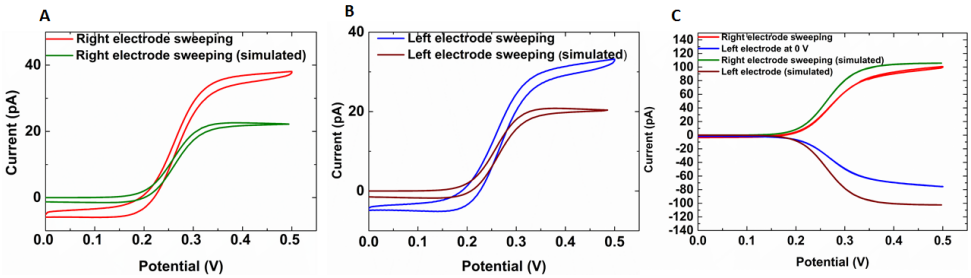

Figure 5.5: Comparison of simulated and experimental cyclic voltammograms obtained for 0.5 mM $Fc(MeOH)_2$ in 1 M KCl solution at a 5 mVs^{-1} scan rate for (A,B) single mode and (C) redox cycling.

SOL Multiphysics 4.4; see Supporting Information) to model the electrochemical reactions in the nanogap, following up our previous, more detailed numerical investigation of the effect of several geometric parameters on redox cycling in the side-by-side nanogap geometry [34]. Numerically and experimentally obtained cyclic voltammograms for 0.5 mM $Fc(MeOH)_2$ in 1 M KCl at 5 mVs^{-1} are compared in figure 5.5 (a 50 nm tolerance of PMMA layer is considered in the simulation as well). There is good agreement with the experimental voltammograms; being slightly skewed towards higher potentials in redox cycling, presumably due to slower electron transfer kinetics, and exhibiting lower limiting currents. In redox cycling, the current is 5% lower for the generator electrode and 26% lower for the collector electrode with respect to the numerical values (at 0.5 V; see figure 5.5C). We attribute these differences to deviations of the device geometry (electrode height and distance, alignment of passivation layer) from nominal values, as well as by the fact that generated molecules can escape the nanogap at both ends, which is not captured by the 2D simulation. For the same reason, in single mode the 2D simulation yields lower current values (see figures 5.5A,B), leading to a high numerical amplification factor of 5. Compared to our previous simulation [34] (amplification factor of 8) this amplification factor is lower because we take the wider opening of the passivation layer into account.

5.4. CONCLUSION

We developed a new electrochemical nanogap transducer geometry by placing two electrodes side by side at a 70 nm distance. Fabrication comprises only two lithography steps and makes it possible to fabricate a wide range of gap sizes and make use of different electrode materials, *i.e.*, any material that can be sputtered or deposited.

While our open geometry enables a very fast response time compared to covered nanogaps, this comes at the cost of a reduced amplification factor and a short residence time of individual molecules between the electrodes. Thus, it is currently not possible to perform single-molecule detection or mesoscopic sensing as is possible in covered nanochannel sensors.

We are convinced that – next to the shown advantages of ease of fabrication and the possible variation of electrode materials – our devices will realize their full potential in future planned experiments for three reasons: First, the nanogap can be covered (*e.g.*,

with a glass coverslip) enclosing a 20-100 aL nanochannel volume (depending of the channel length), which is at least 1 order of magnitude smaller than previously reported nanogap channels [31]. Such small volumes make single molecule detection come into reach. Second, the side-by-side arrangement allows direct access of optical detection methods either from the top or through a transparent substrate using an inverted microscope, thus enabling direct observation of combined optical-electrochemical molecular properties [50]. Third, e-beam lithography allows a further considerable reduction of the interelectrode distance, increasing its sensitivity and further reducing the active volume. Therefore, we anticipate that the side-by-side nanogap transducers will form a versatile nanoscale electroanalytical tool.

REFERENCES

[1] H. R. Zafarani, K. Mathwig, E. J. Sudholter, and L. Rassaei, *Electrochemical amplification in side-by-side attoliter nanogap transducers,* ACS Sensors **2**, 724 (2017).

[2] A. F. D. Cruz, N. Norena, A. Kaushik, and S. Bhansali, *A low-cost miniaturized potentiostat for point-of-care diagnosis,* Biosensors and Bioelectronics **62**, 249 (2014).

[3] K. Mathwig, T. Albrecht, E. D. Goluch, and L. Rassaei, *Challenges of biomolecular detection at the nanoscale: nanopores and microelectrodes,* Analytical chemistry **87**, 5470 (2015).

[4] D. Omanović, C. Garnier, K. Gibbon-Walsh, and I. Pižeta, *Electroanalysis in environmental monitoring: Tracking trace metals—a mini review,* Electrochemistry Communications **61**, 78 (2015).

[5] N. Wang, E. Kanhere, J. Miao, and M. S. Triantafyllou, *Miniaturized chemical sensor with bio-inspired micropillar working electrode array for lead detection,* Sensors and Actuators B: Chemical **233**, 249 (2016).

[6] H. Ben-Yoav, P. H. Dykstra, W. E. Bentley, and R. Ghodssi, *A microfluidic-based electrochemical biochip for label-free diffusion-restricted dna hybridization analysis,* Biosensors and Bioelectronics **38**, 114 (2012).

[7] A. P. Demchenko, *The sensing devices,* in *Introduction to Fluorescence Sensing* (Springer, 2015) pp. 507–550.

[8] Á. Ríos, M. Zougagh, and M. Avila, *Miniaturization through lab-on-a-chip: Utopia or reality for routine laboratories? a review,* Analytica Chimica Acta **740**, 1 (2012).

[9] F. Chang, X. Xie, M. Li, and Z. Zhu, *A miniaturized electrochemical device integrating a biconical microchannel and carbon fiber disk ultramicroelectrode,* Analyst **141**, 4859 (2016).

[10] X. Zhu and C. H. Ahn, *On-chip electrochemical analysis system using nanoelectrodes and bioelectronic cmos chip,* IEEE sensors journal **6**, 1280 (2006).

[11] J. Wang, *Electrochemical detection for microscale analytical systems: a review,* Talanta **56**, 223 (2002).

[12] S. M. Oja, M. Wood, and B. Zhang, *Nanoscale electrochemistry,* Anal. Chem **85**, 473 (2013).

[13] Y. Kanno, K. Ino, H. Shiku, and T. Matsue, *A local redox cycling-based electrochemical chip device with nanocavities for multi-electrochemical evaluation of embryoid bodies,* Lab on a Chip **15**, 4404 (2015).

[14] D. G. Rackus, M. H. Shamsi, and A. R. Wheeler, *Electrochemistry, biosensors and microfluidics: a convergence of fields,* Chemical Society Reviews **44**, 5320 (2015).

[15] K. Mathwig, Q. Chi, S. G. Lemay, and L. Rassaei, *Handling and sensing of single enzyme molecules: from fluorescence detection towards nanoscale electrical measurements,* ChemPhysChem **17**, 452 (2016).

[16] M. Montenegro, A. Queiros, and J. Daschbach, *Microelectrodes—principles and applications,* NATO ASI Series, Riedel, Dordrecht (1990).

[17] N. Alayo, C. Fernández-Sánchez, A. Baldi, J. P. Esquivel, X. Borrisé, and F. Pérez-Murano, *Gold interdigitated nanoelectrodes as a sensitive analytical tool for selective detection of electroactive species via redox cycling,* Microchimica Acta **183**, 1633 (2016).

[18] N. J. Ronkainen, *Micro-and nanoelectrodes in protein-based electrochemical biosensors for nanomedicine and other applications,* Advanced Bioelectronics Materials , 1 (2015).

[19] A. J. Gross and F. Marken, *Ito-ito dual-plate microgap electrodes: E and ec generator-collector processes,* Electroanalysis **27**, 1035 (2015).

[20] M. Y. Vagin, A. N. Sekretaryova, R. S. Reategui, I. Lundstrom, F. Winquist, and M. Eriksson, *Arrays of screen-printed graphite microband electrodes as a versatile electroanalysis platform,* ChemElectroChem **1**, 755 (2014).

[21] R. G. Compton, G. G. Wildgoose, N. V. Rees, I. Streeter, and R. Baron, *Design, fabrication, characterisation and application of nanoelectrode arrays,* Chemical Physics Letters **459**, 1 (2008).

[22] H. R. Zafarani, K. Mathwig, S. G. Lemay, E. J. Sudholter, and L. Rassaei, *Modulating selectivity in nanogap sensors,* ACS Sensors **1**, 1439 (2016).

[23] E. D. Goluch, B. Wolfrum, P. S. Singh, M. A. Zevenbergen, and S. G. Lemay, *Redox cycling in nanofluidic channels using interdigitated electrodes,* Analytical and bioanalytical chemistry **394**, 447 (2009).

[24] M. Morita, K. Hayashi, T. Horiuchi, S. Shibano, K. Yamamoto, and K. J. Aoki, *Enhancement of redox cycling currents at interdigitated electrodes with elevated fingers,* Journal of The Electrochemical Society **161**, H178 (2014).

[25] K. Ueno, M. Hayashida, J.-Y. Ye, and H. Misawa, *Fabrication and electrochemical characterization of interdigitated nanoelectrode arrays,* Electrochemistry communications **7**, 161 (2005).

[26] M. A. Zevenbergen, D. Krapf, M. R. Zuiddam, and S. G. Lemay, *Mesoscopic concentration fluctuations in a fluidic nanocavity detected by redox cycling,* Nano letters **7**, 384 (2007).

[27] K. Fu, D. Han, C. Ma, and P. W. Bohn, *Electrochemistry at single molecule occupancy in nanopore-confined recessed ring-disk electrode arrays,* Faraday discussions **193**, 51 (2016).

[28] D. Han, L. P. Zaino III, K. Fu, and P. W. Bohn, *Redox cycling in nanopore-confined recessed dual-ring electrode arrays,* The Journal of Physical Chemistry C **120**, 20634 (2016).

[29] L. Rassaei, K. Mathwig, S. Kang, H. A. Heering, and S. G. Lemay, *Integrated biodetection in a nanofluidic device,* ACS nano **8**, 8278 (2014).

[30] P. S. Singh and S. G. Lemay, *Stochastic processes in electrochemistry,* Anal. Chem **88**, 5017 (2016).

[31] S. Kang, A. F. Nieuwenhuis, K. Mathwig, D. Mampallil, Z. A. Kostiuchenko, and S. G. Lemay, *Single-molecule electrochemistry in nanochannels: probing the time of first passage,* Faraday discussions **193**, 41 (2016).

[32] K. Mathwig, H. R. Zafarani, J. M. Speck, S. Sarkar, H. Lang, S. G. Lemay, L. Rassaei, and O. G. Schmidt, *Potential-dependent stochastic amperometry of multiferrocenylthiophenes in an electrochemical nanogap transducer,* The Journal of Physical Chemistry C **120**, 23262 (2016).

[33] K. Mathwig and S. G. Lemay, *Pushing the limits of electrical detection of ultralow flows in nanofluidic channels,* Micromachines **4**, 138 (2013).

[34] H. R. Zafarani, K. Mathwig, E. J. Sudhölter, and L. Rassaei, *Electrochemical redox cycling in a new nanogap sensor: Design and simulation,* Journal of Electroanalytical Chemistry **760**, 42 (2016).

[35] N. Azizah, U. Hashim, S. C. Gopinath, and S. Nadzirah, *Gold nanoparticle mediated method for spatially resolved deposition of dna on nano-gapped interdigitated electrodes, and its application to the detection of the human papillomavirus,* Microchimica Acta **183**, 3119 (2016).

[36] X. Zhu and C. H. Ahn, *Electrochemical determination of reversible redox species at interdigitated array micro/nanoelectrodes using charge injection method,* IEEE transactions on nanobioscience **4**, 164 (2005).

[37] J. S. Shim, M. J. Rust, and C. H. Ahn, *A large area nano-gap interdigitated electrode array on a polymer substrate as a disposable nano-biosensor,* Journal of Micromechanics and Microengineering **23**, 035002 (2013).

[38] K. Hayashi, J.-i. Takahashi, T. Horiuchi, Y. Iwasaki, and T. Haga, *Development of nanoscale interdigitated array electrode as electrochemical sensor platform for highly sensitive detection of biomolecules,* Journal of The Electrochemical Society **155**, J240 (2008).

[39] L. Skjolding, C. Spegel, A. Ribayrol, J. Emnéus, and L. Montelius, *Characterisation of nano-interdigitated electrodes,* in *Journal of Physics: Conference Series*, Vol. 100 (IOP Publishing, 2008) p. 052045.

[40] R. R. Kamath and M. J. Madou, *Three-dimensional carbon interdigitated electrode arrays for redox-amplification,* Analytical chemistry **86**, 2963 (2014).

[41] T. Nagase, *Handbook of manufacturing engineering and technology* (Springer London: Imprint: Springer, 2015) pp. 1513–1528.

[42] T. Nagase, T. Kubota, and S. Mashiko, *Fabrication of nano-gap electrodes for measuring electrical properties of organic molecules using a focused ion beam,* Thin Solid Films **438**, 374 (2003).

[43] G. Purohit, M. Shankar, D. Gupta, S. Damodaran, and M. Katiyar, *Fabrication of nano-gap electrodes using a focused ion beam for measuring electrical properties of molecular scale transistors,* in *16th International Workshop on Physics of Semiconductor Devices*, Vol. 8549 (International Society for Optics and Photonics, 2012) p. 85492J.

[44] R. Young, J. Cleaver, and H. Ahmed, *Characteristics of gas-assisted focused ion beam etching,* Journal of Vacuum Science & Technology B: Microelectronics and Nanometer Structures Processing, Measurement, and Phenomena **11**, 234 (1993).

[45] A. A. Tseng, *Recent developments in micromilling using focused ion beam technology,* Journal of Micromechanics and Microengineering **14**, R15 (2004).

[46] M. A. Zevenbergen, B. L. Wolfrum, E. D. Goluch, P. S. Singh, and S. G. Lemay, *Fast electron-transfer kinetics probed in nanofluidic channels,* Journal of the American Chemical Society **131**, 11471 (2009).

[47] L. Rassaei, K. Mathwig, E. D. Goluch, and S. G. Lemay, *Hydrodynamic voltammetry with nanogap electrodes,* The Journal of Physical Chemistry C **116**, 10913 (2012).

[48] S. Kang, K. Mathwig, and S. G. Lemay, *Response time of nanofluidic electrochemical sensors,* Lab on a Chip **12**, 1262 (2012).

[49] D. Mampallil, K. Mathwig, S. Kang, and S. G. Lemay, *Reversible adsorption of outer-sphere redox molecules at pt electrodes,* The journal of physical chemistry letters **5**, 636 (2014).

[50] H. Al-Kutubi, H. R. Zafarani, L. Rassaei, and K. Mathwig, *Electrofluorochromic systems: molecules and materials exhibiting redox-switchable fluorescence,* European Polymer Journal **83**, 478 (2016).

[51] A. J. Bard, L. R. Faulkner, *et al., Fundamentals and applications,* Electrochemical Methods **2** (2001).

[52] C. Ma, N. M. Contento, L. R. Gibson, and P. W. Bohn, *Redox cycling in nanoscale-recessed ring-disk electrode arrays for enhanced electrochemical sensitivity,* Acs Nano **7**, 5483 (2013).

5.5. SUPPORTING INFORMATION

Here, we present the effect of the scan rate on the limiting current response of the nanogap device and the details of our numerical finite element analysis.

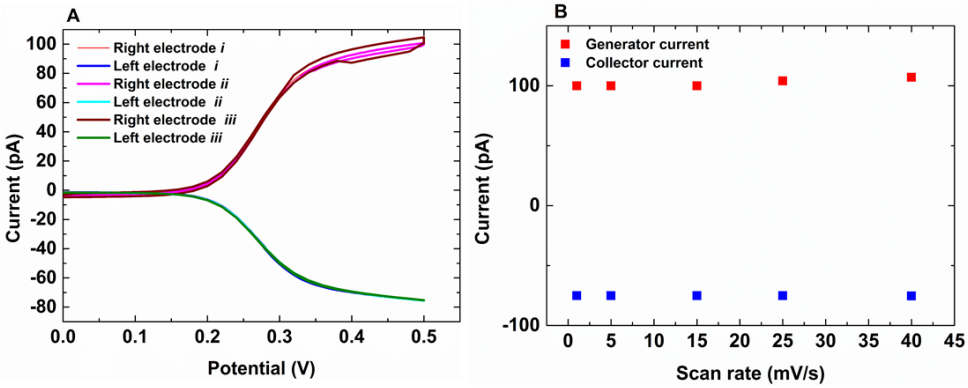

Figure S1: (A) Cyclic voltammograms of 0.5 mM $Fc(MeOH)_2$ in 1 M KCl solution at different scan rates: i) 1 mVs^{-1}, ii) 5 mVs^{-1}, iii) 25 mVs^{-1}. The right electrode was swept from 0 to 0.5 V *vs.* Ag/AgCl while the left electrode was kept constant at 0 V. (B) Limiting currents of the generator and collector electrodes at a potential of 0.5 V of the right generator electrode as a function of the can rate.

5

Effect of the scan rate: We studied the effect of the scan rate on the limiting currents in the nanogap device - ranging from 1 mVs^{-1} to 40 mVs^{-1}. Figure S1 shows cyclic voltammograms obtained for redox cycling of 0.5 mM $Fc(MeOH)_2$ at different scan rates. As expected, all steady state currents obtained in the nanogap sensor are completely identical for scan rates up to 25 mVs^{-1}. For scan rates of 25 mVs^{-1} and higher, a very small deviation from the steady state current is observed at the right electrode (sweeping electrode) due to the contribution of a capacitive current. For the left electrode with a fixed potential, the limiting current is not affected by the change in scan rate at all. Figure S1B presents the magnitude of limiting currents at 0.5 V for both collector and generator electrodes at different scan rates. The currents of both electrodes remain unchanged and are independent for all scan rates.

Numerical Methods: The electrochemical reactions in the nanogap devices were modelled using two-dimensional finite element analysis (COMSOL Multiphysics 4.4) as reported earlier [34]. In brief, in an unstirred solution containing a highly concentrated supporting electrolyte, diffusion was considered as the only mass transport mechanism in the nanogap sensor as described by Fick's second law:

$$\frac{\partial C_j}{\partial t} = D_j \nabla^2 C_\mathrm{j} \tag{5.2}$$

where C_j and D_j are the concentrations and diffusion coefficients of redox species j, respectively. The Faradaic currents at both electrodes were defined based on Butler-Volmer kinetics [51]

$$i = F[c_\mathrm{O} k_f - c_\mathrm{R} k_b] \tag{5.3}$$

$$k_f = k_0 e^{[\frac{-\alpha F(E-E_h)}{RT}]} \tag{5.4}$$

$$k_b = k_0 e^{[\frac{(1-\alpha) F(E-E_h)}{RT}]} \tag{5.5}$$

Table S1. Constants used in the simulation processes [46, 52].

D_O	$6.7 \times 10^{-10} m^2/s$	α	0.49
D_R	$6.7 \times 10^{-10} m^2/s$	F	96485.34 C/mol
k_o	0.06 m/s	R	8.31 J/K
E_h	0.26 V *vs.* Ag/AgCl	T	298 K

where i is the current, k_0 is the standard electrochemical rate constant, α the charge transfer coefficient, F the Faraday constant, E the electrode potential, E_h the standard potential of the redox couple, k_f and k_b are the forward (reduction) and backward (oxidation) rate constants of a redox reaction, R is the gas constant, and T is the temperature. The constants used in the simulation are listed in Table S1.

6

GENERATOR–COLLECTOR ELECTROCHEMICAL SENSOR CONFIGURATIONS BASED ON TRACK-ETCH MEMBRANE SEPARATED PLATINUM LEAVES

We report a novel, simple and cheap generator-collector electrode system, employing platinum leaves, with micron-sized pores and typically 100-300 nm thickness, sandwiched with a porous track etch membrane spacer with typically 30 nm diameter pores. The electrode assembly is sealed into a polymer lamination pouch with one side 2 mm diameter exposed to electrolyte solution. The generator electrode with sweeping potential (top or bottom electrode) shows transient current with high capacitive current component. The collector electrode with fixed potential shows well-defined steady state current response at low potential sweep rates. The fabricated device shows good performance in monitoring both 1,1'-ferrocene dimethanol oxidation and proton reduction redox processes. Oxygen sensor signals are assigned to a lowering of the steady state proton reduction current.

This chapter is based on the following publication:

H.R. Zafarani, L. Rassaei, E.J.R. Sudhölter, B.D.B. Aaronson and Frank Marken, Sensors and Actuators B **2018**, *255*, 2904–2909 [1].

6.1. INTRODUCTION

GENERATOR–COLLECTOR systems contain two working electrodes and provide powerful tools in electroanalytical studies [2]. Over the years these systems have been developed and studied in different geometries such as rotating ring-disk electrode [3], interdigitated electrodes [4, 5], thin-layer cells [6, 7] and nanoscale-recessed ring-disk electrodes [8]. Biasing proper potentials of these two closely spaced electrodes, allows repetitive oxidation and reduction of redox species between them and this leads to a strong amplification effects in sensing (known as redox cycling). This property then causes Faradaic current amplification to enhance the detection limit for analytical detection, also provides features such as suppressing irreversible interferences and enhancing the selectivity for reversible redox couples in electrochemical measurements [9, 10]. Furthermore, by fixing the potential on the "monitor" electrode and scanning the potential only for the second electrode, voltammograms can be recorded free of capacitive currents with improved analytical detection of the Faradaic current.

One of the key and challenging features of these devices is the gap between the electrodes. Reducing the gap size to the nanometer range can enhanced the sensitivity toward single molecule detection [11, 12]. However, in most cases fabrication of such a nanogap device needs access to the cleanroom facilities and requires following multiple sophisticated nanofabrication steps [11, 13–15].

Hence, in recent years there is a great interest for developing simple low cost methods to fabricate the micro/nano junctions between two electrodes that work under redox cycling conditions. Wang *et al.* fabricated a generator-collector system by growing a silicon nanochannel membrane on electrodes to fabricate a nanogap [16], Park *et al.* employed spherical beads as spacer between the electrodes [17] and Adly *et al.* fabricated nanoporous redox cycling devices employing multilayer inkjet printing [18]. However in these methods several steps of substrate treating or preparing the inks and access to inkjet printing facilities are needed. Previously, we developed simple low cost methods to develop the micro-junctions between two electrodes that work under redox cycling conditions. Electro-deposition and employing an epoxy spacer layer can be a feasible way for creating dual electrodes with analytical applications [19–23]. Often, the dual electrode configuration was based on a "microtrench" with one side open to the electrolyte solution.

In this work we introduce a novel generator-collector electrode system using track-etch membrane and "platinum leaf" electrodes. Porous platinum leaf electrodes are employed and the two electrodes are mounted with one of the platinum leaves facing "outward" into the solution phase (figure 6.1). Using a porous track-etch membrane layer between the two platinum leaf electrodes helps to prevent short-circuits while providing the diffusion path for the redox species in the redox cycling process.

It is shown that the two electrodes can be employed in generator-collector mode, although significant differences are observed when using (A) the outward facing electrode as the scanning electrode or (B) the inward facing electrode as the scanningelectrode. Processes based on the 1,1'-ferrocene dimethanol redox systems are demonstrated. Next, the reduction of protons is investigated and it is shown that oxygen concentration in solution is detected indirectly by lowering the local proton concentration within the dual-electrode generator–collector sensor. A wider range of applications is

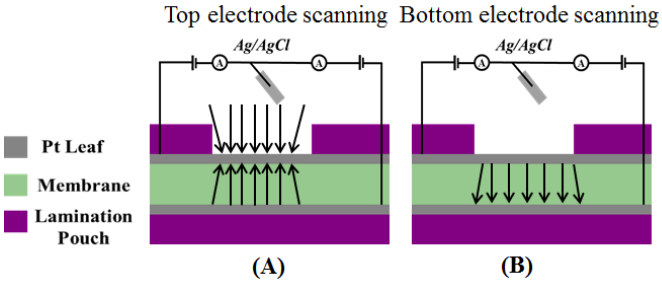

Figure 6.1: Schematic drawing of a dual-platinum leaf sensor with (A) the outward facing electrode scanning and (B) the inward facing electrode scanning. Arrows are shown to indicate diffusional transport towards the "actively scanning" electrode.

envisaged.

6.2. EXPERIMENTAL SECTION

Chemical reagents: 1,1'-ferrocene dimethanol, $Fc(MeOH)_2$, potassium nitrate, KNO_3 and nitric acid, HNO_3 were purchased from Sigma-Aldrich. Genuine platinum leaves (Wrights of Lymm Ltd) were purchased. Scanning electron micrographs indicate approximately 100-300 nm thick platinum (*vide infra*) with 1-10 μm diameter holes. Osmonics Inc. (Catalog No.KN3CP02500) polycarbonate track etch membrane with 30 nanometer diameter pore size was employed. Goodfellow Cambridge Ltd graphitic carbon foil was used to assemble the device (see figure 6.2).

Instrumentation Electrochemical: experiments were carried out using an Auto-lab PGSTAT302N bipotentiostat system. A commercial Ag/AgCl (3 M KCl) reference electrode (BASi Inc.) and a platinum counter electrode were used in electrochemical measurements. Generator-collector voltammetry was performed with one electrode potential fixed and one electrode potential scanning. Scanning electron microscopy images (SEM) were obtained using FEI NovaNano SEM.

Device fabrication: Porous platinum leaves were cut into two small pieces(10 mm × 30 mm) and a track etch membrane was placed as a separating layer between two platinum leaves. Strips of carbon foil were connected to each platinum piece as connection conductors to the top (T) and the bottom (B) electrode. Then the structure was laminated into a lamination pouch with a 2 mm diameter hole on top of the Pt/membrane/Pt sandwich exposing one of the electrodes to the electrolyte solution (figure 6.2).

6.3. RESULTS AND DISCUSSION

6.3.1. GENERATOR-COLLECTOR VOLTAMMETRY I.: CALIBRATION WITH 1,1'-FERROCENE DIMETHANOL

Initially voltammetric experiments were performed with 1,1'-ferrocene dimethanol, $Fc(MeOH)_2$, as a model redox system, in an aqueous 0.1 M KNO_3 solution to characterize

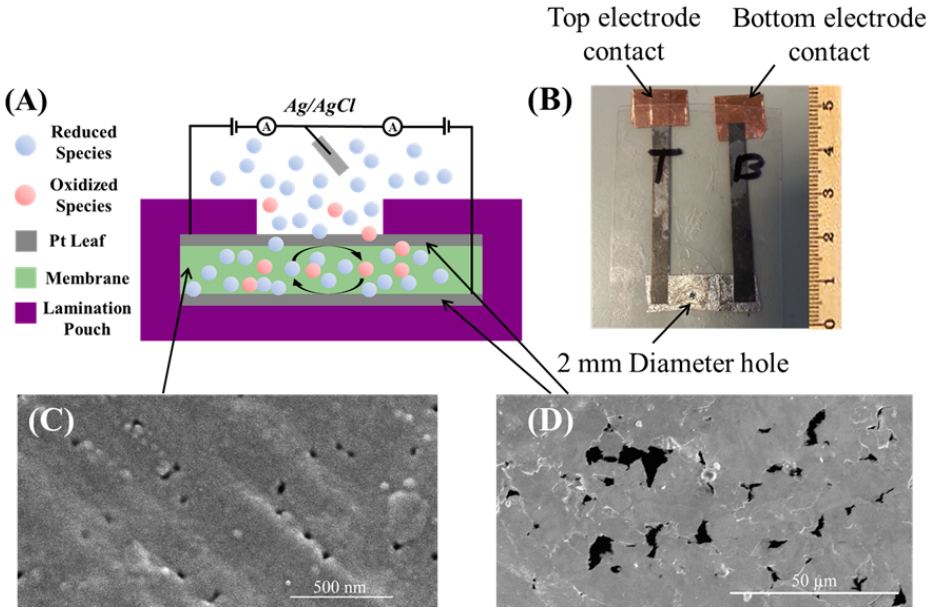

Figure 6.2: (A) Scheme of the device. (B) Fabricated device. (C) SEM image of the track etch membrane. (D) SEM image of the platinum leaf.

the generator-collector device (equation 6.1).

$$Fc(MeOH)_2 \rightleftarrows Fc(MeOH)_2^+ + e^- \tag{6.1}$$

Figure 6.3 shows a cyclic voltammogram for the oxidation of 0.25 mM 1,1'-ferrocene dimethanol , $Fc(MeOH)_2$, in solution. Oxidation of 1,1'-ferrocene dimethanol at the top electrode is clearly observed (figure 6.3A). The top electrode is scanning and the bottom electrode is disconnected. In this case the voltammetric response is almost identical with that observed when a fixed potential (0.0 V *vs.* Ag/AgCl) is applied to the bottom electrode (figure 6.3C). It is most likely that the feedback current is relatively small compared to diffusional flux of 1,1'-ferrocene dimethanol from the bulk phase to the electrode surface.

When the generator-collector currents are recorded due to the feedback effect, an additional current is observed with a sigmoidal shape (limiting current ca. 2 μA) and without any contribution from capacitive charging currents at the collector electrode (with fixed potential). Figure 6.3B and C, cyclic voltammograms in dual mode with top electrode at fixed potential and bottom electrode at fixed potential respectively, demonstrate that this is possible for both the top electrode scanning and the bottom electrode scanning. The voltammetric signal from the scanning electrode is transient in nature and more complicated due to the superposition of capacitive currents and diffusional currents for processes in the open solution and in the generator-collector gap. When changing the role of the two electrodes, a complementary data set is obtained (figure 6.3B and C). Figure 6.4A and B shows schematic drawings for the case of the top elec-

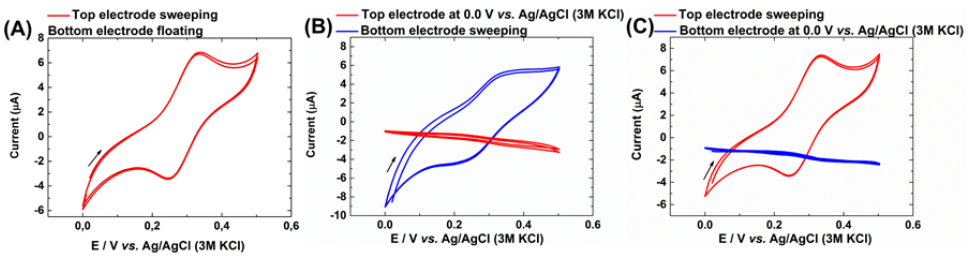

Figure 6.3: Cyclic voltammograms (two potential cycles; scan rate 10 mVs^{-1}) for oxidation of 0.25 mM 1,1'-ferrocene dimethanol in aqueous 0.1 M KNO_3. (A) Top electrode scanning and bottom electrode floating (disconnected). (B) Bottom electrode scanning and top electrode at 0.0 V *vs.* Ag/AgCl. (C) Top electrode scanning and bottom electrode at 0.0 V *vs.* Ag/AgCl.

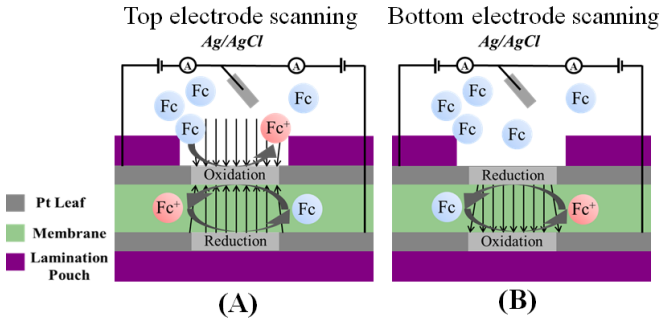

Figure 6.4: Schematic drawing of (A) the top electrode scanning and (B) the bottom electrode scanning.

trode scanning and the bottom electrode scanning. One would anticipate for the case of the bottom electrode scanning that only the feedback current is observed without diffusional peaks. Experimentally, the shape for the voltammetric response at the scanning bottom electrode (figure 6.3B) is indeed more sigmoidal, but there is also a substantial background current, which may be associated with lateral transport in the sandwich electrode configuration. Data for the collector currents obtained for the top electrode scanning appears to be most well-defined with the collector current response reflecting the 1,1'-ferrocene dimethanol solution concentration. Next, the effect of scan rate is investigated.

Figure 6.5 shows data for the top electrodes scanning and the bottom electrode at fixed potential. Perhaps surprisingly, with an increase in potential scan rate peak-shaped current responses are observed also for the collector electrode. A transition appears to occur at approximately 10 mVs^{-1} where the sigmoidal steady state responses changes into a more peak-shaped transient current response.

The change in diffusion characteristics can be attributed to diffusional delay in the track-etch nano-pore membrane. For the configuration with the top electrode scanning and the bottom electrode fixed at 0.0 V *vs.* Ag/AgCl and at sufficiently slow scan rates a fully developed diffusion layer is established across the membrane. However, for a faster

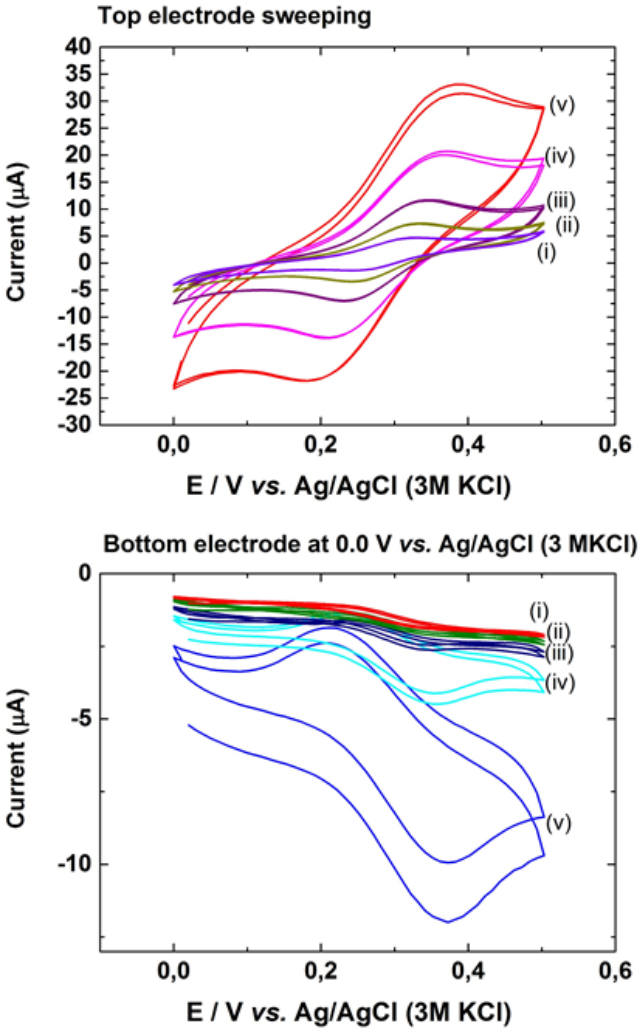

Figure 6.5: Cyclic voltammograms as a function of scan rates for the oxidation of 0.25 mM 1,1'-ferrocene dimethanol in aqueous 0.1 M KNO_3 solution. The top electrode as generator was sweeping the potential and the bottom electrode as collector (potential fixed at 0.0 V *vs.* Ag/AgCl). (i) 5 mVs^{-1}, (ii) 10 mVs^{-1}, (iii) 20 mVs^{-1}, (iv) 50 mVs^{-1}, (v) 100 mVs^{-1}.

scan rate the steady state current response changes toward peak shaped curves. This transition happens owing to the (A) mass transport delay and (B) the device functioning as capacitor with symmetric charge transfer in the short time domain.

From the transition scan rate estimated as υ_{trans} = 10 mVs^{-1} the realistic gap size, δ, is estimated to be 40 μm, using equation 6.2 [22].

$$\delta = \sqrt{\frac{DRT}{F\upsilon_{\text{trans}}}} \tag{6.2}$$

In this expression the diffusion coefficient of 1,1'-ferrocene dimethanol is D = 0.67 × $10^{-9} m^2/s$ [7], the estimated transition scan rate is 10 mVs^{-1} (for scan rates faster than 10 mVs^{-1} peak features appear for the collector electrode), F is the Faraday constant, R is the gas constant and T denotes the absolute temperature. The value δ = 40 μm is in excellent agreement with the nominal thickness of the track-etch membrane.

6.3.2. GENERATOR– COLLECTOR VOLTAMMETRY II.: SEPARATION OF OXYGEN REDUCTION AND PROTON REDUCTION RESPONSES

Generator-collector electrode systems can be employed to distinguish between redox processes that allow feedback via redox cycling (*e.g.* hydrogen evolution, see equation 6.3) and redox processes that are irreversible (*e.g.* oxygen reduction to water, see equation 6.4).

$$H^+ + e^- \rightleftarrows 1/2H_2 \tag{6.3}$$

$$1/2O_2 + 2H^+ + 2e^- \longrightarrow H_2O \tag{6.4}$$

Here, an indirect but quantitative oxygen determination is investigated based on the proton–hydrogen redox cycle by using the Pt–Pt generator–collector electrode in a solution containing 2 mM HNO_3 and 0.1 M KNO_3. For these measurements the top electrode (solution facing) was kept at a fixed potential of 0.2 V *vs.* Ag/AgCl and the bottom electrode (inward facing) was scanning (at a 10 mVs^{-1} scan rate). Figure 6.6A shows data for a solution exposed to ambient air (approximately 20% oxygen content). In this case, the bottom electrode can be employed to reduce protons to molecular hydrogen (equation 6.3). The reduced species then diffuses through the track-etch membrane and are oxidised back to protons at the top electrode(figures 6.6A and 6.7A). A schematic drawing is shown in figure 6.7B to explain proton diffusion towards the top electrode which is accompanied by an anodic current response at the bottom collector electrode. In this configuration there could be some loss of hydrogen into the solution phase. If the configuration is changed (figure 6.7A), hydrogen would be oxidised at the top electrode, which would lead to less loss of hydrogen into the solution and therefore a better defined current response.

Finally, in the presence of oxygen (figure 6.7C) both proton reduction (equation 6.3) and oxygen reduction (equation 6.4) occur simultaneously at the bottom electrode. Oxygen reduction consumes protons and this lowers the production of hydrogen and therefore the associated top collector oxidation current. In order to clarify the current responses at the generator and collector electrodes, measurements were performed in different solutions containing varying oxygen concentrations. Solutions were prepared by purging N_2, or pure O_2 gas in 20 mL portion of the electrolyte solution for 20 min. Cyclic

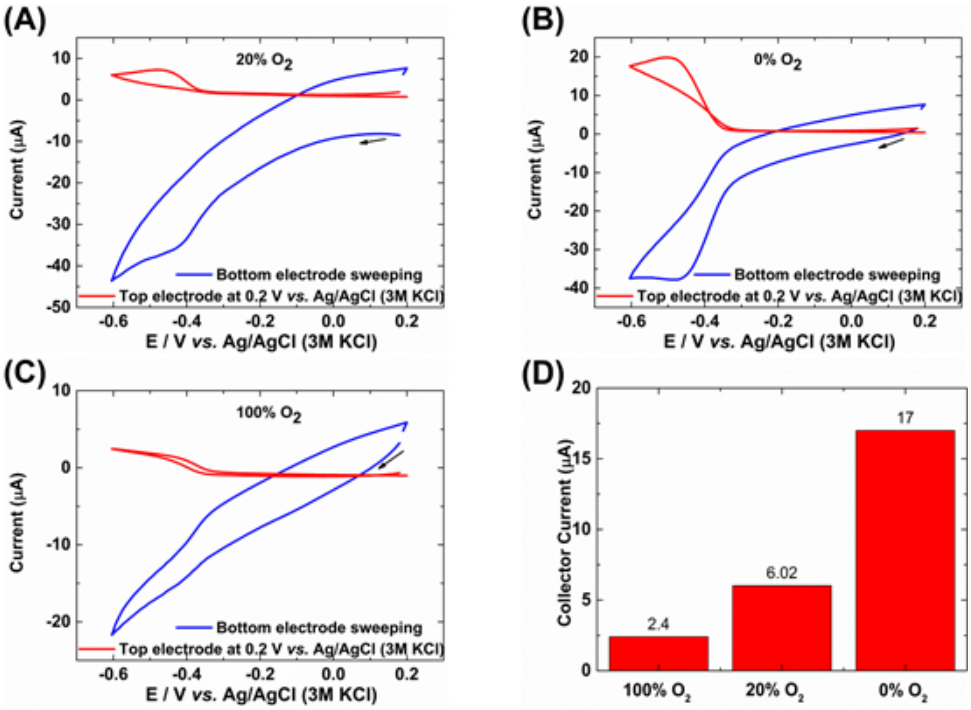

Figure 6.6: Cyclic voltammograms for top and bottom electrode for an electrolyte containing 2 mM HNO_3 in 0.1 M KNO_3 (at a 10 mVs^{-1} scan rate) (A) in ambient air, (B) de-aerated with nitrogen, and (C) saturated with pure oxygen. (D) Bar graph showing the collector current response for hydrogen oxidation diminishing in the presence of oxygen in the electrolyte solution.

voltammetry measurements were then performed immediately under the ambient conditions. Figures 6.6B and C present the results from these measurements. As can be seen purging with nitrogen increases the local hydrogen and proton concentration leading to an increased sensor signal (figure 6.6B). In contrast enriching the solution with pure oxygen lowered the local concentration of protons and hydrogen within the sandwich sensor, which leads to a lower collector current response (figure 6.6C). The same trend is visible in the generator current response, but this is partially obscured by other current contributions. The plot in figure 6.6D clearly demonstrates the correlation of collector current response with oxygen concentration in solution. The choice of 2 mM proton concentration clearly is crucial in optimising the sensor signal for oxygen but the methodology could be improved by employing gel media to fix the proton concentration within the sandwich sensor relative to the outside proton concentration. The detection principle could be useful also for other types of analytes such as sulphide. Finally, redox systems which require removal of oxygen from the solution phase could be detected at the top electrode whilst in situ removing oxygen at the bottom electrode.

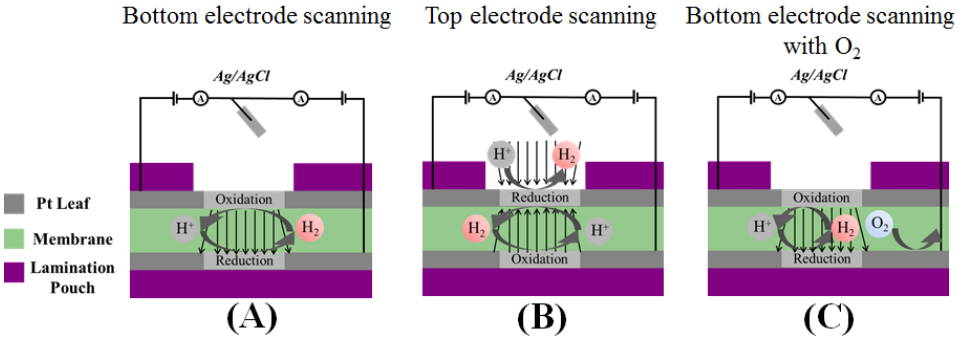

Figure 6.7: Schematic drawing for (A) proton-hydrogen redox cycling with the bottom electrode scanning, (B) proton-hydrogen redox cycling with the top electrode scanning, and (C) the effect of oxygen diffusion from the solution and reduction changing local proton and hydrogen concentration within the sandwich sensor.

6.4. CONCLUSION

It has been shown that platinum leaf materials can be assembled into a sandwich structure with a porous track etch membrane as a spacer. The resulting sandwich structure can be operated as a novel, simple and cheap generator-collector electrode with reference and counter electrode separately immersed into electrolyte solution. At sufficiently slow scan rates a steady state current without capacitive current contribution is registered at the collector electrode. The limiting current is proportional to the analyte solution concentration. Indirect oxygen sensing is possible based on the proton-hydrogen redox system and based on the fact that oxygen reduction is accompanied by removal of protons localised at the electrode surface. In future the design of the platinum–platinum sandwich sensor can be further improved (by changing the lamination pouch to more professional packaging, exploring solid substrates, optimising the membrane thickness and porosity, and by adding a top layer to protect the open platinum leaf) and adapted for a wider range of electroanalytical application.

REFERENCES

[1] H. R. Zafarani, L. Rassaei, E. J. Sudhölter, B. D. Aaronson, and F. Marken, *Generator–collector electrochemical sensor configurations based on track-etch membrane separated platinum leaves,* Sensors and Actuators B: Chemical **255**, 2904 (2018).

[2] E. O. Barnes, G. E. Lewis, S. E. Dale, F. Marken, and R. G. Compton, *Generator-collector double electrode systems: A review,* Analyst **137**, 1068 (2012).

[3] A. Frumkin, L. Nekrasov, B. Levich, and J. Ivanov, *Die anwendung der rotierenden scheibenelektrode mit einem ringe zur untersuchung von zwischenprodukten elektrochemischer reaktionen,* Journal of Electroanalytical Chemistry (1959) **1**, 84 (1959).

[4] M. Čerňanská, P. Tomčík, Z. Jánošíková, M. Rievaj, and D. Bustin, *Indirect voltammetric detection of fluoride ions in toothpaste on a comb-shaped interdigitated microelectrode array,* Talanta **83**, 1472 (2011).

[5] D. Bustin, Š. Mesároš, P. Tomčík, M. Rievaj, and V. Tvarožek, *Application of redox cycling enhanced current at an interdigitated array electrode for iron-trace determination in ultrapure spectral carbon,* Analytica chimica acta **305**, 121 (1995).

[6] M. A. Zevenbergen, B. L. Wolfrum, E. D. Goluch, P. S. Singh, and S. G. Lemay, *Fast electron-transfer kinetics probed in nanofluidic channels,* Journal of the American Chemical Society **131**, 11471 (2009).

[7] H. R. Zafarani, K. Mathwig, E. J. Sudhölter, and L. Rassaei, *Electrochemical redox cycling in a new nanogap sensor: Design and simulation,* Journal of Electroanalytical Chemistry **760**, 42 (2016).

[8] C. Ma, N. M. Contento, L. R. Gibson, and P. W. Bohn, *Redox cycling in nanoscale-recessed ring-disk electrode arrays for enhanced electrochemical sensitivity,* Acs Nano **7**, 5483 (2013).

[9] B. Wolfrum, M. Zevenbergen, and S. Lemay, *Nanofluidic redox cycling amplification for the selective detection of catechol,* Analytical chemistry **80**, 972 (2008).

[10] H. R. Zafarani, K. Mathwig, S. G. Lemay, E. J. Sudholter, and L. Rassaei, *Modulating selectivity in nanogap sensors,* ACS Sensors **1**, 1439 (2016).

[11] M. A. Zevenbergen, P. S. Singh, E. D. Goluch, B. L. Wolfrum, and S. G. Lemay, *Stochastic sensing of single molecules in a nanofluidic electrochemical device,* Nano letters **11**, 2881 (2011).

[12] S. G. Lemay, S. Kang, K. Mathwig, and P. S. Singh, *Single-molecule electrochemistry: present status and outlook,* Accounts of chemical research **46**, 369 (2012).

[13] L. Rassaei, P. S. Singh, and S. G. Lemay, *Lithography-based nanoelectrochemistry,* (2011).

[14] H. R. Zafarani, K. Mathwig, E. J. Sudholter, and L. Rassaei, *Electrochemical amplification in side-by-side attoliter nanogap transducers,* ACS Sensors **2**, 724 (2017).

[15] B. Wolfrum, E. Katelhon, A. Yakushenko, K. J. Krause, N. Adly, M. Huske, and P. Rinklin, *Nanoscale electrochemical sensor arrays: Redox cycling amplification in dual-electrode systems,* Accounts of chemical research **49**, 2031 (2016).

[16] Y. Wang, X. Lin, and B. Su, *Redox cycling with ito electrodes separated by an ultrathin silica nanochannel membrane,* Electrochemistry Communications **72**, 1 (2016).

[17] S. Park, J. H. Park, S. Hwang, and J. Kwak, *Bench-top fabrication and electrochemical applications of a micro-gap electrode using a microbead spacer,* Electrochemistry Communications **68**, 76 (2016).

[18] N. Adly, B. Bachmann, K. Krause, A. Offenhäusser, B. Wolfrum, and A. Yakushenko, *Three-dimensional inkjet-printed redox cycling sensor,* RSC Advances **7**, 5473 (2017).

[19] R. W. French, S. N. Gordeev, P. R. Raithby, and F. Marken, *Paired gold junction electrodes with submicrometer gap,* Journal of Electroanalytical Chemistry **632**, 206 (2009).

[20] M. A. Hasnat, A. J. Gross, S. E. Dale, E. O. Barnes, R. G. Compton, and F. Marken, *A dual-plate ito–ito generator–collector microtrench sensor: surface activation, spatial separation and suppression of irreversible oxygen and ascorbate interference,* Analyst **139**, 569 (2014).

[21] A. J. Gross and F. Marken, *Boron-doped diamond dual-plate microtrench electrode for generator–collector chloride/chlorine sensing,* Electrochemistry Communications **46**, 120 (2014).

[22] R. W. French, A. M. Collins, and F. Marken, *Growth and application of paired gold electrode junctions: evidence for nitrosonium phosphate during nitric oxide oxidation,* Electroanalysis **20**, 2403 (2008).

[23] S. E. Dale, C. E. Hotchen, and F. Marken, *Generator–collector electroanalysis at tin-doped indium oxide–epoxy–tin-doped indium oxide junction electrodes,* Electrochimica Acta **101**, 196 (2013).

7

SUMMARY AND OUTLOOK

7.1. SUMMARY

ELECTROCHEMICAL sensing is considered as one of the most powerful analytical detection techniques. Electrochemical methods have fast response time, high sensitivity and selectivity, and can be performed at low cost. Their inherent ease of miniaturization have made them so popular in recent years. Hence, electrochemical sensors have diverse applications including pathological [1, 2], clinical [3–6] and environmental [7, 8] analyses.

Miniaturization of analytical devices plays an important role in the sensor development studies. Miniaturized electrochemical sensors open up opportunities toward faster, more sensitive, more user friendly (ease to use) and portable systems compared to the traditional cumbersome bulky electrochemical cells. Thanks to the recent advances in nano/micro fabrication techniques, scaling down the electrode size to micro and even nano dimensions and developing "lab on a chip" technology is achievable and is considered as a hot topic in electrochemistry [9, 10].

Traditional electrochemical cells are composed of three electrodes: a working electrode, a reference electrode and a counter electrode. However, in this thesis the main focus is on the dual- electrode systems, where two closely spaced working electrodes are placed next to each other. Hence the events at each electrode can be affected by the other one. These two electrodes can be biased independently and the current of each can be detected separately. Biasing one of the electrodes in an oxidizing potential (according to a desired redox active analyte) and the other in a reducing potential, results in a repeated successive oxidation and reduction of analyte species on the two electrode surfaces. Accordingly, the current at each electrode is amplified which leads to a higher sensitivity. Reducing the gap size between the electrodes can further enhance the sensitivity and amplification factor (the ratio between the limiting current in dual electrode mode and the current in a single electrode mode) of the device.

There are different approaches for fabricating such devices. Interdigitated electrodes (comb-shaped electrodes), ring-disc or nanopore electrodes are most common dual-electrode systems. Lemay has proposed a thin layer cell structure consisting of two electrodes, which are placed in a few tenth nanometer distance on top of each other with an electrolyte solution in between [11]. They employed multiple steps of e-beam/photo lithography patterning techniques followed by multiple metal evaporation techniques, oxide deposition and dry etching processes to fabricate such a sophisticated sandwich structure device. The above mentioned devices are employed in chapters 2 and 3.

The capability and the unique feature of dual electrode devices are not only limited to the current amplification. It is shown in chapter 2 that these devices provide a powerful tool to enhance the selectivity in electrochemical measurements as well. Interference or crosstalk of coexisting compounds in the electrolyte leads to an overlap of electrochemical responses and is one of the major hurdles in electrochemical measurements. Separate detection of a few redox active molecules by modulation the potential of the electrodes in a nanogap sensor is described in this chapter. Our approach relies on modulating the electrode potentials to define a specific potential windows between the two working electrodes. Consequently, the specific detection of each redox species is achieved. Finite element modeling is employed to simulate the electrochemical processes in the nanogap sensor, and the corresponding results are in good agreement with

those of experiments.

In chapter 3, another capability of the nanogap sensors is described in molecular-level studies. Considering a very limited active volume in a nanogap (the volume which is trapped between the electrodes), only a limited number of analytes are present in the nanogap at each single moment. These molecules can diffuse in and out between the nanogap and the attached reservoir to the nanogap. Hence, the number of molecules in the nanogap fluctuates and accordingly this is reflected in the measured current. Analyzing the fluctuation in current-time traces (stochastic analysis) can reveal information such as: diffusion coefficients of the molecule as well as the generated Faradic current per molecule. In this chapter the molecular properties of 2,3,4-triferrocenylthiop-hene and 2,5-diferrocenylthiophene compounds are studied within a nanogap sensor. It is found that diffusive transport is reduced for higher oxidation states and that analytes generate very high currents per molecule of 15 fA.

In chapters 4 and 5, a new design for nanogap sensors, working under redox cycling is introduced. The new design consists of two side-by-side electrodes which are placed closely next to each other. In chapter 4, the effect of geometrical aspects of the device on its performance is fully studied, using finite element simulation methods. Based on the simulated results, in chapter 5, the proposed device is fabricated. As is discussed there (chapter 5), the fabrication procedure for this device is straight forward, capable of using different electrode materials and provides setting a wide range of gap sizes. The open geometry of the device - the nanochannel between the electrodes is directly in contact with the bulk solution - enables a very fast response time compared to the covered nanogap devices - where the nanochannel between the electrodes is surrounded completely by an insulating layer and the solution is introduced via access holes between the electrodes. The open geometry allows direct access of optical detection methods as well, thus enabling observation of combined optical-electrochemical molecular properties.

In the final chapter (chapter 6) of the thesis, a new simple and cost-effective macrogap sensor is introduced. As is addressed in chapters 4 and 5, a new nanogap design with more straight forward fabrication procedures is introduced in the thesis. However, still there is a need to access the cleanrooms and nanofabrication procedures. Dual-electrode systems are not only limited to the nanogap devices; macrogap electrodes also provide nice and novel applications in electrochemical detection field. In this chapter a very simple macrogap sensor, employing platinum leaves sandwiched with a porous track etch membrane spacer, is introduced. The fabricated device shows good performance in monitoring both 1,1'-ferrocene dimethanol oxidation and proton reduction redox processes.

7.2. OUTLOOK

In this thesis, nanogap devices, as powerful electrochemical sensors, are employed. These devices can drastically enhance the sensitivity and selectivity of the detection method. Thanks to the unique structure of these devices fundamental studies down to the molecular level are achievable.

The author would like to mention a few future relevant outlooks of this research; In nanogap devices the electrodes are mainly made of platinum or gold (in few studies tin doped indium oxide, ITO, is used in macrogap dual-electrode systems [12, 13]). However

in this thesis with the new design for nanogap electrodes (Chapters 4 and 5), fabricating nanogaps with other materials such as graphene is possible, which can open new related studies. As addressed before in this thesis, due to the fabrication requirements for metallic electrodes, mainly because of the lift-off process, there is a need for a thin adhesion layer underneath the metal electrodes such as a thin layer of Ti or Cr underneath the Au or Pt electrodes. Once a sensor is in contact with an electrolyte, galvanic corrosion of these dual metal couples can deteriorate the sensor functionality during long term electrochemical measurements. Carbon based electrodes can be used as stable, biocompatible electrodes in electrochemical measurements [14–16]. Also the proposed open nanogap geometry provides the opportunity to combine optical detection methods with electrochemical measurements. In the new fabrication method, e-beam lithography allows a further considerable reduction of the interelectrode distance, increasing its sensitivity and further reducing the active volume. Tuning the interelectrode gap size can define different diffusion time between the electrodes. Combining this property to the kinetics of the reactions ongoing in the electrolyte solution can enhance the selectivity and separate detection of different analytes in dual-electrode systems, as partially is reported in [17] for catecholamines or detection the short-lived reaction intermediates.

SAMENVATTING

ELEKTROCHEMISCHE detectie wordt beschouwd als een van de krachtigste analytische-technieken. Deze methoden hebben een snelle reactietijd, hoge gevoeligheid en selectiviteit, en kunnen worden uitgevoerd tegen lage kosten. Het inherente gemak waarmee deze detectiemethoden kunnen worden geminiaturiseerd maakt dat ze zo populair zijn geworden de afgelopen jaren. Vandaar dat elektrochemische sensoren verschillende toepassingen hebben, zoals in pathologische [1, 2] en klinische analyses [3–6], als ook in milieuanalyses [7, 8].

Miniaturisatie van de analytische apparaten speelt een belangrijke rol in de studies rond sensorontwikkeling. Geminiaturiseerde elektrochemische sensoren creëren nieuwe mogelijkheden voor snellere, gevoeliger, gebruikersvriendelijkere en draagbare systemen, dit in vergelijking met de traditionele en vaak omslachtige en grote elektrochemische cellen. Dankzij recente ontwikkelingen in de nano- tot micrometer grootte productietechnieken, waarbij de grootte van de electroden verkleind worden tot dit domein, en het ontwikkelen van "lab on a chip" technologie is dit allemaal haalbaar geworden. Het wordt dan ook gezien als veelbelovend en van grote interesse voor het elektrochemische onderzoeksveld [9, 10].

Traditionele elektrochemische cellen zijn samengesteld uit drie elektroden: een werkelektrode, een referentieelektrode en een tegenelektrode. Echter, in dit proefschrift ligt de nadruk op de dubbele electrode systemen, waarin twee werkelektroden dicht bij elkaar in de buurt zijn geplaatst. Daardoor kunnen de gebeurtenissen bij de ene elektrode worden beïnvloed door de andere. De potentiaal van deze twee elektroden kunnen onafhankelijk van elkaar worden ingesteld en de electrische stroom kan afzonderlijk worden gedetecteerd. Het instellen van één van de elektroden op een oxiderende potentiaal (behorende bij een gewenste redox-actieve analiet) en de andere electrode op de bijbehorende reducerende potentiaal, resulteert in herhaalde opeenvolgende oxidatie en reductie van het analiet aan de beide elektroden. Deze cyclische oxidatie en reductie resulteert in een versterking van de gemeten electrische stroom. Hiermee wordt dus een hogere gevoeligheid verkregen. Het verder verkleinen van de afstand tussen beide elektroden, leidt tot een verdere versterking van de gevoeligheid. Ook de versterkingsfactor (dit is de ratio tussen de limiterende stroom in dubbele-elektrode configuratie en de stroom in een enkele-elektrode configuratie) zal hierdoor toenemen.

Er zijn verschillende benaderingen voor het fabriceren van zulke apparaten. Vingervormige elektroden (kamvormige elektroden), schijfvormige elektroden of nanopore elektroden behoren tot de meest voorkomende dubbele-elektrode systemen. Lemay heeft een dunne-laag celstructuur voorgesteld, bestaande uit twee elektroden die op een afstand van enkele tienden van een nanometer boven elkaar worden geplaatst met een elektrolytoplossing daar tussen [11]; Zij gebruikten meerdere productiestappen van elektronenbundel/fotolithografische technieken gevolgd door meerdere metaal-dampdepositie technieken, oxide depositie en plasma ets processen, om op deze wijze een

dergelijke verfijnde “sandwich”-structuur te maken. Op deze wijze gemaakte apparaten worden in het onderzoek gebruikt, zoals beschreven in hoofdstukken 2 en 3.

De geschiktheid en de unieke eigenschappen van dubbele-elektroden apparaten beperken zich niet alleen tot de stroomversterking. In hoofdstuk 2 wordt beschreven dat deze apparaten ook bijzonder krachtig zijn in het verbeteren van de selectiviteit in elektrochemische metingen. Interferentie of overspraak van naast elkaar aanwezige analieten in de elektrolytoplossing, leidt tot overlappende elektrochemische reacties en vormt zo een van de grootste hindernissen bij elektrochemische metingen. Afzonderlijke detectie van een aantal redox-actieve analieten, door aanpassing van de potentiaal van de elektroden in de “nanogap” sensoren wordt beschreven in dit hoofdstuk. Onze aanpak berust op het zodanig aanpassen van de beide elektrodepotentialen, zodat de reikwijdte tussen beide werkelectroden is bepaald. Op deze wijze wordt specifieke detectie van elke redox-acieve analiet mogelijk. Eindige elementen modellering is toegepast om de elektrochemische processen in de “nanogap” sensor te simuleren en de verkregen resultaten blijken in goede overeenstemming te zijn met de experimenten.

In hoofdstuk 3 wordt een andere geschiktheid van “nanogap” sensoren beschreven in een studie op moleculair niveau. Omdat het actieve volume in een “nanogap” (het aanwezige volume tussen de elektroden) heel klein is, zijn slechts een beperkt aantal analietmoleculen aanwezig. Deze moleculen kunnen zowel in als uit diffunderen tussen de “nanogap” en het aan deze “nanogap” grenzende reservoir. Hierdoor fluctueert het aantal moleculen in de “nanogap” in de tijd en dit wordt weerspiegeld in de gemeten fluctuerende stroom. Analyse van deze fluctuatie (stochastische analyse) kan informatie verschaffen zoals de diffusiecoëfficiënten van het molecuul, en ook de gegenereerde Faraday-stroom per molecuul. In dit hoofdstuk worden deze moleculaire eigenschappen van 2,3,4-tri-ferrocenyl thiofeen en 2,5-di-ferrocenyl thiofeen bestudeerd in een “nanogap” sensor. Hieruit blijkt dat transport via diffusie trager is voor de hogere oxidatietoestand van het analiet en dat deze analieten zeer hoge stromen van 15 fA per molecuul opleveren.

In de hoofdstukken 4 en 5 wordt een nieuw ontwerp voor “nanogap” sensoren geïntroduceerd dat werkt volgens redox cycling. Het nieuwe ontwerp bestaat uit twee elektrodes die dicht bij elkaar en zij aan zij worden geplaatst. In hoofdstuk 4 wordt het effect van de geometrische aspecten van het apparaat op zijn prestaties volledig onderzocht en met behulp van eindige elementen methoden gesimuleerd. Gebaseerd op deze resultaten wordt, in hoofdstuk 5, het voorgestelde apparaat gefabriceerd. Zoals daar (hoofdstuk 5) wordt besproken is de fabricageprocedure voor dit apparaat eenvoudig, en biedt mogelijkheden om verschillende elektrodematerialen te gebruiken en biedt bovendien de mogelijkheid om te variëren in “nanogap” dimensies. De open geometrie van het apparaat – het nanokanaal tussen de elektroden staat in direct contact met de reservoiroplossing – maakt een zeer snelle reactietijd mogelijk ten opzichte van de bedekte “nanogap” apparaten – waar het nanokanaal tussen de elektrodes compleet omgeven wordt door een isolerende laag en de reservoir oplossing alleen via de openingen tussen beide elektrodes toegang heeft. Deze open geometrie maakt het ook mogelijk om met optische methoden toegang te hebben tot dit kleine volume. Zo kunnen gelijktijdig optische- en electrochemische eigenschappen van de moleculen aanwezig in het “nanogap” volume worden onderzocht.

In het laatste hoofdstuk (hoofdstuk 6) van dit proefschrift wordt een nieuwe, eenvoudig te maken, en goedkope “macrogap” sensor geïntroduceerd. In de hoofdstukken 4 en 5 wordt een nieuw “nanogap” ontwerp geïntroduceerd. Echter voor het fabriceren van deze apparaten zijn cleanroom en nanofabricatiemethoden nodig. Dubbele-elektrode systemen zijn niet alleen mogelijk in “nanogap” apparaten; ook “macrogap” elektroden bieden mooie en nieuwe toepassingen op het terrein van elektrochemische-detectie. In dit hoofdstuk wordt een erg eenvoudige “macrogap” sensor geintroduceerd, waarbij gebruik gemaakt wordt van platina blaadjes, die ingeklemd worden tussen “track-etch” membranen. Het aldus gefabriceerde apparaat laat goede prestaties zien in het registreren van zowel de 1,1’-ferrocene dimethanol oxidatie als bij proton reductie redox processen.

VOORUITZICHT

In dit proefschrift is onderzoek beschreven dat is uitgevoerd aan “nanogap” apparaten. Deze hebben zich getoond als krachtige elektrochemische sensoren, welke een drastische verbetering laten zien wat betreft gevoeligheid en selectiviteit. Dankzij de unieke structuur van deze apparaten zijn fundamentele studies tot op het moleculaire niveau haalbaar.

De auteur wil graag enkele toekomstgerelateerde vooruitzichten op dit onderzoeksgebied noemen. In “nanogap” apparaten zijn de elektroden meestal gemaakt van platina of goud (in enkele studies van “macrogap” dubbele-electrodensystemen wordt ook tin gedoteerd indium oxide (ITO) gebruikt [12, 13]). Met het nieuwe ontwerp voor “nanogap” electroden in dit proefschrift (hoofdstukken 4 en 5), is ook het gebruik van andere electrodenmaterialen mogelijk, zoals bijvoorbeeld grafeen. Dit kan leiden tot nieuwe gerelateerde onderzoeken. Zoals eerder beschreven in dit proefschrift, vereist de fabricatie van metaalelectroden, de aanwezigheid van een dunne adhesielaag (vaak titanium of chroom) direct onder de platina- of goudelectroden. Dit vanwege het toegepaste “lift-off” proces. Zodra een dergelijke sensor contact maakt met de elektrolytoplossing kan galvanische corrosie optreden en de functionaliteit van deze gecombineerde metaalkoppel kapotmaken. Op koolstof-gebaseerde elektroden (zoals grafeen) hebben daar geen last van en kunnen gebruikt worden als stabiele, bio-compatibele elektroden in elektrochemische metingen [14–16]. De voorgestelde open-nanogap-geometrie biedt hier ook de kans om optische detectiemethodes te combineren met elektrochemische metingen. In de nieuwe fabricagemethode laat elektronenbundel lithografie een verdere aanzienlijke reductie toe in de afstand tussen de elektroden, wat leidt tot verhoging van de gevoeligheid en een verdere reductie van het actieve volume. Het fijn afstemmen van de preciese afmetingen van de ruimte tussen de elektroden bepaalt de diffusietijd tussen deze elektroden. In combinatie met de kinetiek van reacties, die in de elektrolytoplossing verlopen, kan zo de selectiviteit worden verbeterd en verschillende analieten gescheiden worden gedetecteerd. Dit is voor een deel gerapporteerd [17] voor catecholamines en voor de detectie van bepaalde kortlevende reactieintermediairen.

REFERENCES

[1] B. V. Chikkaveeraiah, A. A. Bhirde, N. Y. Morgan, H. S. Eden, and X. Chen, *Electrochemical immunosensors for detection of cancer protein biomarkers,* ACS nano **6**, 6546 (2012).

[2] H. Li, J. He, S. Li, and A. P. Turner, *Electrochemical immunosensor with n-doped graphene-modified electrode for label-free detection of the breast cancer biomarker ca 15-3,* Biosensors and Bioelectronics **43**, 25 (2013).

[3] A. Vasudev, A. Kaushik, Y. Tomizawa, N. Norena, and S. Bhansali, *An ltcc-based microfluidic system for label-free, electrochemical detection of cortisol,* Sensors and Actuators B: Chemical **182**, 139 (2013).

[4] Q. Yan, B. Peng, G. Su, B. E. Cohan, T. C. Major, and M. E. Meyerhoff, *Measurement of tear glucose levels with amperometric glucose biosensor/capillary tube configuration,* Analytical chemistry **83**, 8341 (2011).

[5] M. Gamella, S. Campuzano, J. Manso, G. G. De Rivera, F. López-Colino, A. Reviejo, and J. Pingarrón, *A novel non-invasive electrochemical biosensing device for in situ determination of the alcohol content in blood by monitoring ethanol in sweat,* Analytica chimica acta **806**, 1 (2014).

[6] A. J. Bandodkar and J. Wang, *Non-invasive wearable electrochemical sensors: a review,* Trends in biotechnology **32**, 363 (2014).

[7] K. A. Howell, E. P. Achterberg, C. B. Braungardt, A. D. Tappin, D. R. Turner, and P. J. Worsfold, *The determination of trace metals in estuarine and coastal waters using a voltammetric in situ profiling system,* Analyst **128**, 734 (2003).

[8] M.-L. Tercier and J. Buffle, *In situ voltammetric measurements in natural waters: future prospects and challenges,* Electroanalysis **5**, 187 (1993).

[9] J. Wang, *Portable electrochemical systems,* TrAC Trends in Analytical Chemistry **21**, 226 (2002).

[10] L. Rassaei, P. S. Singh, and S. G. Lemay, *Lithography-based nanoelectrochemistry,* (2011).

[11] M. A. Zevenbergen, B. L. Wolfrum, E. D. Goluch, P. S. Singh, and S. G. Lemay, *Fast electron-transfer kinetics probed in nanofluidic channels,* Journal of the American Chemical Society **131**, 11471 (2009).

[12] S. E. Dale, C. E. Hotchen, and F. Marken, *Generator–collector electroanalysis at tin-doped indium oxide–epoxy–tin-doped indium oxide junction electrodes,* Electrochimica Acta **101**, 196 (2013).

[13] M. A. Hasnat, A. J. Gross, S. E. Dale, E. O. Barnes, R. G. Compton, and F. Marken, *A dual-plate ito–ito generator–collector microtrench sensor: surface activation, spatial separation and suppression of irreversible oxygen and ascorbate interference,* Analyst **139**, 569 (2014).

[14] J. Heo, D. Shim, G. T. Teixidor, S. Oh, M. Madou, and H. Shin, *Carbon interdigitated array nanoelectrodes for electrochemical applications,* Journal of the Electrochemical Society **158**, J76 (2011).

[15] M. Pumera, A. Ambrosi, A. Bonanni, E. L. K. Chng, and H. L. Poh, *Graphene for electrochemical sensing and biosensing,* TrAC Trends in Analytical Chemistry **29**, 954 (2010).

[16] T. Kuila, S. Bose, P. Khanra, A. K. Mishra, N. H. Kim, and J. H. Lee, *Recent advances in graphene-based biosensors,* Biosensors and Bioelectronics **26**, 4637 (2011).

[17] M. Hu and I. Fritsch, *Redox cycling behavior of individual and binary mixtures of catecholamines at gold microband electrode arrays,* Analytical chemistry **87**, 2029 (2015).

ACKNOWLEDGEMENTS

Now I am at the end of my Ph.D. journey. A journey for four years; full of adventures, challenges, amazing experiences and lots of frustrating moments. Going through this journey was not possible without help and support of great people around who helped me to growth as a researcher.

First of all I would like to thank Prof. dr. Ernst J.R. Sudhölter and Dr. Liza Rassaei for offering the opportunity to do my research as a Ph.D. candidate in their group. I always enjoyed our discussions and meetings. Your valuable hints and feedbacks helped me to growth a lot; not only scientifically but more importantly in personal skills development aspects.

My special and sincere thanks to Dr. Klaus Mathwig. Klaus, thanks for all your supports and helps, thanks for all your countless useful hints and discussions, thanks for being available and making time for me whenever I needed your help.

I like to thank Wolter, Klaas, Louis, Marcel, Duco for their hints during our group meeting. Klaas, thank for providing me a chance to take a role as a teaching assistance in "Thermodynamics of Life Science" course, it was a great experience. Duco, thanks for all your technical and useful guides in the laboratory and all your efforts that you made to make and run my measurement setup. Venkatesh, Daniela, Zhen, Aldo, Anping, Pierre, Nick, Sumit, Rajeev, Lukasz, Naveen, Liangyong , Stijn, Laura, Mohammad, Jesse, Nienke, Hanan, Arun, Sneha, thanks guys for being awesome colleagues, thanks for our nice chats during coffee breaks and lunch times and thanks for making unforgettable memories in OMI for me. Wish you all lots of success both in your careers and personal lives. Nienke, thanks a lot for being a great colleague and a kind neighbor next to my desk in the office within my last few months of Ph.D. . I enjoyed all our daily chats and thanks a lot for your kind help in translating the summary of the thesis, wish you lots of success in your research.

I also would like to thank all the support staff who have helped me through my Ph.D., thanks to Marian, Karin, Caroline and Els who always helped me with all administrative and paper works.

Thanks to Kavli Nanolab staff for all their valuable cleanroom fabrication advices and keep the machines running; Anja, Roel, Eugene, Marco, Marc, Charles, Hozanna. Thanks Leonardo for training me on e-beam lithography machine. Thanks Carel for all useful fabrications hints that you taught me.

My dear friends Afshin, Yoones, Amin, Saeid, Bijan thanks for your presence and all your supports.

Finally, my deepest sincere appreciation and thanks goes to my family who always support me even from far away. Dear Dad and Mom, without you and your endless love and support that you have given me, I might not be the person I am today; Thanks for everything. My lovely younger sister and brother, thanks for all your helps and supports. I proud of you and wish you all the best.

BIOGRAPHY

Hamid Reza Zafarani was born on 22nd March 1987 in Shiraz , Iran. He received his B.Sc. and M.Sc. in Materials Science and Engineering, Shiraz University, Shiraz, Iran. In April 2014, he started his Ph.D. at the Department of Chemical Engineering at Delft University of Technology, Delft, The Netherlands. During his Ph.D., he worked on developing and fabricating new nano-/micro gap electrochemical sensors working based on redox cycling amplification.

LIST OF PUBLICATIONS

9. **H.R. Zafarani**, L. Rassaei, E.J.R. Sudhölter, B.D.B. Aaronson and F. Marken, “Generator–collector electrochemical sensor configurations based on track-etch membrane separated platinum leaves”, Sensors and Actuators B: Chemical, 2018, 255, pp 2904-2909.

8. A. Feizabadi, M. Salehi Doolabi, S.K. Sadrnezhaad, **H.R. Zafarani**, D. Salehi Doolabi and M. AsadiZarch, “MCDM selection of pulse parameters for best tribological performance of Cr–Al2O3 nano-composite co-deposited from trivalent chromium bath”, Journal of Alloys and Compounds, 2017, 727, pp 286-296.

7. **H.R. Zafarani**, K. Mathwig, E.J.R. Sudhölter and L. Rassaei, “Electrochemical amplification in side-by-side attoliter nanogap transducers”, ACS Sensors, 2017, 2 (6), pp 724–728.

6. **H.R. Zafarani**, K. Mathwig, S.G. Lemay, E.J.R. Sudhölter and L. Rassaei, “Modulating selectivity in nanogap sensors”, ACS Sensors, 2016, 1 (12), pp 1439–1444.

5. H. Al-Kutubi, **H.R. Zafarani**, L. Rassaei and K. Mathwig, “Electrofluorochromic systems: Molecules and materials exhibiting redox-switchable fluorescence”, European Polymer Journal, 2016, 83, pp 478-498.

4. K. Mathwig, **H.R. Zafarani**, J.M. Speck, S. Sarkar, H. Lang, S.G. Lemay, L. Rassaei and O.G. Schmidt, ”Potential-dependent stochastic amperometry of multiferrocenylthiophenes in an electrochemical nanogap transducer”, The Journal of Physical Chemistry C, 2016, 120 (40), pp 23262–23267.

3. C. Tudisco, G. Zolubas, B. Seoane, **H.R. Zafarani**, M. Kazemzad, J. Gascon, P.-L. Hagedoorn and L. Rassaei, “Covalent immobilization of glucose oxidase on amino MOFs via post-synthetic modification”, RSC Advances, 2016, 6, pp 108051-108055.

2. **H.R. Zafarani**, K. Mathwig, E.J.R. Sudhölter and L. Rassaei, “Electrochemical redox cycling in a new nanogap sensor: Design and simulation”, Journal of Electroanalytical Chemistry, 2016, 760, pp 42-47.

1. H. Al-Kutubi, A. Dikhtiarenko, **H.R. Zafarani**, E.J.R. Sudhölter, J. Gascon and L. Rassaei, “Facile formation of ZIF-8 thin films on ZnO nanorods", CrystEngComm, 2015, 17, pp 5360-5364.

Prior to this thesis

6. **H.R. Zafarani**, M.E. Bahrololoom, C. Noubactep and J. Tashkhourian, “Green walnut shell as a new material for removal of Cr (VI) ions from aqueous solutions", Desalination and Water Treatment, 2015, 55 (2), pp 431-439.

5. R. Bazargan-Lari, **H.R. Zafarani**, M.E. Bahrololoom and A. Nemati, “Removal of Cu (II) ions from aqueous solutions by low-cost natural hydroxyapatite/chitosan composite: equilibrium, kinetic and thermodynamic studies", Journal of the Taiwan Institute of Chemical Engineers, 2014, 45(4), pp 1642-1648.

4. **H.R. Zafarani**, M.E. Bahrololoom, M. Javidi, M.H. Shariat and J. Tashkhourian, “Removal of chromate ion from aqueous solutions by sponge iron", Desalination and Water Treatment, 2014, 52 (37-39), pp 7154-7162.

3. **H.R. Zafarani**, M. Abdi and M.E. Bahrololoom, “Wear behavior of PTFE - Hydroxyapatite composite fabricated by hot-press sintering process", Acta Metallurgica Sinica (English Letters), 2014, 27(2), pp 347–351.

2. **H.R. Zafarani**, A. Hassani, E. Bagherpour, “Achieving a desirable combination of strength and workability in Al/SiC composites by AHP selection method", Journal of Alloys and Compounds, 2014, 589, pp 295-300.

1. **H.R. Zafarani**, N. Gactha-Bandjun, C. Tsamo, M.E. Bahrololoom, C. Noubactep and J. Tashkhourian, “Evaluating the suitability of the testing procedures for alternative adsorbing materials for wastewater treatment", Fresenius Environmental Bulletin,2014, 26, pp 1433-1437.